

# **Nano-Confined Room-Temperature Ionic Liquids for Electrochemical Applications**

Yadong He

Dissertation submitted to the faculty of the Virginia Polytechnic Institute and State University in partial fulfillment of the requirements for the degree of

Doctor of Philosophy  
In  
Mechanical Engineering

Rui Qiao, Chair

Chang Lu

Jiangtao Cheng

Louis A. Madsen

Zhiting Tian

February 14<sup>th</sup>, 2018  
Blacksburg, Virginia

Keywords: Room-temperature ionic liquids, nanopore, ion gel, molecular dynamics

Copyright 2018, Yadong He

# Nano-Confined Room-Temperature Ionic Liquids for Electrochemical Applications

Yadong He

## ABSTRACT

This dissertation focuses on the application of nano-confined room-temperature ionic liquids (RTILs) as electrolytes or components of electrolytes in electrochemical devices.

The mass deployment of supercapacitors is hindered by their low energy density. Using RTILs as electrolytes and porous carbons with subnanometer pores as electrodes can potentially resolve this issue but the dynamic charge storage in these materials is little understood. The dynamics of RTILs in nanopores under conditions similar to those during charging is studied first. Based on molecular simulations of EMIM<sup>+</sup> and TFSI<sup>-</sup> ions in slit micropores, it is shown that, in pores accommodating only one layer of ions, ions diffuse increasingly faster as the pore becomes charged. This trend is only reversed when the pore becomes highly charged. The charge storage in RTIL-filled nanopores during cyclic (dis)charging is studied next. It is shown that the cyclic (dis)charging of nanopores is governed by the interplay between the external field-driven ion transport and the sloshing dynamics of ions inside the pores. The ion occupancy along the pores depends strongly on the scan rates. Unlike that at low scan rates, charge storage at high scan rates is dominated by counterions and the contribution by co-ions is marginal or negative.

Electrochemical devices often demand solid electrolytes with both high ionic conductivities and excellent mechanical strength. The recent invention of PBDT ion gels featuring aligned polyanions immersed inside RTILs has shown great promise in meeting this demand, but the mechanism behind their superior mechanical strength is not yet

understood. Using molecular simulations, the high elastic moduli of model PBDT ion gels is reproduced. In particular, the elastic modulus in direction normal to polyanions' axis reaches hundreds of MPa. This strong modulus originates from the RTIL-mediated interactions between polyanions. Under transverse loading, the interference of the ionic space charges between polyanions (consequently the polyanion-polyanion interactions) become less favorable and thus resists transverse strain strongly. The computed shear modulus of the ion gels is small, consistent with experimental data and the fact that shear deformation of ion gels does not greatly modify the interference of space charges between their polyanions.

# Nano-Confined Room-Temperature Ionic Liquids for Electrochemical Applications

Yadong He

## GENERAL AUDIENCE ABSTRACT

Room-temperature ionic liquids (RTILs) and their derivatives are promising electrolytes for electrochemical devices including supercapacitors. Understanding the behavior of RTILs in these devices is critical for improving their performance.

The energy density of supercapacitors can be improved greatly by using RTILs as electrolytes and nanoporous carbon as electrodes, but the mechanism of the charge storage using these materials is not well understood. In this dissertation, the diffusion and charging dynamics of RTILs in nanopores are studied. The results show that ion packing typically plays the most important role in ion diffusion. The study also demonstrates that the cyclic charging and discharging of a pore can exhibit a number of interesting features (e.g., sloshing of ionic charge along the pores during cyclic scans), which help explain experimental observations such as the negligible contribution of co-ions to charge storage at high scan rates.

Solid electrolytes with both high ionic conductivities and excellent mechanical strength are needed in many electrochemical devices. The invention of ion gels featuring aligned polyanions immersed inside RTILs has shown promise in meeting this demand, but the mechanism behind their superior mechanical strength remains elusive. Using molecular simulations, it is discovered that the high elastic moduli of model PBDT ion gels originate from the RTIL-mediated interactions between the polyanions. This insight is useful for future design of ion gels to improve their transport and mechanical properties.

## **Dedication**

For my mother, Mrs. Guimei Wang, my father, Mr. Liuqing He, and my sister Ms. Dongxiao He.

# Acknowledgments

I would like to express my deep gratitude to my advisor Dr. Rui Qiao for his constant support and encouragement. He inspired and guided me through my work and life during my doctoral study in the states. I would also like to thank the members of my committee: Dr. Chang Lu, Dr. Jiangtao Cheng, Dr. Louis A. Madsen and Dr. Zhiting Tian for their time and valuable suggestions on my research and coursework.

I am also very grateful to all the research collaborators, especially Dr. Bobby G. Sumpter, Dr. Jingsong Huang from Oak Ridge National Lab, Professor Alexi Kornyshev at Imperial College in London, Dr. Louis A. Madsen, Dr. Ying Wang at Virginia Tech. The dynamics of the RTILs in nanopores reported in this work was inspired by the previous work of Professor Alexi Kornyshev. And the last part of this dissertation would not exist if not for the ion gel that was first fabricated by Dr. Ying Wang.

I would also like to extend my thanks to my lab mates, Dr. Peng Wu, Dr. Ying Liu, Dr. Xikai Jiang, Dr. Fengchang Yang, Mr. Fei Zhang, Mr. Zhou Yu, Mr. Haiyi Wu, and Mr. Chao Fang. I have learned a lot of research tools from Dr. Peng Wu when I first started my doctoral research. Dr. Fengchang Yang and Mr. Fei Zhang have been great friends and roommates in the past a few years.

I would also like to thank the National Science Foundation for financial support and the staff at the Mechanical Engineering department, especially Ms. Cathy Hill, who has answered many questions and processed tons of forms for me during my study here.

At last, I would like thank my sister and my parents for their love and support throughout my study.

# Table of Contents

	Page
Abstract .....	ii
General Audience Abstract .....	iv
Dedication .....	v
Acknowledgments .....	vi
Table of Contents .....	vii
List of Figures .....	ix
List of Tables .....	xii
Chapter 1 Introduction .....	1
1.1. Background .....	1
1.2. Electrodes and Electrolytes of Electrochemical Devices.....	5
1.2.1. Electrode Materials .....	5
1.2.2. Electrolyte Materials .....	8
1.3. RTILs and RTILs-Based Electrolytes.....	11
1.3.1. RTILs as Liquid Electrolytes .....	12
1.3.2. RTILs-based Polymer Electrolytes .....	15
1.4. Fundamental Understanding RTILs and RTIL-based Electrolytes .....	18
1.4.1. Dynamics of RTILs in nanopores .....	18
1.4.2. Charging Dynamics of RTILs in Nanopores .....	25

1.4.3. RTILs in Ion Gels .....	33
1.5. The Scope of This Dissertation.....	38
Chapter 2 Dynamics of Ions in Nanopores under Charging Relevant Conditions .....	40
2.1. MD Systems and Methods .....	41
2.2. Results and Discussion .....	46
2.3. Conclusions.....	56
Chapter 3 Dynamic Charge Storage in RTIL-filled Nanopores .....	58
3.1. Models, Simulation System and Methods .....	59
3.2. Results and Discussion .....	64
3.2.1. Initial Transients of Cyclic Voltammetry .....	66
3.2.2. Cyclic Charging/discharging and the Underlying Ion Dynamics .....	69
3.2.3. Effects of Scan Rate and Pore Size on Dynamic Charge Storage .....	74
3.3. Conclusions.....	80
Chapter 4 Molecular Mechanics of PBDT Ion Gels.....	83
4.1. Models, Simulation System and Methods .....	84
4.2. Results and discussion .....	91
4.3. Conclusions.....	101
Chapter 5 Conclusions .....	103
References.....	107

# List of Figures

Figure	Page
<b>Figure 1-1.</b> The Ragone plot for several common energy storage devices.....	2
<b>Figure 1-2.</b> A schematic diagram of a battery energy storage system. ....	3
<b>Figure 1-3.</b> A schematic diagram of a supercapacitor system. ....	4
<b>Figure 1-4.</b> A schematic diagram of a fuel cell system.....	5
<b>Figure 1-5.</b> Carbon-based porous materials used as the electrode of supercapacitors.....	6
<b>Figure 1-6.</b> A schematic diagram of a typical polymer electrolyte membrane fuel cell....	8
<b>Figure 1-7.</b> Ionic liquids.....	11
<b>Figure 1-8.</b> Specific capacitance of supercapacitors.....	13
<b>Figure 1-9.</b> Property change of RTILs after the addition of the second RTILs. ....	14
<b>Figure 1-10.</b> Sketches of two types of polymer electrolytes.....	16
<b>Figure 1-11.</b> A novel PBDT ion gel.....	17
<b>Figure 1-12.</b> Mean square displacements (MSDs) of ILs confined inside a slit rutile pore. .....	20
<b>Figure 1-13.</b> MSDs of [EMIM <sup>+</sup> ][TFSI <sup>-</sup> ] confined inside slit graphitic nanopores.....	21
<b>Figure 1-14.</b> Diffusion of RTILs confined in the carbon nanotube at different loadings.	21
<b>Figure 1-15.</b> Diffusion coefficients of [BMIM][BF <sub>4</sub> ] as a function of the temperature. .	22
<b>Figure 1-16.</b> Diffusion of RTILs [C <sub>2</sub> C <sub>1</sub> IM][Cl] inside double-walled carbon nanotube.	23
<b>Figure 1-17.</b> Self-diffusion of ions during the charging of ionophilic pores .....	24
<b>Figure 1-18.</b> Dynamic charging and discharging of supercapacitor using CDC electrodes and RTILs. ....	26
<b>Figure 1-19.</b> Electrode mass change vs charge during the polarization of electrodes. ....	27

<b>Figure 1-20.</b> NMR spectra of electrodes during cyclic voltammetric cycling.....	28
<b>Figure 1-21.</b> Charging of two types of pores under the action of an impulsively imposed voltage.....	30
<b>Figure 1-22.</b> Charging of ionophilic pores.....	31
<b>Figure 1-23.</b> Total charge of the electrodes as a function of time for three systems. ....	32
<b>Figure 1-24.</b> Morphological alignment and structure of the PBDT ion gels. ....	34
<b>Figure 1-25.</b> Structure of the RTIL and charge overscreening near the PBDT rod in an ion gel.....	35
<b>Figure 1-26.</b> Diffusion coefficients of the ions in the PBDT ion gel.....	36
<b>Figure 1-27.</b> Interactions between two charged nanorods immersed in RTILs. ....	37
<b>Figure 2-1.</b> Diffusion coefficient of the EMIM <sup>+</sup> ions using two methods. ....	43
<b>Figure 2-2.</b> MSDs of the TFSI <sup>-</sup> ions confined inside 0.75 nm pores (fast).....	45
<b>Figure 2-3.</b> MSDs of the TFSI <sup>-</sup> ions confined inside 0.75 nm pores (slow).....	45
<b>Figure 2-4.</b> Diffusion coefficients of TFSI <sup>-</sup> ions using two sets of MSDs.....	46
<b>Figure 2-5.</b> Ion diffusion inside a 0.75 nm slit pore.....	47
<b>Figure 2-6.</b> Cage dynamics for EMIM <sup>+</sup> ions.....	50
<b>Figure 2-7.</b> Dynamics of cations at zero charge condition. ....	52
<b>Figure 2-8.</b> Ion diffusion inside a 0.72 nm slit pore.....	53
<b>Figure 2-9.</b> Structures of EMIM <sup>+</sup> and TFSI <sup>-</sup> ions confined inside micropores. ....	55
<b>Figure 2-10.</b> Ion diffusion inside a 1.1 nm slit pore.....	56
<b>Figure 3-1.</b> A schematic of the system used for MD simulations.....	59
<b>Figure 3-2.</b> Radial distribution function (RDF) for the bulk model of RTILs.....	60
<b>Figure 3-3.</b> Density profile of cations across the pore .....	61

<b>Figure 3-4.</b> Charging and discharging of a 0.78 nm-wide electrode pore. ....	66
<b>Figure 3-5.</b> Current and ion density during steady-state charging/discharging cycles. ...	69
<b>Figure 3-6.</b> Current and ion density during steady-state charging/discharging of two pores. .....	71
<b>Figure 3-7.</b> Ionic space charge density during cyclic charging/discharging.....	73
<b>Figure 3-8.</b> Effects of scan rate on the charging/discharging of a 0.78 nm pore. ....	75
<b>Figure 3-9.</b> Variation of ion density during charging of a 0.78 nm-pore.....	77
<b>Figure 3-10.</b> Effects of scan rate on the charging/discharging of a 0.91 nm pore. ....	78
<b>Figure 3-11.</b> Variation of ion density during charging of a 0.91 nm-pore.....	79
<b>Figure 4-1.</b> The structure of the PBDT ion gel. ....	84
<b>Figure 4-2.</b> The molecular system used to study the mechanical properties of PBDT ion gels. ....	85
<b>Figure 4-3.</b> Temperature (a) and potential energy (b) of the system .....	86
<b>Figure 4-4.</b> The simulation box before and after the shear deformation.....	89
<b>Figure 4-5.</b> Formation of the double helix structure using non-periodic PBDT polyanions. .....	91
<b>Figure 4-6.</b> The pencil-in-water box test.....	92
<b>Figure 4-7.</b> Ion charge density distribution in the interstitial space between the PBDT polyanions .....	94
<b>Figure 4-8.</b> The interference of the ionic space charge between two PBDT rods .....	96
<b>Figure 4-9.</b> Charge interference in the PBDT ion gel. ....	98
<b>Figure 4-10.</b> A sketch of a subdomain within an ion gel sample.....	100

# LIST OF TABLES

Table	Page
<b>Table 1-1.</b> Conductivity of some common RTILs and aqueous electrolytes at 25 °C. ....	12
<b>Table 2-1.</b> Number density of ILs inside 0.75 nm pore. ....	41
<b>Table 2-2.</b> Number density of ILs inside 0.72 nm pore. ....	42
<b>Table 2-3.</b> Number density of ILs inside 1.1 nm pore. ....	42
<b>Table 4-1.</b> The displacement applied at the boundary of the simulation system. ....	87
<b>Table 4-2.</b> Stiffness constants and modulus of the model ion gel studied in this work. ..	93

# CHAPTER 1

## Introduction

### 1.1. Background

The modern society is still primarily fueled by fossil fuels. In 2016, about 78% of U.S. electricity is generated using fossil fuels, i.e. natural gas, coal, petroleum etc<sup>1</sup>. In order to convert fossil fuels to electricity, the fuel is burned in a furnace to heat water in boiler to produce steam. However, the combustion process generates a significant amount of CO<sub>2</sub>, a greenhouse gas that leads to global warming<sup>2</sup>. Furthermore, at the current consumption and compound rate, it is estimated that the fossil fuel reserve will be depleted in about one century<sup>3</sup>. To avoid the continuing of global warming and deal with the decreasing availability of fossil fuels, it is crucial that the society should move from the fossil fuels towards sustainable and renewable energy sources. Besides, replacing the traditional internal-combustion engine vehicles with the electric vehicles could also help to reduce the consumption of fossil fuels and curb greenhouse gas emissions.

Renewable energy sources including wind<sup>4</sup>, solar<sup>5</sup> and ocean waves<sup>6</sup> energies provide about 15% of U.S. electricity<sup>1</sup> in 2016. One major drawback of the renewable energy, which contributes to their limited deployment, is the intermittence of the energy source, e.g., no electricity could be generated from solar source at night and the wind at a wind farm could change hourly<sup>7</sup>. Therefore, in order to effectively use these energy sources and provide reliable and stable power to the grid, electrical energy storage devices become important. Generally, electricity generated from renewable sources can be first stored in energy storage device, which will later be released to provide reliable and stable electricity supply even if the energy source is intermittent. Besides,

the development of the electrical energy storage devices in recent years has also boosted the development of the environment-friendly commercial products, such as electrical vehicles. Many different approaches can be used for developing electrical energy storage systems, and those relied on electrochemical principles, e.g., batteries, supercapacitors and fuel cells, have received significant attention due to their advantages such as reliability, compactness and cost-effectiveness.

Energy density and power density are two of the most important performance metrics of electrochemical energy storage devices. High power density and energy density are desired in many applications. For example, long-lasting and high-power batteries are essential for smart phones. The Ragone plot in Figure 1-1 compares the performance of several common electrical energy storage devices. A brief introduction of these devices is provided below.

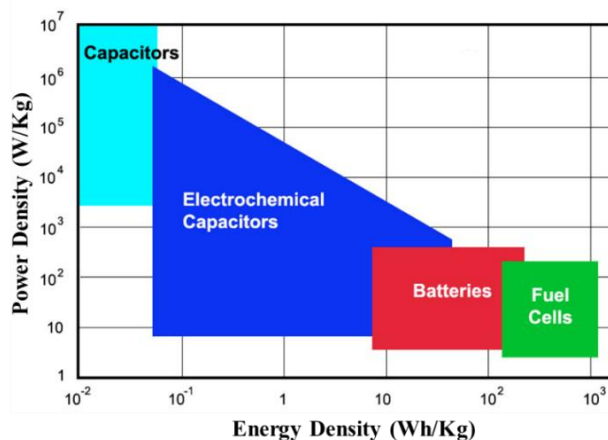


**Figure 1-1.** The Ragone plot for several common energy storage devices. Source: U.S. Department of Energy, basic research needs for electrical energy storage<sup>8</sup>, 2007.

Battery energy storage system is one of the most widely used electrical energy storage system in industry and daily life. As shown in Figure 1-2, a battery usually consists of one or more electrochemical cells connected in serial or parallel. Each battery cell consists of two electrodes connected by electrolyte which could be at solid or liquid state<sup>9-10</sup>. A cell converts energy between

electrical energy and chemical energy through electrochemical reactions. Batteries often have high energy density and moderate power density.

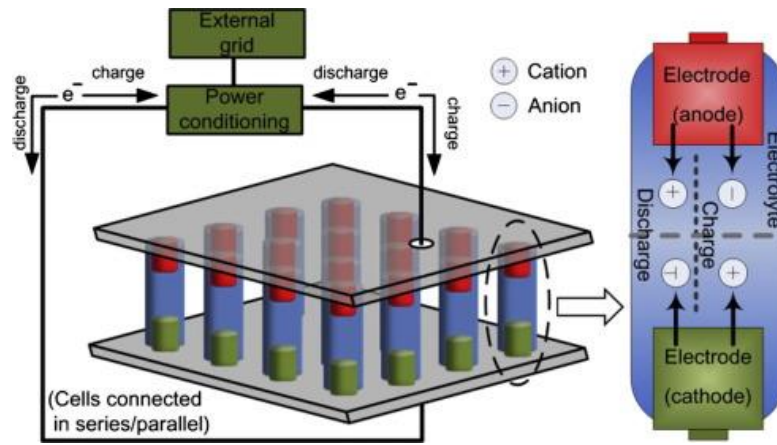


**Figure 1-2.** A schematic diagram of a battery energy storage system. The figure is reprinted from Ref. 11.

Supercapacitors are also known as electrochemical capacitors (ECs) or electrical double-layer capacitors (EDLCs). As shown in Figure 1-3, supercapacitors are typically composed of porous electrode, separator and electrolyte<sup>12</sup>. During the charging process, positive/negative electrode carrying positive/negative charges would attract ions in the electrolyte carrying the opposite charges. Due to the variation of the electric potential near the electrode surface, a layer of ions will be adsorbed onto the electrode surface. This layer of ions adjacent to the electrode surface and the electrical charge on the electrode surface form an electrical double layer (EDL), and store the electrical energy. Compared to traditional dielectric capacitors, the capacitance of supercapacitors could be orders of magnitude higher<sup>13</sup>. Supercapacitors fill the gap between traditional dielectric capacitors and batteries, i.e. it has high power density and decent energy density; however, in order to break into the mainstream market, the energy density of supercapacitors must be significantly improved.

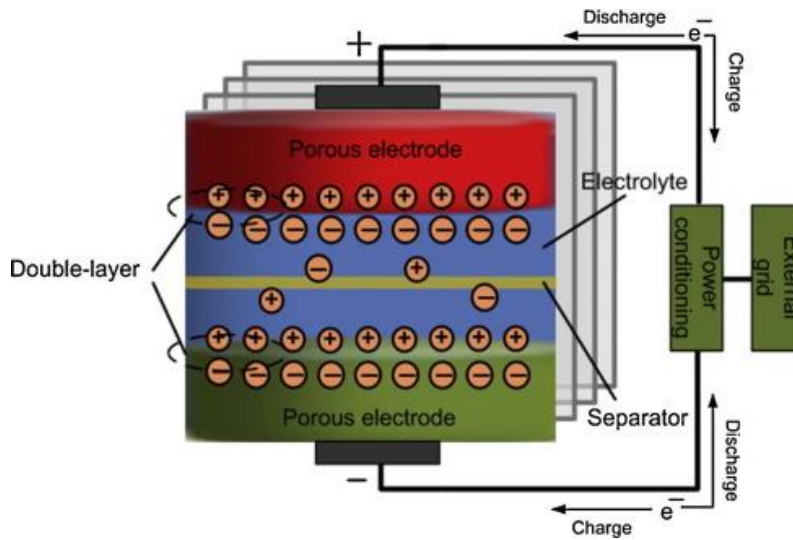


**Figure 1-3.** A schematic diagram of a supercapacitor system. The figure is reprinted from Ref. 11.

Fuel cells convert chemical energy of the fuel into electricity through electrochemical reactions. Unlike batteries, fuel cells do not need recharging; instead, the electricity will be produced as long as fuel is provided. There are many types of fuel cells, such as the alkaline fuel cell (AFC), polymeric-electrolyte-membrane fuel cell (PEMFC), molten-carbonate fuel cells (MCFCs), solid-oxide fuel cells (SOFCs) *et al.* For a fuel cell using hydrogen and oxygen as the reactant, the fuel (hydrogen molecules) is separated into protons (hydrogen ions) and electrons at the anode<sup>12, 14</sup>. The protons migrate through the electrolyte membrane to react with the oxygen at the cathode, while the electrons go through an external circuit to create a flow of electricity. The only products of this process are electricity, water and heat. Fuel cells can be integrated with other devices for energy storage. As shown in Figure 1-4, the power generated from an external grid (e.g. from a renewable source) can be first used to split water, and the resulting hydrogen gas is stored. Then the hydrogen is fed to the fuel cell as the fuel, and the resulting electricity from fuel cell to the external grid will be stable.

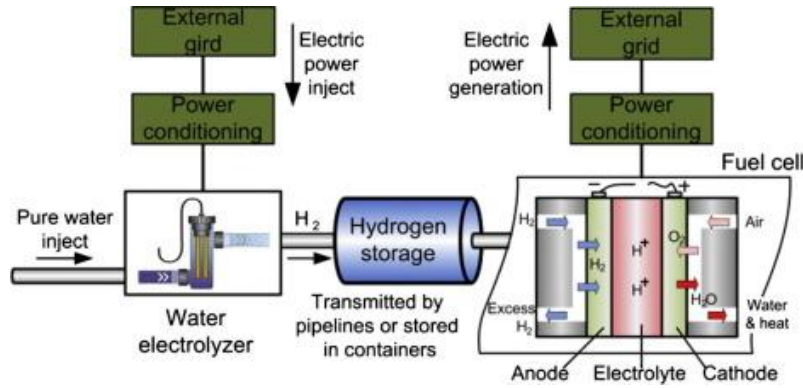


**Figure 1-4.** A schematic diagram of a fuel cell system. Figures are reprinted from Ref. 11.

## 1.2. Electrodes and Electrolyte of Electrochemical Devices

The increasing demand for electrochemical energy storage devices has led to intensive research aiming to improve their energy and power densities. Much of these researches focus on development and application of new electrode and electrolyte materials in these devices. Because electrode and electrolyte function differently in different electrochemical devices, these devices also have different requirements for these materials. Below is a brief introduction of the recent progress on the development of electrode and electrolyte materials for electrochemical energy storage devices.

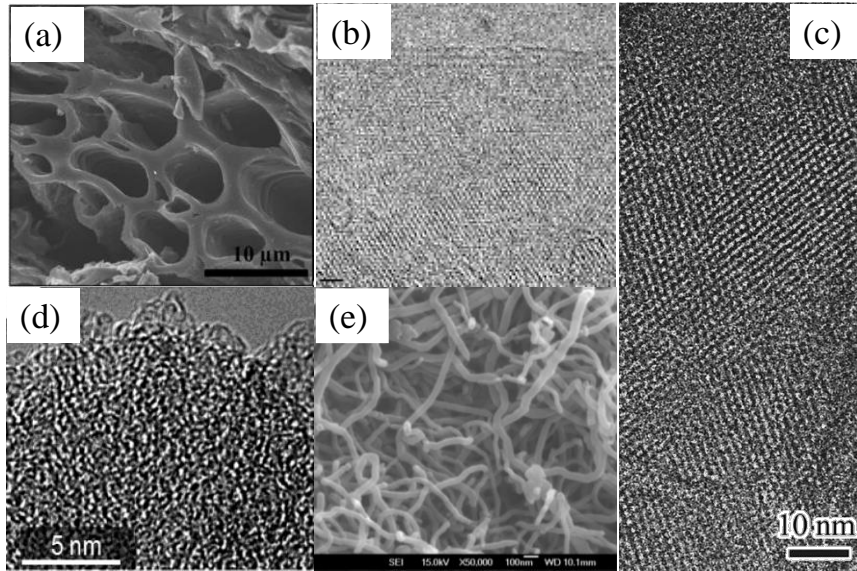
### 1.2.1. Electrode Materials

The power and energy density of electrochemical energy storage devices depend on the electrodes used in these devices. For example, prior work<sup>15-16</sup> has shown that the energy and power density of supercapacitors are given by

$$E = c \times \frac{V^2}{2} \times SSA \quad (1-1)$$

$$P = V^2/4R_s \quad (1-2)$$

where  $c$  is capacitance,  $V$  is the operation voltage,  $SSA$  is the specific surface area of the electrode and  $R_s$  is effective internal resistance of the supercapacitors. And it is further established that these parameters are mostly affected by the selection of electrode and electrolyte materials<sup>8, 15-17</sup>. As shown in Equation 1-1, the energy density of the supercapacitors could be improved by increasing the specific surface area of the electrode. For this reason, porous materials featuring fine pores are generally used as the electrode of supercapacitors. In particular, carbon-based porous materials are the most popular choices because of their low cost, high electrical conductivity, and excellent thermal stability<sup>15-16, 18-19</sup>.



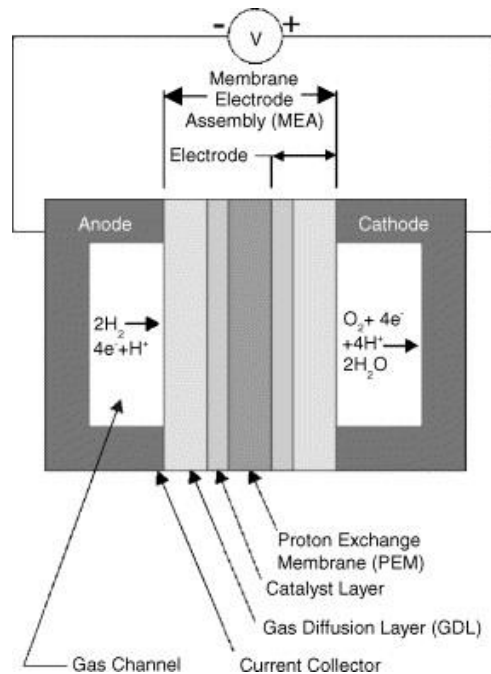
**Figure 1-5.** Carbon-based porous materials used as the electrode of supercapacitors. (a) Field emission scanning electron microscopy (FESEM) image of activated carbons. Figure is reprinted from Ref. 20. (b) Transmission electron microscopy (TEM) image of graphene. Figure is reprinted with permission from Ref. 21. Copyright 2007 Springer Nature. (c) High-resolution transmission electron microscopy (HRTEM) image of zeolite Y templated carbon. Figure is reprinted with permission from Ref. 22. Copyright 2001 American Chemical Society. (d) HRTEM image showing the microstructure of carbon derived-carbon. Figure is reprinted with permission from Ref. 23. Copyright 2010 American Chemical Society. (e) The SEM image of the multiwall carbon nanotube. Figure is reprinted from Ref. 24.

Figure 1-5 shows the images of some carbon-based porous electrode materials for supercapacitors, including activated carbon<sup>25</sup>, templated carbon<sup>17</sup>, carbide-derived carbon<sup>23</sup>, carbon nanotube<sup>26</sup> and graphene<sup>27</sup>. Using these carbon-based materials energy densities of 3-130 Wh/kg have been reported for supercapacitors.

The performance of batteries is also greatly related to the properties of their positive/negative electrodes<sup>28</sup>. The development of cathode and anode materials with nanoscale features for rechargeable batteries (especially the Li-batteries) has led to improvements over the years, e.g., longer cycle life, higher electrode/electrolyte contact area, capability in operating at higher power, and reduced transport resistance for Li<sup>+</sup> ions<sup>29</sup>. Using Li-ion batteries as an example, lithium metal alloys and nano-sized transition metal oxides (TMOs) have been found to be promising candidates for the anode<sup>30</sup>. Lithium metal alloys are attractive for their capability of accommodating high amount of lithium<sup>30</sup>, while the use of nano-sized TMOs enhances the surface electrochemical reactivity and further leads to improvement of device performance<sup>31</sup>. At the cathode side, three types of materials have been explored extensively: layered oxides such as LiCoO<sub>2</sub>, spinels such as LiMn<sub>2</sub>O<sub>4</sub>, and olivines such as LiFePO<sub>4</sub><sup>32</sup>. Additives have been shown to improve the performance of base materials, e.g., combining LiFePO<sub>4</sub> with electronic conductors like carbon nanotubes<sup>33</sup> and graphenes<sup>34-35</sup> improves the specific capacity, rate capability and cycle life of cathodes.

For fuel cells, the membrane electrode assembly (MEA) is its core component. There has been extensive work on the electrodes of different types of fuel cells. For symmetrical solid oxide fuel cells (SSOFCs), perovskite materials such as Sr<sub>2</sub>Fe<sub>1.5</sub>Mo<sub>0.5</sub>O<sub>6-δ</sub> have been investigated as the electrode<sup>36</sup>, but the cell performance is usually not as good as the SOFCs. For PEMFCs, a typical MEA is composed of the polymer electrolyte membrane (PEM), the catalyst layers, and the gas

diffusion layers. One way of fabricating MEA is coating the catalyst layer on the PEM. Another approach is to have the catalyst layers and the gas diffusion layers as the electrodes of the fuel cell, while the PEM is sandwiched between the electrodes as shown in Figure 1-6. Therefore, an electrode provides the interface between the fuel gases and the electrolytes, which means the electrode must allow wet gas permeation and provide a reaction surface. At present, the most common design for electrode of PEMFC is the thin-film design that binds carbon supported catalyst particles<sup>37</sup>.



**Figure 1-6.** A schematic diagram of a typical polymer electrolyte membrane fuel cell. The membrane electrode assembly (MEA) is the core component of the fuel cell and composed of the proton exchange membrane (PEM) sandwiched by the electrodes (combination of gas diffusion layers and catalyst layers). Figure is reprinted with permission from Ref. 37. Copyright 2004 Elsevier.

### 1.2.2. Electrolyte Materials

In electrochemical devices, electrolytes usually play a dual role: as an ionic conductor so that ion transport is facile and as the electronic insulator to prevent short circuiting and self-

discharging<sup>38-40</sup>. The general requirements for an ideal electrolyte of electrochemical devices include the followings: wide electrochemical window, high ionic conductivity, high chemical and electrochemical stability, low volatility and flammability, being environmentally friendly, and low cost<sup>38-40</sup>. As the electrolytes work differently in different electrochemical devices, some additional properties are desired for the electrolyte in different devices.

For the supercapacitors, the ions accumulated near electrodes works as the charge to be stored. From Equations 1-1 and 1-2, it is obvious that high operation voltage and low internal resistance are desired for the electrolytes of supercapacitors. This is because both energy density and power density are proportional to the square of the operating voltage and power density is inversely proportional to the internal resistance. There are generally three types of electrolytes for supercapacitors: aqueous electrolytes, organic electrolytes and room-temperature ionic liquids (RTILs). Aqueous electrolytes can have high ion concentration and ionic conductivity, but their operation voltages are rather low due to the thermodynamic decomposition of water at  $\sim 1$  V<sup>16</sup>. Organic electrolytes allow a relatively higher operation voltage in the range of 3-3.5 V, but they come with a higher cost, lower conductivity, and safety concerns due to their flammability and toxicity<sup>16, 18</sup>. RTILs have a wide electrochemical stability window ranging from 2 to 6 V, superior thermal and chemical stability, low flammability and a decent conductivity<sup>18</sup>. Therefore, RTILs have been received tremendous attention in the supercapacitor community.

In batteries and fuel cells, electrolyte usually serves as the medium where ions migrate from one electrode to the other, allowing the chemical reactions to happen at certain terminals. One of the big challenges for fuel cell and battery electrolytes is the stability requirement, that is, the electrolyte need to be stable in both the highly reducing environment of the anode and the highly oxidizing environment of the cathode<sup>39-40</sup>.

For rechargeable batteries, many electrolytes have been adopted, e.g., non-aqueous and aqueous electrolytes, RTILs, polymer electrolytes and hybrid electrolytes<sup>39</sup>. Currently the most widely used electrolytes are non-aqueous organic solutions. Aqueous electrolyte has a good ionic conductivity but a relatively low operation voltage at  $\sim 1.23$  V. RTILs seem promising, but their application is still in an early stage and their relatively low ionic conductivity remains a major concern. While liquid electrolytes dominate the application in batteries, polymer electrolytes also receive much attention because they provide a safer operation, better mechanical stability without the leakage, and avoid the volatility or flammability issues usually associated with liquid-based electrolytes. The polymer electrolytes could be further classified into solid polymer electrolytes and gel polymer electrolytes<sup>39</sup>. However, current polymer electrolytes suffer from a low ionic conductivity.

There are four major candidates for the electrolytes of fuel cells: aqueous electrolytes, RTILs, polymer electrolytes and ceramic electrolytes. For aqueous/RTILs electrolytes, a matrix material is used to provide mechanical strength to the electrolyte and prevent fuel crossover. For a polymer to be used as the electrolyte, it must provide a good ion conductivity and mechanical strength. Ceramic electrolyte are mainly used in solid oxide fuel cells (SOFC), and the most popular SOFC electrolyte is the yttria-stabilized zirconia (YSZ)<sup>40</sup>.

Overall, an emerging trend in electrochemical devices is that RTILs and materials based on them are increasingly being used as electrolytes. In the following section, a more detailed review of RTILs (and RTILs-based electrolytes) and their applications in electrochemical devices is presented.

### 1.3. RTILs and RTILs-Based Electrolytes

As shown in Figure 1-7, ionic liquids (ILs) are molten salts composed completely of ions<sup>41</sup>. By carefully choosing the cations and anions of the IL, it is possible to obtain ILs that remain in the liquid state at and below room temperature, i.e., RTILs<sup>42-43</sup>. Since RTILs show a great combination of properties such as high ionic conductivity, wide electrochemical window, low vapor pressure, and good thermal stability<sup>44</sup>, they are suitable for electrochemical devices such as batteries and supercapacitors.

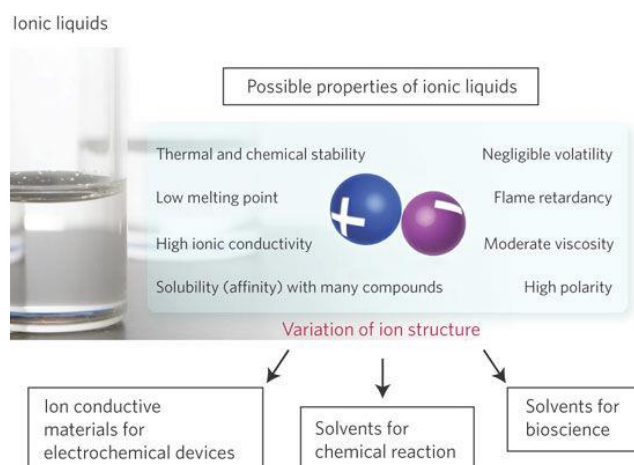


**Figure 1-7.** Ionic liquids. ILs are molten salts completely composed of ions. They have potential applications such as electrolytes of electrochemical devices, solvents for chemical reactions and bioscience. Figures are reprinted with permission from Ref. 45. Copyright 2009 Springer Nature.

Currently one of the main arguments against the use of RTILs as electrolyte is the cost. However, it is estimated that the price of RTILs would drop significantly if the production has surpassed a certain level<sup>46</sup>. Another limitation of the RTILs and RTILs-based electrolytes is their relatively low conductivity compared to aqueous electrolytes (see Table 1-1).

Nevertheless, in recent years, RTILs has been intensively investigated as the electrolyte or electrolyte components in electrochemical devices. In particular, there has been much work on

using the RTILs as electrolytes in supercapacitors, aiming to improve the energy density of the device by increasing its operation voltage. Even though these applications generally still suffer from the relatively low conductivity of RTILs, recent work has shown some promising results when combining RTILs with nanoporous electrodes.

**Table 1-1.** Conductivity of some common RTILs and aqueous electrolytes at 25 °C.

Compound	Conductivity (Scm <sup>-1</sup> )	Ref.
emimCl(60%)-AlCl <sub>3</sub>	0.0065	47
emim CF <sub>3</sub> CO <sub>2</sub>	0.0032	47
bupy BF <sub>4</sub>	0.0019	47
emim[(CF <sub>3</sub> SO <sub>2</sub> ) <sub>2</sub> N]	0.0057	47
0.1M aq. KCl	0.013	48

Besides, by introducing RTILs to traditional polymer electrolytes, new polymer electrolytes containing RTILs can be fabricated. These novel solid and gel polymer materials show better mechanical strength than the traditional polymer electrolytes, as well as providing a much higher ionic conductivity and thermal stability. Some of these gel materials have anisotropic ionic conductivity and modulus<sup>49</sup> along a pre-determined direction, which are beyond the reach for most known ion gels but are appealing in many applications<sup>50,51</sup>.

### 1.3.1. RTILs as Liquid Electrolytes

As it has been reviewed in the previous section, RTILs has been investigated as the electrolyte in various applications, including batteries, supercapacitors and fuel cells. As the main concern of the first parts of this dissertation, recent work regarding RTILs as electrolytes of supercapacitors is reviewed in this section. The traditional electrolytes of supercapacitors have limited their development due to their low operation voltage. In the last a few years, in order to

further improve the energy density, much work has been done to develop electrolytes for supercapacitors that enable higher operation voltages. Among the proposed electrolytes, RTILs are considered as the most promising candidate due to their wide electrochemical window<sup>52</sup>.

Two main families of RTILs have been used as electrolytes for supercapacitors, i.e. RTILs based on pyrrolidinium<sup>53</sup> and imidazolium<sup>54</sup>. The pyrrolidinium-based RTILs generally show a larger electrochemical window, while the imidazolium-based RTILs usually display a higher conductivity. These different characteristics would affect the performance of supercapacitors containing these RTILs. Due to the higher operation voltage, these RTILs-based supercapacitors display energy densities significantly higher than those of conventional systems. However, due to the relative high viscosity of these electrolytes and the use of nanoporous electrode material, the internal resistance of these electrolytes can potentially be much higher than that of conventional electrolytes. As a consequence, the power density can be compromised. To deal with this situation, mixture electrolytes containing RTILs appear to be a convenient way to take advantage of the beneficial properties of RTILs.

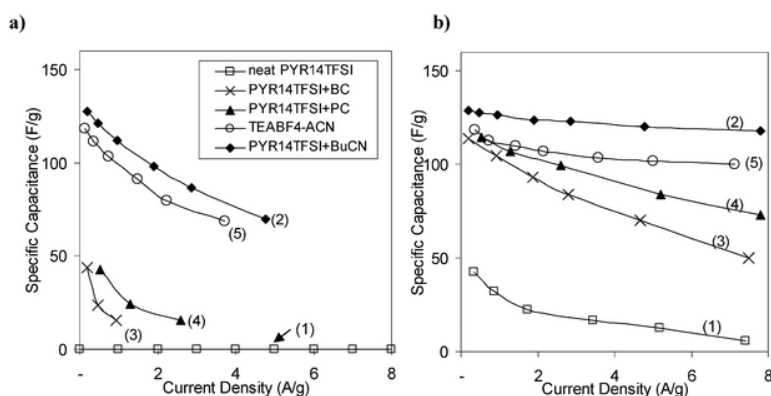


**Figure 1-8.** Specific capacitance of supercapacitors. The capacitance was measured at different temperatures using different electrolytes. (a) -20 °C, (b) 25 °C. Electrolytes used: (1) neat IL, (2) IL-BuCN, (3) IL-BC, (4) IL-PC and (5) 1 M TEABF4-CAN. Voltage window: 2.5 V. Figures are reprinted with permission from Ref. 53. Copyright 2012 Royal Society of Chemistry.

The conductivity of the pyrrolidinium-based ionic liquid could be increased by mixing it with other solvents. It has been reported<sup>53</sup> that the conductivity of an RTIL, N-butyl-n-methylpyrrolidinium bis(trifluoromethane sulfonyl) imide (PYR<sub>14</sub>TFSI) was increased from 2.48 mS cm<sup>-1</sup> to 8–45 mS cm<sup>-1</sup> by mixing with an appropriate nitrile or carbonate-based solvents without compromising their electrochemical windows (~4-6 V). As shown in Figure 1-8, this mixture was also shown as an excellent electrolyte for supercapacitors in terms of specific capacitance. In particular, the IL-butyronitrile (BuCN) mixture provided higher capacitance (~125 F g<sup>-1</sup> at 500 mA g<sup>-1</sup>; independent of the testing temperature) and superior performance at high current rates, than both the commercially employed electrolytes in supercapacitors (1 M TEABF<sub>4</sub>-acetonitrile) and the neat RTIL.

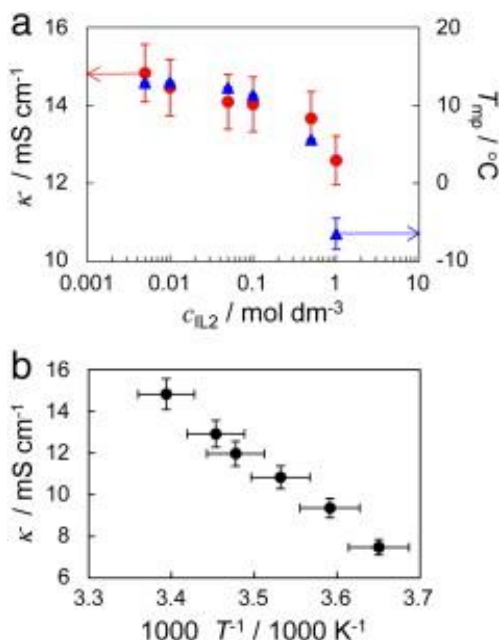


**Figure 1-9.** Property change of RTILs after the addition of the second RTILs. (a) The bulk conductivity (circles) and melting point (triangles) of EMImBF<sub>4</sub> change after the addition of BMImBF<sub>4</sub>. (b) Bulk conductivity of EMImBF<sub>4</sub> + 1 M BMImBF<sub>4</sub> mixture as a function of the temperature. Figures are reprinted with permission from Ref. 54. Copyright 2012 Elsevier.

By mixing two different ILs, the properties of RTILs could be further tailored. As shown in Figure 1-9, noticeable lowering of the melting point (from 13.5 °C to 5.6 °C) of the bulk 1-ethyl-3-methylimidazolium tetrafluoroborate (EMImBF<sub>4</sub>) electrolyte has been achieved by adding a relatively small amount ( $c_{IL2}=0.5$  M) of 1-butyl-3-methylimidazolium tetrafluoroborate (BMImBF<sub>4</sub>), while the conductivity changes only slightly<sup>54</sup>. It has also been reported that<sup>54</sup>, at lower concentration ( $c_{IL2}\leq 0.5$  M), the addition of BMImBF<sub>4</sub> does not remarkably influence the performance of the supercapacitors, with a capacitance of 135 F g<sup>-1</sup> at 3.2 V, energy density of 49 Wh kg<sup>-1</sup>, and power density of 38 kW kg<sup>-1</sup>.

Even though mixing ILs with organic solvents or new type of ILs seems to be a suitable strategy to improve the conductivity of the IL electrolytes, there are still some limitations. For example, when mixing two ILs, supercapacitors sometime show lower rate capability even at room temperature<sup>54</sup>. Recently, it has been shown that fast charging (hence high power density) can be achieved by combining RTILs with sub-nanometer pores<sup>55-57</sup>, which offers hope that one can enhance the energy density of supercapacitors using these materials while maintaining satisfactory power density. The related work will be reviewed in Section 1.4.1.

### **1.3.2. RTILs-based Polymer Electrolytes**

A major drawback of using liquid-state RTILs as electrolytes in electrochemical devices is the leakage issue, which requires a thorough device encapsulation. Besides, in applications like the fuel cells, liquid electrolyte will require an additional matrix material to provide mechanical strength to the electrolyte and prevent fuel crossover. In these cases, solid or quasi-solid electrolytes such as polymer electrolytes have important advantages including mechanical stability, safety, and simple processing<sup>58</sup>. Traditionally, polymer electrolytes are divided into two main

categories<sup>58</sup>: solid polymer electrolytes (SPEs) and gel polymer electrolytes. SPEs are generally composed of a polymer matrix and a salt, while the gel polymer electrolytes are composed of a polymer matrix, a salt and an organic solvent. The latter usually shows a higher conductivity because of the faster ion transport due to the presence of organic solvents in the polymer matrix.

In recent years, the scope of polymer electrolytes have been extended due to the introduction of RTILs into this area<sup>58</sup>. Bulk polymeric ionic liquids (PILs) or poly(ionic liquids) are also considered as the SPEs. In these polymeric ionic liquids, no additional salts are added. Depending on the backbone of the PILs, the transport of the counter-cations or counter-anions is responsible for their ionic conductivity. In order to further increase the conductivity of SPE, a novel gel type polymer electrolyte could be prepared by introducing ILs. In this type of gel electrolytes, organic solvents are replaced by ILs. This ion gel can be prepared using PILs or different types of polymeric matrices. Figure 1-10 shows graphical representations of the SPEs poly(ionic liquid)s and the ion gels.

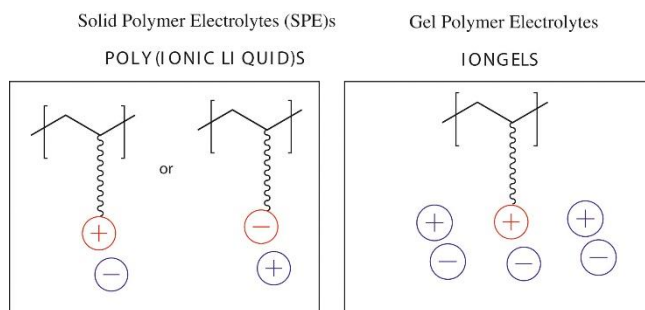


**Figure 1-10.** Sketches of two types of polymer electrolytes. The left panel shows the SPEs poly(ionic liquid)s and right panel shows the ion gels. Figures are reprinted with permission from Ref. 58. Copyright 2015 Elsevier.

Ion gels are promising candidates for next generation electrolytes due to features such as high ion mobility, excellent thermal stability, high mechanical integrity and excellent electrode-electrolyte contact<sup>59-62</sup>. A recent breakthrough in this field is the synthesis of liquid crystalline (LC)

ion gels containing rigid-rod polyanionic aramid poly(2,2'-disulfonyl-4,4'-benzidine terephthalamide (abbreviated **PBDT**) and a RTIL 1-ethyl-3-methyl imidazolium trifluoromethanesulfonate ( $[\text{C}_2\text{mim}][\text{TfO}]$ )<sup>49</sup>. The formation scheme of the gel, a schematic of the dried gel, and the gel with water present are shown in Figure 1-11. The PBDT LC ion gel is fabricated by the ion exchange between the IL in the top and the PBDT aqueous seed solution in the bottom under a magnetic field. The dried gels exhibit high ionic conductivity (up to  $8 \text{ mS}\cdot\text{cm}^{-1}$  at room temperature), widely tunable modulus (0.003 - 3 GPa), excellent thermal stability (up to  $300^\circ\text{C}$ ), and transport anisotropy (up to  $3.5\times$ ). The combination of strong modulus and high ionic conductivity makes it an ideal candidate for electrolyte in electrochemical devices such as batteries, and the anisotropic ionic mobility and modulus could further expand its applications. The fabrication of this ion gel opens up exciting new avenues for engineering polymer electrolyte materials. In the following section, some recent work on this novel ion gel is reviewed.

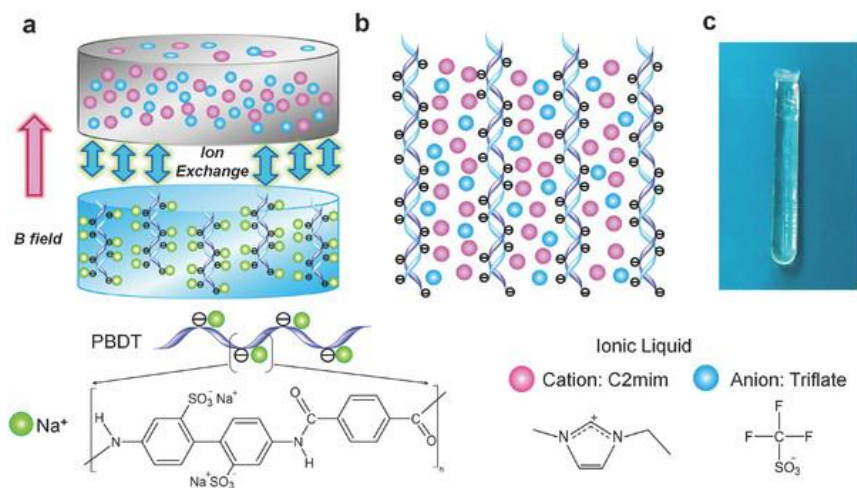


**Figure 1-11.** A novel PBDT ion gel. (a) Fabrication of the PBDT LC ion gel through ion exchange between ILs in the top and the PBDT seed solution in the bottom under a magnetic field  $B$ . PBDT is a rigid-rod sulfonated aramid anionic polymer. The ILs are  $[\text{C}_2\text{mim}][\text{TfO}]$ . (b) Schematic of molecular structure of dried PBDT IL gels in which ILs are dispersed between aligned PBDT polyanions. (c) A picture of the as-prepared PBDT ion gel. Figures are reprinted with permission from Ref. 49. Copyright 2016 John Wiley and Sons.

## **1.4. Fundamental Understanding RTILs and RTIL-based Electrolytes**

To improve the power density of the supercapacitor featuring RTILs, a thorough understanding of the dynamics and charging dynamics of RTILs confined in nanopores is required. Likewise, to improve the transport and mechanical properties of the novel PBDT ion gels, a fundamental understanding of the structure and dynamics of the RTILs confined between the polyanions with spacing on order of a few nanometers is essential. Here, some key insights on the diffusion and charging dynamics of RTILs in nanopores from both experiments and theoretical simulations, as well as theoretical works on the novel PBDT gel are reviewed. At the end of each review section, key open issues are outlined.

### **1.4.1. Dynamics of RTILs in nanopores**

By replacing conventional electrolytes (aqueous electrolytes or organic electrolytes) with room-temperature ionic liquids (RTILs), which have much wider electrochemical window compared to conventional electrolytes, the energy density of supercapacitors has been improved greatly<sup>63</sup>. Likewise, using porous electrodes with narrow pores helps improve the specific surface area available for energy storage and thus the energy density of supercapacitors<sup>64</sup>. Thanks to the intensive research in recent years, the mechanisms of charge storage in these materials under equilibrium conditions are now reasonably understood<sup>15, 65-73</sup>. There is, however, a significant concern that the enhanced energy density of supercapacitors achieved using these new materials may come at the cost of reduced power density. In fact, the power density of RTIL-based supercapacitors is often lower compared to those based on aqueous or organic electrolytes (see Ref. 52 for a review), and this is especially true when RTILs are used together with porous electrodes with mesopores (diameter > 2 nm) or micropores (diameter < 2 nm) that are the most

promising for achieving high energy density. Following conventions in the literature, electrodes featuring mesopores or micropores are referred to as nanoporous electrodes since these pores all have diameters on the order of  $10^{-9}$  m. A comprehensive understanding of the origins of the limited power density of current supercapacitors based on RTILs and nanoporous electrodes is lacking.

Conceivably, the slow transport of bulky RTIL ions in narrow pores and in bulk electrolyte could lead to sluggish charging/discharging and thus limited power density. However, other factors, e.g., ineffective device fabrication and packing, may also be implicated. Because of the limited understanding on this important issue, supercapacitor manufacturers often limit the size of electrode powder to preserve power density, which in turn sacrifices the volumetric capacitance and electrical conductance of the electrode. A possible way to improve the rate capability (and thus power density) is to use hierarchical porous electrodes with both micro- and mesopores<sup>74-75</sup>. To facilitate the development of these materials, it is critical to obtain a fundamental understanding of RTILs transport in micro- and mesopores.

Much of the prior studies of dynamics of RTILs in nanoporous electrodes focused on the self-diffusion of RTIL ions inside mesopores (diameter  $> 2$  nm)<sup>76-80</sup>. For example, Huang *et al.* investigated the dynamics of the ionic liquid [EMIM][TFSI] inside a rutile slit nanopore of width  $H = 5.2$  nm at 333K using the molecular dynamics simulations<sup>78</sup>. The mean square displacement (MSD) of the ions in the direction parallel to the rutile walls are shown in Figure 1-12. While the ions in the center of the pore have faster dynamics than the ions near the pore walls, the diffusion is generally slower than that in the bulk RTILs ( $D_{bulk}$  is on the order of  $10^{-10}$  m<sup>2</sup>/s). It should be noted that the  $\rho \sim \rho_{bulk}$  lines in the figures exhibit the MSDs of ions packed between the electrodes at a bulk density, not the MSDs of ions in bulk RTILs.

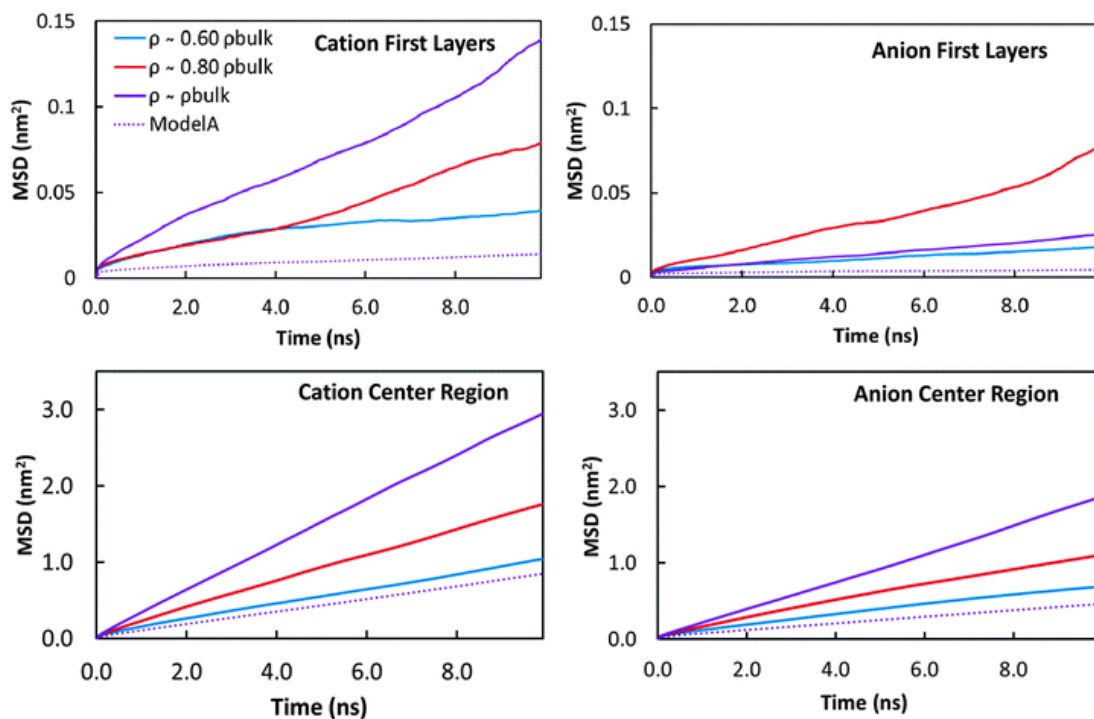


**Figure 1-12.** Mean square displacements (MSDs) of ILs confined inside a slit rutile pore. MSDs of cations (anions) are shown in the left panel (right panel). Pore width is  $H = 5.2$  nm. The MSDs reported are in the direction parallel to the rutile walls ( $x$  and  $y$  directions), for the ions in the first layers (close to the pore walls, top panel) and in the center region of the pore (bottom panel). The parallel component of the MSD of all confined ions (dashed lines) at different pore loadings is also shown. Figures are reprinted with permission from Ref. 78. Copyright 2013 Royal Society of Chemistry.

In another work by Huang *et al.*, they investigated the dynamics of the RTILs [EMIM<sup>+</sup>][TFSI<sup>-</sup>] confined inside a slit-like graphitic pore at 333 K<sup>80</sup>. In these simulations, they investigated systems with different the pore width  $H = 1.9, 2.5, 4.0$  and  $5.2$  nm while the density of the RTILs was maintained at the bulk value ( $\sim 1.56$  g cm<sup>-3</sup>). Figure 1-13 shows the parallel component of the MSDs of the RTILs confined inside the slit pore. When the pore width is  $5.2$  nm, the MSD of the cation is similar to that in the bulk, while the MSD of the anion is still smaller than that in the bulk. In narrower pores, much slower dynamics of the ions are observed. They further investigated the dynamics of the ions in the  $z$ -direction (perpendicular to the pore wall), and found even smaller MSDs in the  $z$  direction than that in the parallel directions ( $x$  and  $y$ ).

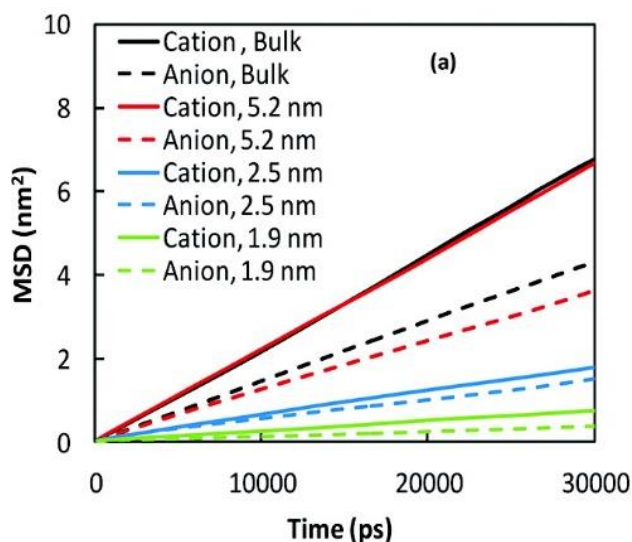


**Figure 1-13.** MSDs of [EMIM<sup>+</sup>][TFSI<sup>-</sup>] confined inside slit graphitic nanopores. The parallel component ( $x$  and  $y$ ) of the MSDs of the ILs inside the slit pore is compared with the bulk value. Pore widths are 1.9, 2.5, and 5.2 nm respectively. Temperature is 333 K. In all cases,  $\rho = \rho_{bulk}$ . Figure is reprinted with permission from Ref. 80. Copyright 2012 American Chemical Society.

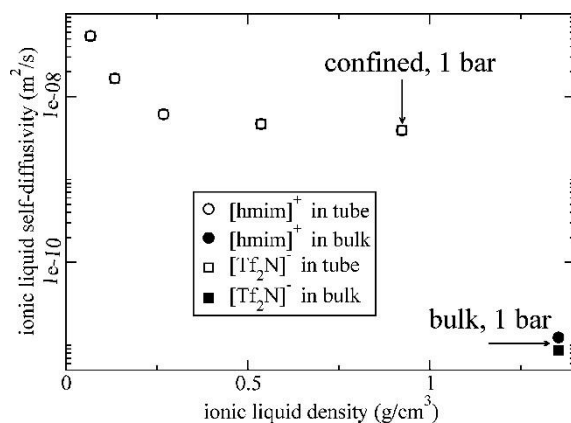


**Figure 1-14.** Diffusion of RTILs confined in the carbon nanotube at different loadings. ILs is [hmim][Tf<sub>2</sub>N]. Temperature is 313 K. The loadings correspond to 5, 10, 20, and 40 pairs of ionic liquid molecules inside the nanotube. Length of the CNTs (20,20) is 95.921 Å. The tube length is 83.623 Å for a loading of 60 pairs of ILs molecules. The axial pressure tensor  $P_{zz}$  is about 1 bar. The diffusion coefficients of the bulk ionic liquid are also shown in the figure. Figure is reprinted with permission from Ref. 81. Copyright 2010 American Chemical Society.

While the transport of ions in these mesopores is mostly slower than that in bulk RTILs, the opposite trend has also been observed both in simulations and experiments<sup>81-82</sup>. Shi *et al.*

investigated the dynamics of the RTILs 1-n-hexyl-3-methylimidazolium bis(trifluoromethylsulfonyl)amide ([hmim][Tf<sub>2</sub>N]) confined into (20, 20) and (9, 9) carbon nanotubes (CNTs) using molecular dynamics simulations<sup>81</sup>. Figure 1-14 shows the comparison of the self-diffusivity of the ionic liquid inside the (20, 20) CNTs (diameter ~2.7 nm) and their bulk value at 313 K. The diffusivity of the ions decreases gradually as the loading in the CNTs increases, however, even when the pressure in the axial direction reaches 1 bar, the diffusivity of the ILs is still 300-400 times larger than the bulk value. They further investigated the diffusion of the ILs at 573 K and 1 bar, and found the confined IL in the CNTs diffuses about 14 times faster than in the bulk ILs. In this work, they attribute the fast dynamics of the ILs in CNTs to the weaker interactions among the ions under confinement.

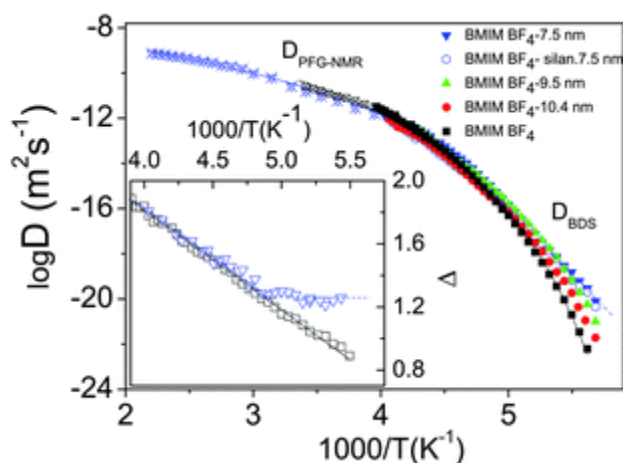


**Figure 1-15.** Diffusion coefficients of [BMIM][BF<sub>4</sub>] as a function of the temperature. The diffusion coefficients are measured using PFG NMR (crossed open symbols) and BDS measurements (filled symbols). The lines are fitted by the VFT (continuous) and Arrhenius (dotted) equations. The figure is reprinted with permission from Ref. 82. Copyright 2011 Royal Society of Chemistry.

Iacob *et al.* investigated the transport of an RTIL 1-butyl-3-methylimidazolium tetrafluoroborate ([BMIM][BF<sub>4</sub>]) in unidirectional nano-porous membranes (pore diameters: 7.5 ~ 10.4 nm) using broadband dielectric spectroscopy (BDS) and pulsed field gradient (PFG)-NMR,

which can determine the diffusion coefficient and the diffusion rate over more than 13 decades and to trace its temperature dependence<sup>82</sup>. The measured diffusion coefficient of the ions confined in the nano-porous membranes can be higher than that in the bulk RTILs at low temperature, as shown in Figure 1-15. In this work they attribute the increase of the observed ion diffusion in nanoconfinement to the reduction of packing density of RTILs in the pores.

There are less studies of ion transport in micropores (diameter < 2 nm), but the general expectation is that the diffusion may be slow due to the ultra-confinement. However, in a recent study it was discovered that highly viscous RTIL 1-ethyl-3-methylimidazolium chloride ([C<sub>2</sub>C<sub>1</sub>IM][Cl]) rapidly fills electrically neutral carbon nanotubes as narrow as 1.36 nm, and the ion diffusion inside the idealized nanotube is even faster than that in bulk<sup>83</sup>. As shown in Figure 1-16, the self-diffusivity of the RTILs inside CNT-10 and CNT-13 are found 4-5 times higher than that in the bulk phase, and this increase was attributed to the liquid polarity.

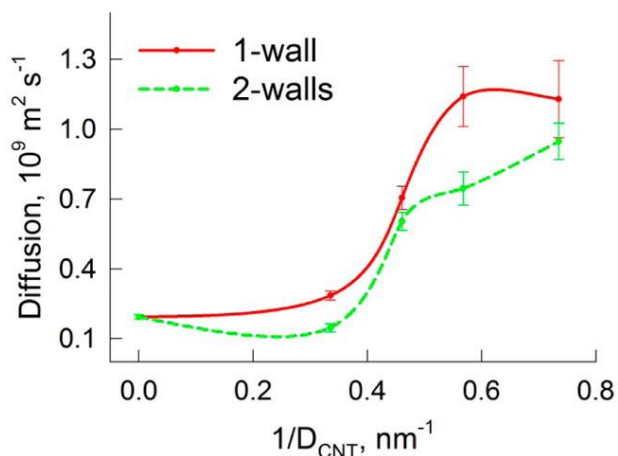


**Figure 1-16.** Diffusion of RTILs [C<sub>2</sub>C<sub>1</sub>IM][Cl] inside double-walled carbon nanotube. The filled circles correspond to systems with CNT-10, CNT-13, CNT-16, CNT-19, CNT-22, and bulk systems, and the diameters of these CNTs are 1.36, 1.76, 2.17, 2.58, 2.98 nm respectively. Figure is reprinted with permission from Ref. 83. Copyright 2014 American Chemical Society.

Recent studies of the impulsive and cyclic charging of sub-nanometer pores (diameter < 1 nm) with RTILs showed that fast charging (hence high power density) can be achieved in materials with sub-nanometer pores<sup>55-57</sup>. It was further demonstrated that the fast charging is contributed by the onset of a collective ion transport mode mediated by polarizable pore walls and fast ion diffusion during charging<sup>56-57</sup>. As shown in Figure 1-17, the self-diffusivity of ions confined in sub-nanometer pores exhibits a bell-shaped curve as charging proceeds: at the potential of zero charge, ions inside neutral sub-nanometer pores diffuse very slowly; as charging proceeds, the self-diffusion of ions greatly accelerates, even becoming a few times faster than that in bulk RTILs; their diffusion finally slows down when the pore becomes strongly charged<sup>57</sup>.

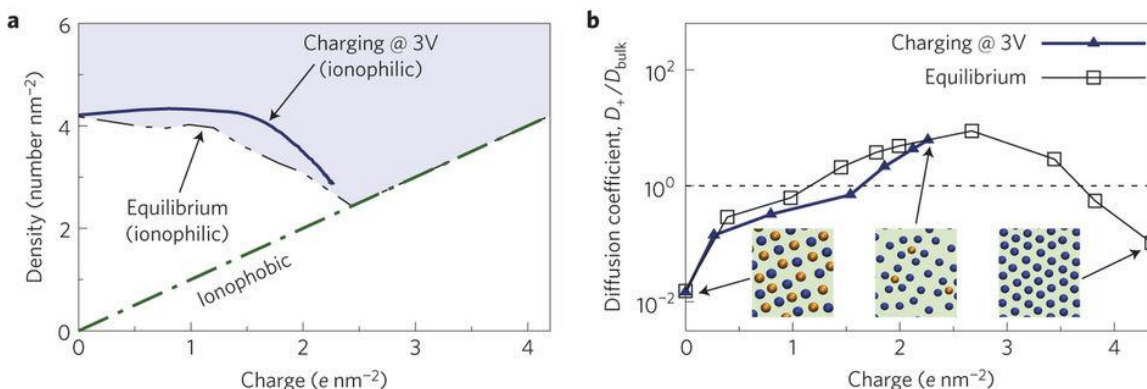


**Figure 1-17.** Self-diffusion of ions during the charging of ionophilic pores (width: 0.53 nm). (a) The average total ( $\rho_{\Sigma}$ ) and charge densities ( $q$ ) during ‘impulsive’ charging (blue solid line) and in equilibrium (black dash-double-dot line). (b) Self-diffusion coefficients of the counterions along the equilibrium path and along  $\rho_{\Sigma}(q)$  during the impulsive charging at 3 V. The diffusion coefficient is expressed in terms of the diffusion coefficient of a neutral bulk system ( $D_{\text{bulk}}$ ). Blue and orange balls in the insets denote cations and anions, respectively. Figures are reprinted with permission from Ref. 57. Copyright 2014 Springer Nature.

These results highlight the need to study ion transport under conditions similar to that found during charging of pores. The fact that fast ion dynamics was observed during charging offers hope that one can enhance the energy density of supercapacitors using RTILs and nanoporous electrodes featuring micropores while maintaining satisfactory power density. However, the fast ion

dynamics revealed in these studies was obtained using coarse-grained, nearly spherical models of RTILs, in which most atomic details of the ions are neglected. The diffusion of **real RTIL ions in micropores**, however, is affected by a host of factors including the shape of ions, occupancy of ions inside a pore, binding between specific sites on cations and anions, steric ion-wall interactions, to name just a few. Obtaining fundamental understanding of the interplay between these factors and electrode potential is a key step toward accelerating the rational design of RTILs for supercapacitors featuring micropores.

#### **1.4.2. Charging Dynamics of RTILs in Nanopores**

Most of the works reviewed in the previous section focused on the equilibrium dynamics of ions inside nanopores. While these works help understand the operation of supercapacitors, they do not directly probe the charge storage in supercapacitors under non-equilibrium conditions, i.e., dynamic charge storage. Understanding the dynamic charge storage is especially important for optimizing the performance of supercapacitors utilizing carbon nanopores and RTILs to achieve high energy densities while maintaining high charging/discharging rates<sup>15, 65</sup>. Below the experimental and computational studies of dynamic charge storage using porous carbon electrodes and RTILs are reviewed.

Experimental studies of the dynamic charge storage in supercapacitors traditionally relied on cyclic voltammetry, galvanostatic cycling, etc., which probe the macroscopic electrochemical performance. In comparison, the application of powerful techniques such as electrochemical quartz crystal microbalance (EQCM)<sup>84-85</sup>, NMR spectroscopy<sup>86</sup>, and infrared spectroelectrochemical techniques<sup>87</sup> may provide molecular information about the dynamic charge storage.

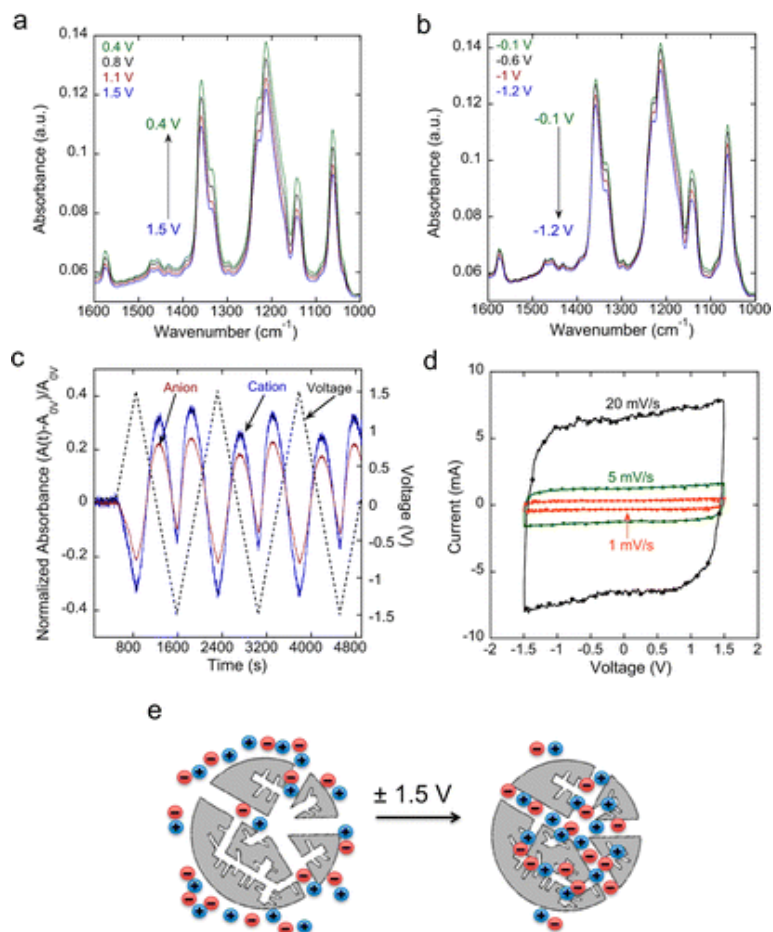


**Figure 1-18.** Dynamic charging and discharging of supercapacitor using CDC electrodes and RTILs. Cyclic voltammetry (CV) scan was from -1.5 to 1.5 V at three different scan rates. (a)(b) Time-resolved infrared spectra corresponding to positive and negative voltages respectively. (c) Normalized absorbance of the infrared bands of the cation and anion as a function of time at a scan rate of 5 mV/s (open circuit voltage: 0.068 V); (d) Corresponding CV scans at three different scan rates; (e) Sketch showing the ion dynamics within pores of CDC particles during the CV cycles. Figures are reprinted with permission from Ref. 87. Copyright 2013 American Chemical Society.

As shown in Figure 1-18, using an *in situ* infrared spectroelectrochemical technique in conjunction with cyclic voltammetry, Richey *et al.* provided direct evidence for 1-ethyl-3-methylimidazolium bis-((trifluoromethyl)sulfonyl)imide (EMIm-TFSI) ions entering and exiting carbide-derived carbon (CDC) electrode nanopores immersed during charging/discharging<sup>87</sup>. They further tested the RTILs with nonporous onion-like carbons (OLC) and showed that the OLC

electrode allows fast charging and discharging by storing the ions on the surface, resulting a small change in concentration in the electrodes. At last, they also showed when a mixture of RTILs and organic solvent were used as the electrolytes, both the organic solvent and RTILs enter and exit the CDC pores during charging/discharging.

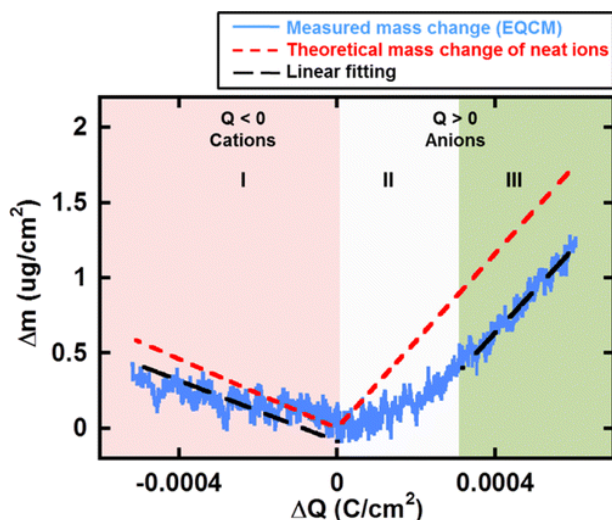


**Figure 1-19.** Electrode mass change vs charge during the polarization of electrodes. Average pore size of the CDC electrodes is 1 nm. Electrolyte is neat EMI-TFSI. The blue solid line is the measured mass change using EQCM, the red dashed line is the theoretical mass change of neat ions calculated from Faraday’s law, the black dashed line is the linear fitting of measured mass change. Figures are reprinted with permission from Ref. 88. Copyright 2014 American Chemical Society.

Using EQCM, Tsai *et al.* tested neat EMI-TFSI and acetonitrile-solvated EMI-TFSI electrolyte in CDC with two different average pore sizes (1 and 0.65 nm) under cyclic voltammetry<sup>88</sup>. Figure 1-19 shows the change of the electrode mass vs. the charge passed in the electrode during the cyclic voltammetry and its comparison with theoretical mass change of neat ions, for the CDC-1 nm in neat EMI-TFSI. In domain I, charging of the porous electrode occurs through the adsorption of counterions ( $\text{EMI}^+$ ) and no co-ion ( $\text{TFSI}^-$ ) seems to be involved, indicating that at high polarization, counterions dominate the charge storage in CDC electrodes. Furthermore, they also showed that both neat and solvated ions have more difficulty in accessing

the 0.65 nm-pores than the 1 nm-pores. For solvated EMI-TFSI in acetonitrile, the solvation numbers of cations in the 1 nm- and 0.65 nm-pore were estimated to be 3–4 and 1–2, respectively.

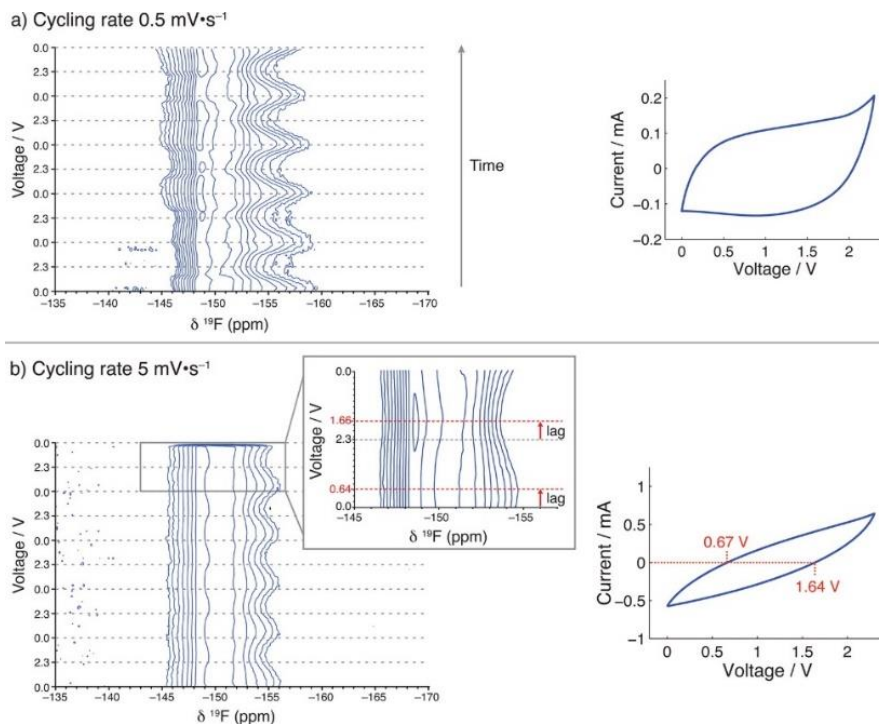


**Figure 1-20.** NMR spectra of electrodes during cyclic voltammetric cycling. The figures show only the negative electrodes of the supercapacitor cell. Contour plot of the spectra (left) and cyclic (right) voltammograms are shown. The NMR spectra are measured at two cycling rates: (a)  $0.5 \text{ mV}\cdot\text{s}^{-1}$  and (b)  $5 \text{ mV}\cdot\text{s}^{-1}$ . Figures are reprinted with permission from Ref. 86. Copyright 2013 American Chemical Society.

Wang *et al.* investigated the charge storage mechanism of supercapacitors using in-situ NMR spectroscopy<sup>86</sup>. Specifically, they studied the changes at the electrode-electrolyte interface during charging and discharging. Figure 1-20 shows the real-time in-situ NMR spectra during cyclic voltammetric cycling at two cycling rates. At the lower rate, the variation of the strongly adsorbed chemical shift is well synchronized with the applied voltage, and the cyclic voltammogram is nearly rectangular. At a higher cycling speed, the variation of the strongly adsorbed chemical shift is no longer synchronized with the voltage change, and the cyclic voltammogram shows a nonrectangular shape. They further confirmed that the changes in the

resonance frequency are directly related to the amount of charge stored in the electrode, but not the potential difference applied on to the cell.

These studies provided unprecedented details on the dynamic charge storage in supercapacitors at the electrode level, i.e., an ensemble average of all pores inside the electrodes. However, the charging dynamics in individual nanopores, especially the underlying ion dynamics along the pore length, was not resolved in these experimental works. These limitations, along with the fact that some of the intriguing phenomena revealed in these studies are yet to be fully rationalized (e.g., the predominance of counterions in charge storage inside narrow pores), highlight that significant gaps still remain in the understanding of the dynamic charge storage in nanopores filled with RTILs. Filling such a gap is essential for the rational design of nanoporous electrodes and RTIL electrolytes for optimal dynamic charge storage. Computer simulations, especially those at the single-pore level, may lend critical insight in filling this knowledge gap by spatially and temporally resolving the dynamic charge storage. At present, only a limited number of computer simulations of the charging dynamics in subnanometer pores exist.

Based on a mean-field phenomenological model, Kondrat *et al.* performed the first simulations on the charging dynamics of nanosized porous electrodes<sup>89</sup>. Figure 1-21 shows the charging of a nanopore under an impulsively imposed voltage. The pore is initially filled (ionophilic) in (a) and empty (ionophobic) in (b). The charging process for the initially empty pores finishes faster than the initially filled pores. Furthermore, their work also suggested that charging of empty pores proceeds in a front-like manner, the accumulated charge grows as a square root of time for both types of pores, and the charging of a pore initially filled with RTILs is a diffusive process.

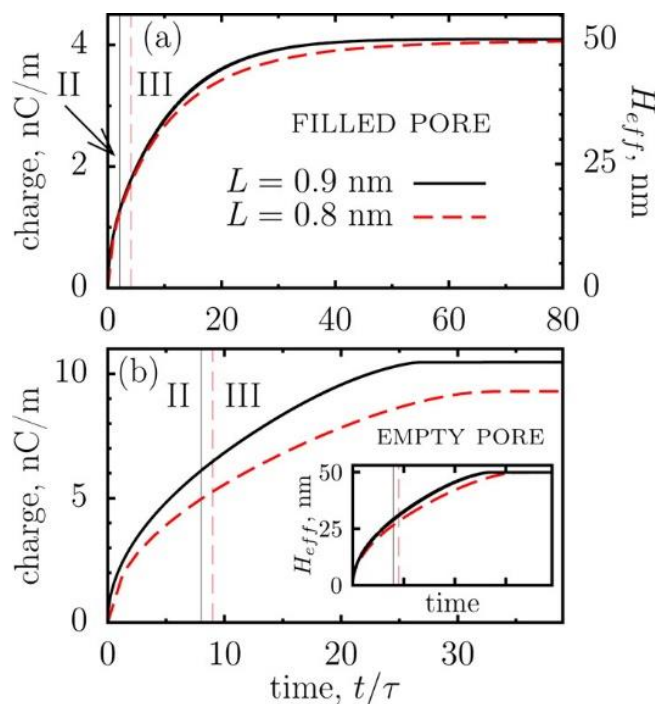


**Figure 1-21.** Charging of two types of pores under the action of an impulsively imposed voltage. (a) Pore is initially filled. (b) Pore is initially empty. The thin vertical lines indicate the beginning of the final charging stage. The empty pore reaches the final charging state faster. The right axis in (a) and the inset in (b) show the effective charging depth  $H_{eff}$  as defined by  $H_{eff} = q_0^{-1}Q(t) = q_0^{-1} \int_0^\infty ec(x, t)dx$ , where  $c$  is the volumetric charge density,  $q_0$  is the final charge density, and  $e$  is the elementary charge. The total pore length is  $H = 50$  nm. Figures are reprinted with permission from Ref. 89. Copyright 2013 American Chemical Society.

Later Kondrat et al. used MD simulations<sup>57</sup> to verify the diffusive nature of the charging of ionophilic pores. Figure 1-22 shows charging of ionophilic pores obtained from MD simulations. The evolution of the net charge inside the pore exhibits the square-root and exponential saturation regimes revealed by the mean field theory model. Although the diffusive nature of charging revealed by these simulations is in apparent agreement with the transmission line model (TLM), the physics underlying the time constant of charging differ fundamentally from that in the TLM<sup>57</sup>. In this work they also calculated the ion self-diffusion during charging of ionophilic pores. These MD simulations using simplistic models for ions and pores indicated that the charging of

subnanometer pores is fast - the ion diffusion inside a pore during charging can be very fast despite geometrical confinement and the collective transport of ions due to electrical migration greatly accelerates charging.

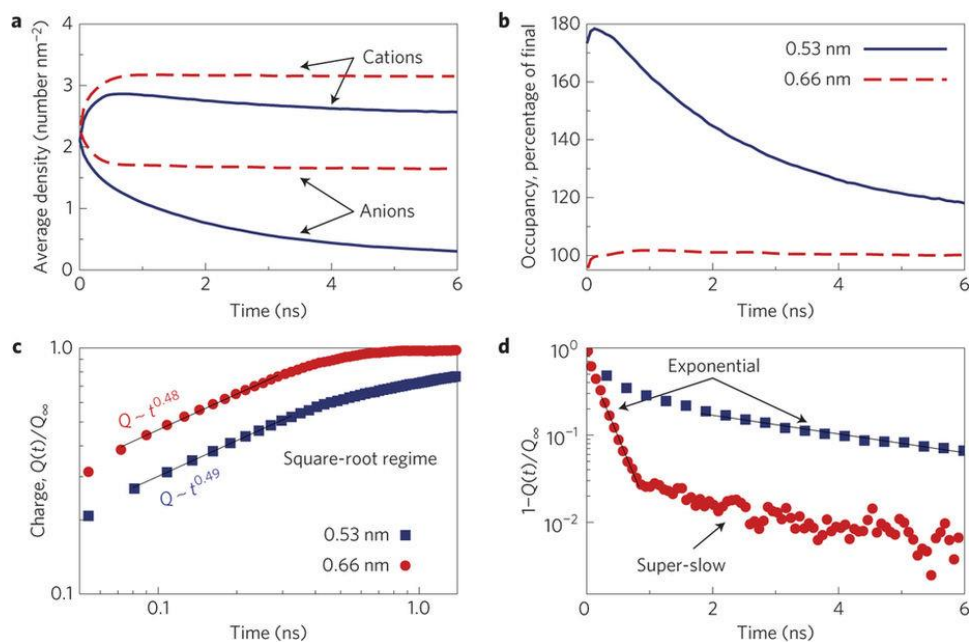


**Figure 1-22.** Charging of ionophilic pores. The pore was charged imposing a 3 V potential difference between the negative and positive electrodes at  $t=0$ . (a) The average cation and anion densities inside the pore as a function of time. (b) The total pore occupancy as a function of time. The evolution of the net charge inside the pores exhibits a diffusive behavior: the initial stage of charging follows a square-root law (c); The late stage of charging follows an exponential saturation law (d). Figures are reprinted with permission from Ref. 57. Copyright 2014 Springer Nature.

Both the diffusive nature and fast rate of charging subnanometer pores revealed above are in line with findings from another MD simulations of the charging of porous electrodes with realistic pore structures<sup>55</sup>. In this work, Péan *et al.* used MD simulations to study the charging of nanoporous CDC electrodes with 1-butyl-3-methylimidazolium hexafluorophosphate (BMI-PF<sub>6</sub>). As shown in Figure 1-23, the variation of the total charge of the electrodes as a function of time are well described by the equation corresponding to an RC circuit representation of the MD system, which shows a diffusive charging process.

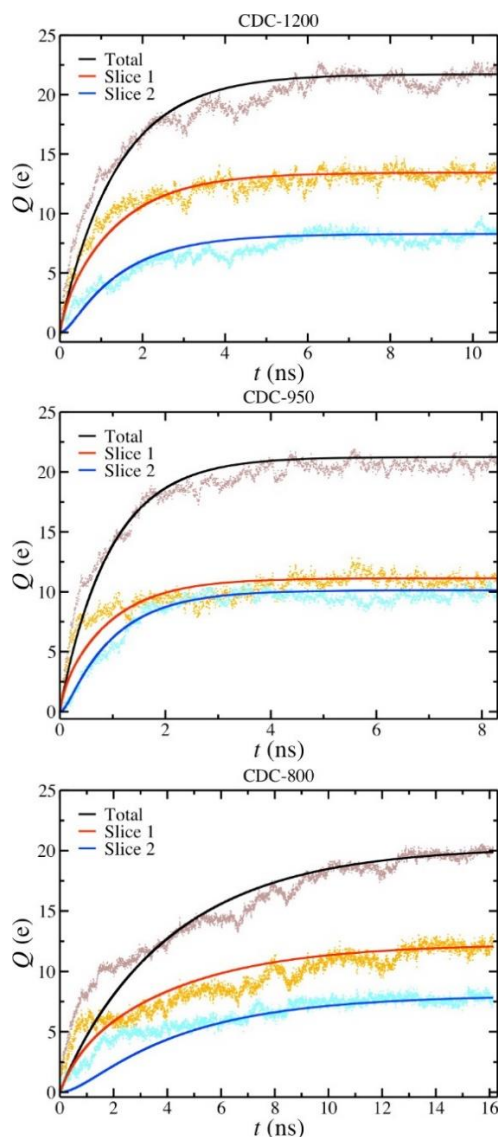


**Figure 1-23.** Total charge of the electrodes as a function of time for three systems. MD simulation results (dotted curves) are well described by the RC circuit (solid lines,  $Q(t) = Q_{max}[1 - A_1 \exp(-\frac{t}{\tau_1}) - A_2 \exp(-\frac{t}{\tau_2})]$ , where  $Q_{max}, A_1, A_2, \tau_1$  and  $\tau_2$  are given as function of electric circuit components). Figures are reprinted with permission from Ref. 55. Copyright 2014 American Chemical Society.

These works suggest that nanoporous electrodes and RTILs can potentially lead to high energy density supercapacitors capable of operating at high charging/discharging rates. Most of these simulations, however, did not study the *discharging* of nanopores, which is not a simple reversal of the charging process and is critical for understanding the energy efficiency of dynamic

charge storage. Furthermore, except for one of the most recent works<sup>90</sup>, all previous studies dealt with the charging of nanopores by impulsively imposed voltages, while nanopores are typically subject to *cyclic charging/discharging* during characterization and in practical operation of supercapacitors.

### 1.4.3. RTILs in Ion Gels

In this section, recent research progress on PBDT ion gels<sup>49</sup> is reviewed. In their first work on the liquid crystalline (LC) ion gels, Ying *et al.* investigated the structure of the ion gel using scanning electron microscope (SEM), polarized microscopy (POM), and X-ray diffraction. The morphological alignment and semi-crystalline structure of the LC ion gels are studied systematically. Figure 1-24a shows the SEM image of the 21% PBDT IL gel (the mass fraction of PBDT is ~21% in the dried gel), and a micrometer-scale fibrillary structure are oriented parallel to the magnetic (B-) field. Figure 1-24b shows smooth modulation in light transmission as a function of  $\phi$  angle between the alignment axis of 21% PBDT IL gel and the plane polarization of incident light. Adjacent minima and maxima are separated by  $45^\circ$ , with a sinusoidal periodicity of  $90^\circ$ . Figure 1-24c-e shows the X-ray diffraction patterns for 5%, 15%, and 21% PBDT IL gel. The gray amorphous halo at  $2\theta = 12^\circ\text{--}24^\circ$  scattering angle are assigned to the amorphous RTILs. The difference pattern shown in Figure 1-24f represents the predominantly diffraction of aligned PBDT chains in the 21% PBDT IL gel. The main diffraction peaks, labeled by A, B, C and D, are assigned to the different characteristic lengths labeled in Figure 1-24g, respectively. At last, the “X” pattern in Figure 1-24f is similar to those observed in the diffraction pattern of DNA<sup>91-92</sup> and other double helix fibers<sup>93</sup>, indicating a helical dimer conformation of the PBDT chains. These molecular and mesoscale structures of the ion gels revealed experimentally form a good foundation for the future

computational simulation of these materials to understand the mechanisms behind their unusual properties, such as high conductivity and strong mechanical modulus.

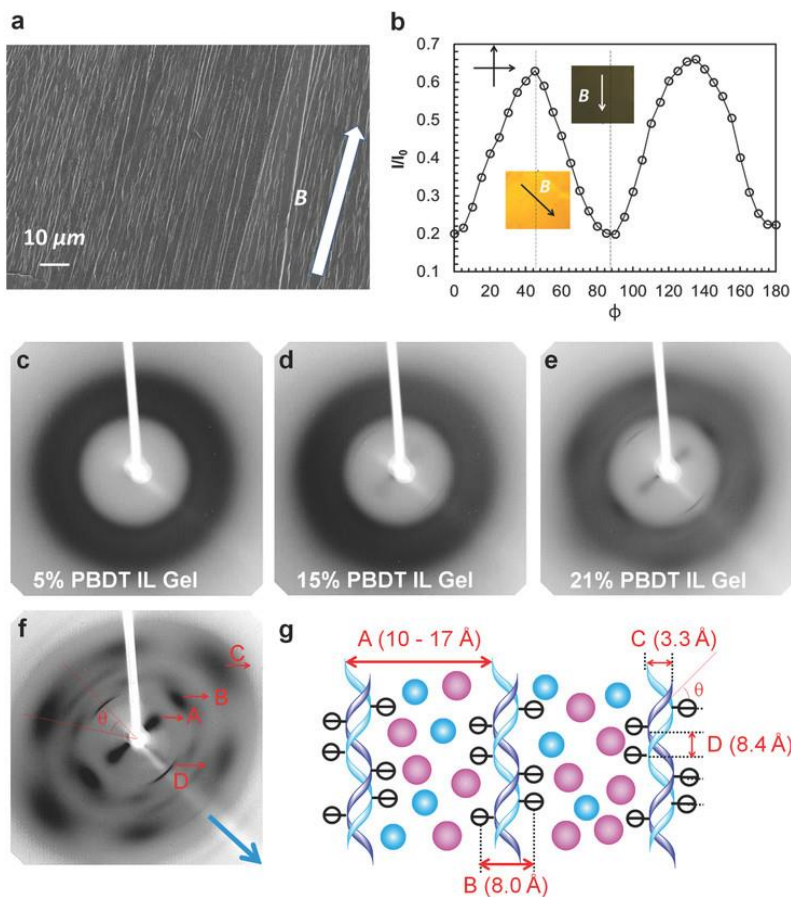


**Figure 1-24.** Morphological alignment and structure of the PBDT ion gels. (a) SEM image of nitrogen freeze-fractured side-on surface. The PBDT mass fraction is 21% in the dried gel. (b) Transmitted light intensity of aligned gel sample under crossed polarizers as a function of the angle  $\phi$  between the sample alignment and the analyzer. (c–e) X-ray diffraction patterns for gels with PBDT mass fraction of 5%, 15%, and 21%, respectively. (f) Difference image of (c) and (e) to remove the amorphous halo due to RTIL scattering. The blue arrow indicates the mounting direction of the sample fiber and gel alignment axis. (g) A diagram of the molecular structure of gel based on the scattering parameters. Figures are reprinted with permission from Ref. 49. Copyright 2016 John Wiley and Sons.

In a follow-up study, Zhou *et al.* investigated the structure and dynamics of the RTILs  $[\text{C}_2\text{mim}][\text{TfO}]$  in PBDT IL gels us MD simulations<sup>94</sup>. In these simulations, the PBDT polyanions are semi-coarse grained as rigid rods decorated with sulfonate groups. The dimensions of the

model are derived from the structure information observed in X-ray diffraction data<sup>49</sup>. The RTILs are all resolved at molecular level. Figure 1-25 shows the ion charge density and overscreening near the PBDT rods. The cations and anions are observed to form alternating layers around the polyanion nanorods and charge on the rod is overscreened by the ionic layer surrounding it. This ordering of ions indicates the formation of long-range electrostatic networks that may help provide the mechanical cohesion in this gel. Figure 1-26 shows the diffusion of the RTILs in the PBDT ion gel with different PBDT mass fractions. The RTIL dynamics predicted in these simulations qualitatively agree with the experimental values, but some important differences exist. This is possibly due to the coarse-grain rods and the lack of precise structure of the gel. Slower dynamics of the ions compared with that in the bulk phase are observed, but they are still faster than the diffusion of Li<sup>+</sup> ions in most solid polymer electrolytes.

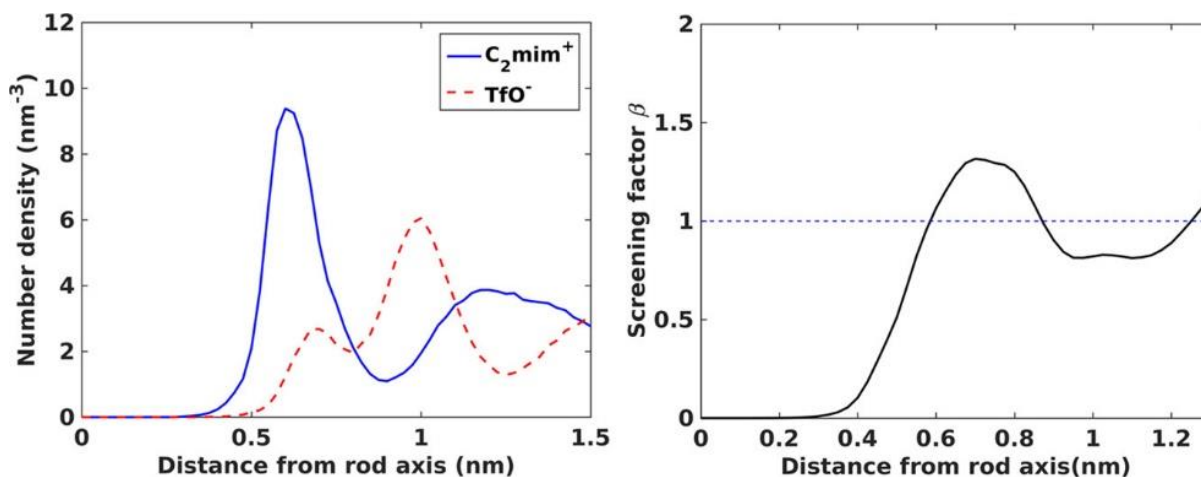


**Figure 1-25.** Structure of the RTIL and charge overscreening near the PBDT rod in an ion gel. Ion density (a) and screening factor  $\beta$  (b) as a function of the radial distance from the PBDT rod axis. The positions of the  $C_2mim^+$  and  $TfO^-$  ions are based on the center atom of the molecule. The nominal rod spacing is 2.2 nm.  $\beta(r) = -\frac{1}{q_L} \int_0^r 2\pi r \rho_e(s) ds$  is the defined screening factor, where  $\rho_e(s)$  is the space charge density due to ions at a radial distance  $s$  and  $q_L$  is the charge on the PBDT rod per unit length (-2.38 e/nm). Figures are reprinted with permission from Ref. 94. Copyright 2017 American Chemical Society.

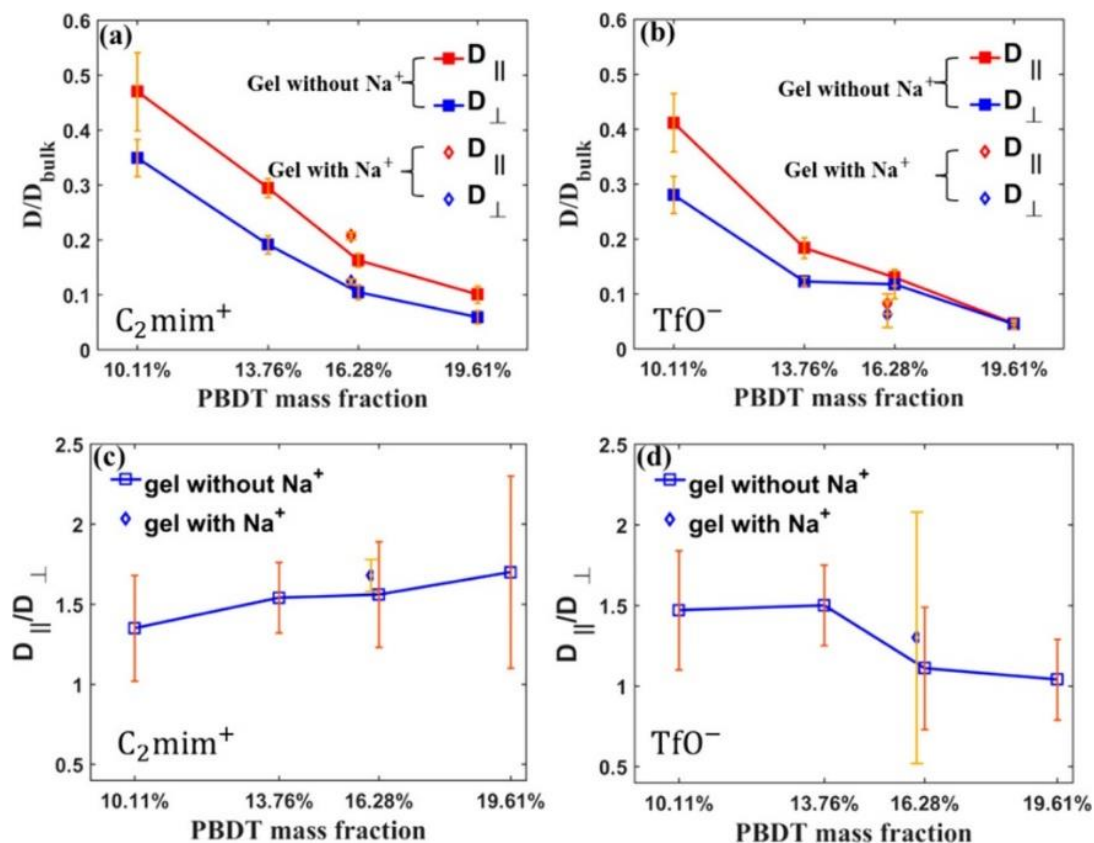


**Figure 1-26.** Diffusion coefficients of the ions in the PBDT ion gel. (a, c) Diffusion coefficients of  $\text{C}_2\text{mim}^+$ . (b, d) Diffusion coefficients of the  $\text{TfO}^-$  ions. The diffusion coefficients were measured with systems corresponding to different PBDT mass fractions and residual  $\text{Na}^+$  ions. The bulk diffusion coefficients of the  $\text{C}_2\text{mim}^+$  and  $\text{TfO}^-$  ions are  $22.0 \times 10^{-11}$  and  $12.1 \times 10^{-11}$   $\text{m}^2/\text{s}$  respectively. Figures are reprinted with permission from Ref. 94. Copyright 2017 American Chemical Society.

Most recently, Zhou *et al.* investigated the interactions between nanorods immersed in RTILs using MD simulations<sup>95</sup>. In these simulations, the nanorods are also modeled as semi-coarse grained carbon rods. The rods are fully aligned and swollen by RTILs, which is similar to the situation of polyanions in the PBDT ion gels. As shown in Figure 1-27, they found that, when the rods are charged, the force between the rods is oscillatory as the distance between them changes, and there is an energy barrier of  $\sim 5 k_B T/\text{nm}$  to separate rods that are initially positioned at the primary energy minimum. Such a barrier can stabilize the nanorods in RTILs and this may contribute to the mechanical strength of the PBDT ion gels. They further correlate the energy

change with the interference of ionic space charge around different rods, i.e. a constructive (destructive) interference leads to peak (valley) in the interaction energy vs. rod-rod separation curve, and the interference of the ionic space charge near nanorods can be predicted by a simple superposition of ion charge density near one rod.

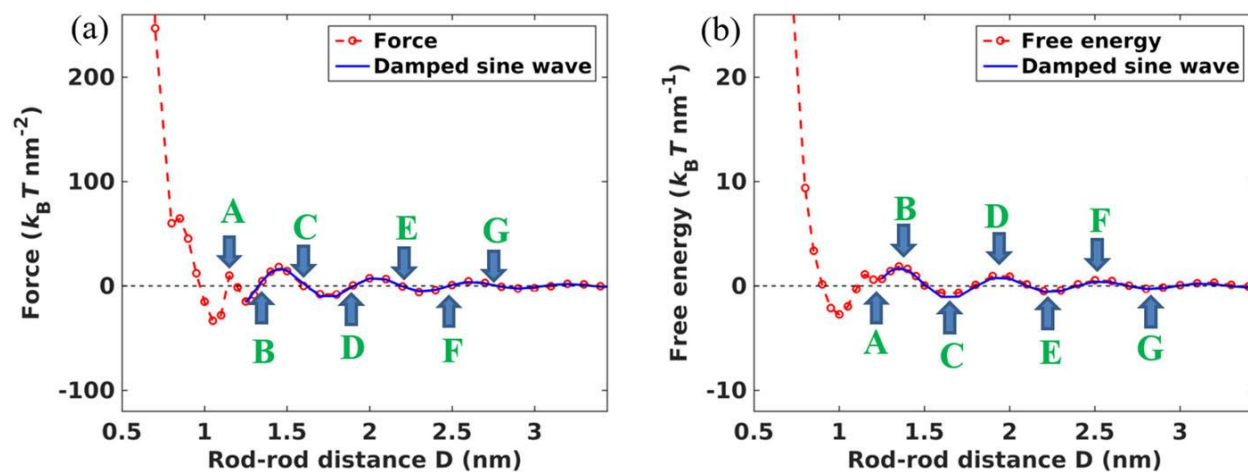


**Figure 1-27.** Interactions between two charged nanorods immersed in RTILs. (a) Interaction force. (b) Interaction energy. Figures are reprinted with permission from Ref. 95. Copyright 2017 AIP Publishing LLC.

These work laid a foundation of understanding the properties of the PBDT ion gels. However, to enable the rational design of these materials, many fundamental questions must be answered. In particular, the tensile modulus of PBDT ion gels can reach hundreds of MPa to a few GPa. This modulus is much higher than most reported ion gels<sup>96-97</sup> and is desired in numerous electrochemical devices. Is this strong modulus the result of the rod-rod interaction in the RTILs? In PBDT ion gels it was found that the polyanions may form a hexagonal phase<sup>98</sup>, thus the distribution of polyanions in ion gels can be more complicated than that investigated by Zhou *et al.*<sup>95</sup>. In these situations, how do the nanorod interactions affect the mechanical strength of the gel? Specifically, how did the nanorods interact with each other and the RTILs confined between them? When the rods are modeled as fully resolved PBDT polyanions in a hexagonal phase, can the

nanorods interaction still be predicted by the charge interference, and can the charge interference be predicted by the simple superposition of charge density? Answering these questions will help to shape and guide the development of this new class of ion gels.

## 1.5. The Scope of This Dissertation

This dissertation focuses on the application of RTILs as working electrolytes in supercapacitors and as components of ion-gel electrolytes. For the application of RTILs in supercapacitors, the review of prior works in this area suggests that a fundamental understanding of the self-diffusion of real RTIL ions confined in micropores and the *dynamic* charge storage in nanopore filled with RTILs under cyclic charging/discharging conditions is essential for the rational design of RTILs and porous electrodes of supercapacitors. In view of this need, the following research will be performed:

- (1) The diffusion of EMIM<sup>+</sup> and TFSI<sup>-</sup> ions inside slit-shaped micropores is studied using MD simulations. The unique aspect of this study is that the ion densities inside the pores are taken from those during quasi-static charging process and ions are resolved with full atomistic details. The evolution of the self-diffusion coefficients of EMIM<sup>+</sup> and TFSI<sup>-</sup> ions during the quasi-static charging of pores are mapped out. Pores with center-to-center widths corresponding to single to two layers of ions inside the pores are considered.
- (2) The cyclic voltammetry of subnanometer pores connected with RTIL reservoirs is investigated, which have so far only been studied experimentally but not using molecular simulations. By dissecting the cyclic voltammetry with molecular resolution, the study clarifies the essential features of the dynamic charge storage in nanopores, its underlying

ion dynamics, and how its macroscopic characteristics such as energy density and charge storage efficiency are affected by pore size and voltage scan rates.

For the application of RTILs in the novel PBDT ion gels, current experimental data already suggests that they are promising candidates for numerous electrochemical devices. To enable the rational design of these ion gels, a fundamental understanding of the origins of their superior mechanical strength and transport properties is needed. In particular, understandings of the structure of RTILs confined between polyanions, how this structure affects the interactions between polyanions and ultimately the mechanical properties of the ion gel are needed. In view of these needs, the following research will be performed:

(3) The mechanical property of the novel PBDT ion gels is investigated using MD simulations.

Both RTILs and PBDT polyanions are resolved with molecular details. The elastic modulus of the gel is calculated from the MD simulations and compared to the experimental data. The mechanisms behind the computed elastic modulus, i.e. how the modulus is related to structure of the RTILs in the ion gel, is discussed.

The rest of the dissertation is organized as follows. Chapter 2 and 3 present the studies on diffusion of RTILs in slit micropores and the dynamic charge storage in nanopores, respectively. Chapter 4 presents the molecular simulations of the PBDT ion gels aiming to understand its strong mechanical modulus. Finally, conclusions are presented in Chapter 5.

## CHAPTER 2

### Dynamics of Ions in Nanopores under Charging Relevant

#### Conditions\*

There is an emerging concern that using room-temperature ionic liquids (RTILs) together with microporous electrodes may compromise supercapacitors' power density in spite of their benefit for enhancing energy density due to possibly slow transport of ions inside narrow pores. Based on molecular simulations of the diffusion of EMIM<sup>+</sup> and TFSI<sup>-</sup> ions in slit-shaped micropores (width < 2 nm) under conditions similar to those during pore charging, it is shown that, in pores that accommodate only a single layer of ions, the ions diffuse increasingly faster as the pore becomes charged, even faster than Na<sup>+</sup> ions in bulk water. This trend is only reversed when the pore becomes very highly charged. In pores wide enough to fit more than one layer of ions, the ion diffusion is typically slower than in the bulk, and only changes modestly as the pore becomes charged. Analysis of these results revealed that the fast (or slow) diffusion of ions inside a micropore is correlated most strongly with the dense (or loose) ion packing inside the pore during charging. The molecular details of ions and the precise width of pores modify these trends relatively weakly, except when the pore size is so narrow that the conformation of ions is strongly

---

\* This chapter is adapted with permission from the following paper (Ref. 99):

He, Y.; Qiao, R.; Vatamanu, J.; Borodin, O.; Bedrov, D.; Huang, J.; Sumpter, B. G., Importance of Ion Packing on the Dynamics of Ionic Liquids During Micropore Charging. *The Journal of Physical Chemistry Letters* **2016**, *7*, 36-42.

Copyright 2016 American Chemical Society.

constrained by the pore walls. Insight from these results should be useful for establishing guidelines for the design of RTILs and electrode materials for supercapacitors.

## 2.1. MD Systems and Methods

The simulation system consisted of a slab of EMIM<sup>+</sup> and TFSI<sup>-</sup> ions enclosed between two graphene layers. Three pores with width of 0.72, 0.75, and 1.1 nm were studied. The pore walls measure approximately 6×6 nm<sup>2</sup> laterally in all simulations, and periodic boundary conditions were applied in the lateral directions. Inside each pore, for a given net ionic charge, the number of EMIM<sup>+</sup> and TFSI<sup>-</sup> ions is taken to be the same as that computed in Ref. 70, which studied the charge storage with the ions considered here in the pores of the same width. The number densities of cations/anions/charge/total ion density are reproduced in Table 2-1 to Table 2-3.

**Table 2-1.** Number density of ILs inside 0.75 nm pore.

Potential Difference (V)	$\rho_{EMIM^+}$ (#/nm <sup>2</sup> ) <sup>a</sup>	$\rho_{TFSI^-}$ (#/nm <sup>2</sup> ) <sup>a</sup>	$q$ (e/nm <sup>2</sup> ) <sup>b</sup>	$\rho_{\Sigma}$ (#/nm <sup>2</sup> ) <sup>c</sup>
8.0	0.0	2.23	-2.23	2.23
6.0	0.0	2.07	-2.07	2.07
5.0	0.0	1.95	-1.95	1.95
3.0	0.40	1.63	-1.23	2.03
2.4	0.53	1.50	-0.97	2.03
1.5	0.80	1.23	-0.43	2.03
0	1.017	1.017	0	2.03
1.0	1.20	0.83	0.37	2.03
2.0	1.25	0.41	0.84	1.66
2.4	1.25	0.27	0.99	1.52
3.0	1.303	0.062	1.24	1.37

<sup>a</sup> area number density. <sup>b</sup>  $q = \rho_+ - \rho_-$ . <sup>c</sup>  $\rho_{\Sigma} = \rho_+ + \rho_-$ .

**Table 2-2.** Number density of ILs inside 0.72 nm pore.

Potential Difference (V)	$\rho_{EMIM^+}$ ( $\#/nm^2$ ) <sup>a</sup>	$\rho_{TFSI^-}$ ( $\#/nm^2$ ) <sup>a</sup>	$q$ ( $e/nm^2$ ) <sup>b</sup>	$\rho_{\Sigma}$ ( $\#/nm^2$ ) <sup>c</sup>
2.5	0.534	1.335	-0.8	1.87
1.75	0.590	1.20	-0.62	1.79
0	0.544	0.544	0	1.09
1.0	0.770	0.10	0.67	0.87
2.5	1.090	0	1.09	1.09

<sup>a</sup> area number density. <sup>b</sup>  $q = \rho_+ - \rho_-$ . <sup>c</sup>  $\rho_{\Sigma} = \rho_+ + \rho_-$ .

**Table 2-3.** Number density of ILs inside 1.1 nm pore.

Potential Difference (V)	$\rho_{EMIM^+}$ ( $\#/nm^2$ ) <sup>a</sup>	$\rho_{TFSI^-}$ ( $\#/nm^2$ ) <sup>a</sup>	$q$ ( $e/nm^2$ ) <sup>b</sup>	$\rho_{\Sigma}$ ( $\#/nm^2$ ) <sup>c</sup>
3.0	1.232	2.023	-0.8	3.26
1.5	1.42	1.88	-0.46	3.30
1.0	1.49	1.80	-0.31	3.29
0	1.725	1.725	0	3.45
1.0	1.94	1.62	0.32	3.56
1.5	2.04	1.58	0.46	3.62
3.0	2.24	1.44	0.8	3.68

<sup>a</sup> area number density. <sup>b</sup>  $q = \rho_+ - \rho_-$ . <sup>c</sup>  $\rho_{\Sigma} = \rho_+ + \rho_-$ .

The explicit atom (EA)/united atom (UA) models of EMIM<sup>+</sup> and TFSI<sup>-</sup> ions developed by Vatamanu *et al.*<sup>100</sup> were adopted for these ions. The carbon atoms in the graphene wall were modeled using the same force fields as in Ref. 70. The non-electrostatic, non-bonded interactions in these force fields are a combination of Lennard-Jones (LJ) and Buckingham potential, and the modified Waldman-Hagler combination rules<sup>101</sup> were used to compute the LJ and Buckingham potential parameters for the interaction between two different types of atoms.

Molecular dynamics simulations were performed using the LAMMPS code in the NVT ensemble<sup>102</sup>. The temperature of the ions was maintained at 393 K using a Nosé-Hoover thermostat. The non-electrostatic interactions were computed via direct summation with a cut-off length of 1.0 nm. The electrical potential on all wall atoms are enforced to be the same, using the LAMMPS

subroutine developed in Ref. <sup>103</sup>. Such a subroutine computes the electrical charge on the wall atoms at each time step, and thereafter the electrostatic interactions within the system were computed using the P3M (particle-particle particle-mesh) method<sup>104</sup>. The wall atoms were fixed during the simulation. Trial simulations were also performed in which the wall atoms were allowed to move and their temperature was maintained at 393 K. In those simulations, the intermolecular interactions between graphene wall's carbon atoms were modeled using the force fields developed by Wei *et al.*<sup>105</sup> The electrostatic ion-ion interactions were computed based on the electrostatic potential given by<sup>69</sup>

$$\phi(z, R; z_1) = \frac{4}{\epsilon_0 \epsilon_r W} \sum_{n=1}^{\infty} \sin\left(\frac{\pi n z_1}{W}\right) \sin\left(\frac{\pi n z}{W}\right) K_0\left(\frac{\pi n R}{W}\right) \quad (2-1)$$

where  $\epsilon_0$  is the vacuum permittivity,  $\epsilon_r$  is the dielectric constant of the medium in the slit pore,  $R$  is the lateral distance between charges,  $W$  is the pore width, and  $K_0(x)$  is the modified Bessel

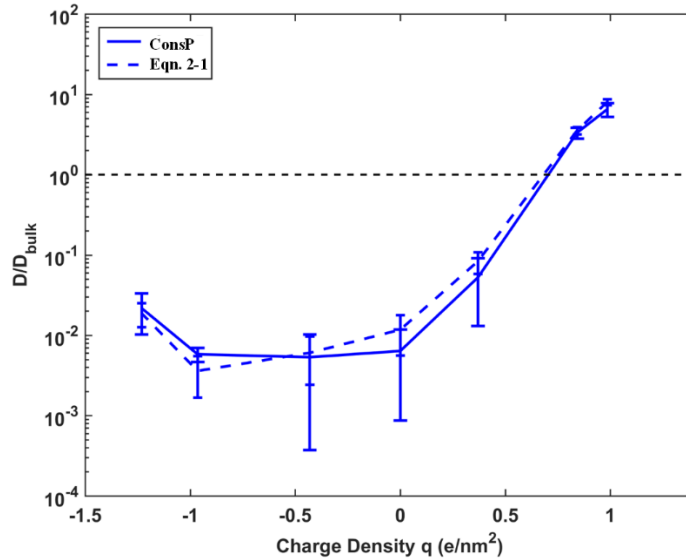


**Figure 2-1.** Diffusion coefficient of the EMIM<sup>+</sup> ions using two methods. The ions were confined inside a 0.75 nm slit pore at different levels of charging. The solid line is computed using the constant potential code in which carbon atoms were fixed. The dashed line is computed using Equation 2-1 for ion-ion electrostatic interactions and carbon atoms were allowed to vibrate.

function of the second kind of order zero. With such an electrostatic potential, the screening of the electrostatic ion-ion interactions by the polarizable pore walls is explicitly considered. While these simulations are significantly more expensive than those described above, it was found that the ion diffusion coefficients obtained in these simulations were very similar to those obtained when the graphene atoms were fixed (see Figure 2-1). Hence, all results reported in this work are based on the fixed graphene wall simulations.

To generate the initial configuration of the simulation system, the desired number of ions were first packed between the pore walls using the PACKMOL code<sup>106</sup>. After energy minimization, the system is then equilibrated for 10 ns, followed by a production run of 40 ns. A 1 fs time step was used and the trajectories of the ions were saved every 1ps. The diffusion coefficients of ions were then computed using the Einstein-Helfand method<sup>107</sup>. Specifically, the mean-square displacement (MSD) of each ion in the *xy*-plane as a function of time was first calculated. The MSD is computed for a time *T* up to 150 ps (when ion diffusion is fast) or 500 ps (when ion diffusion is slow). Such a time is long enough that the MSD increases linearly with time (see Figure 2-2). Next, the MSD is fitted to a linear curve in the time window of 0.6-1.0*T*, and the lateral ion diffusion coefficient is computed as 1/4 of the slope of the fitted linear curve. The latter is consistent with the formula

$$D = \lim_{t \rightarrow \infty} (r(t) - r(0))^2 / 4t \quad (2-2)$$

where  $(r(t) - r(0))^2$  is the ion's mean square displacement in the *xy*-plane. Sample MSDs for the TFSI ions confined in the 0.75 nm pore under various charging conditions are shown in Figure 2-2.

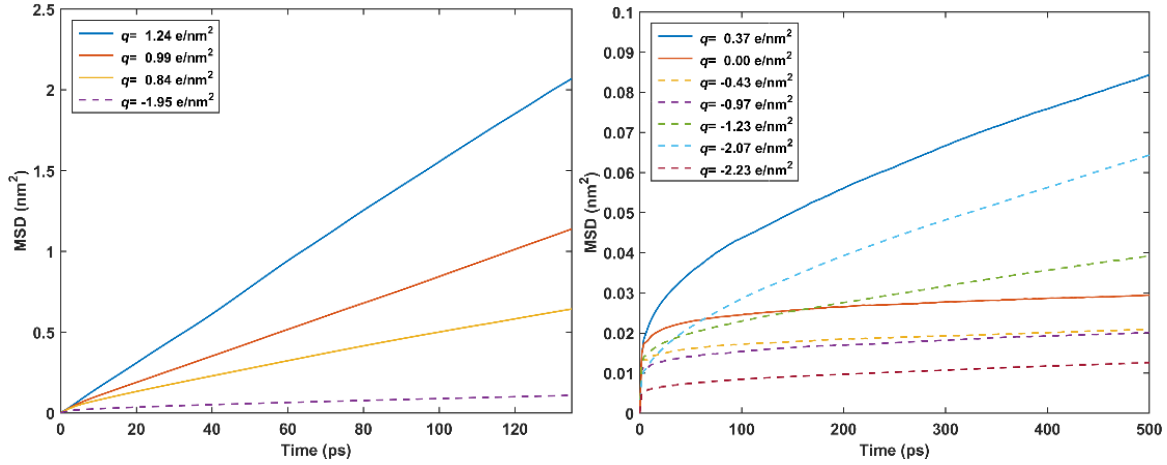


**Figure 2-2.** MSDs of the TFSI ions confined inside 0.75 nm pores (fast). Each curve represents a charging state corresponding to the respective charge density in the pore.

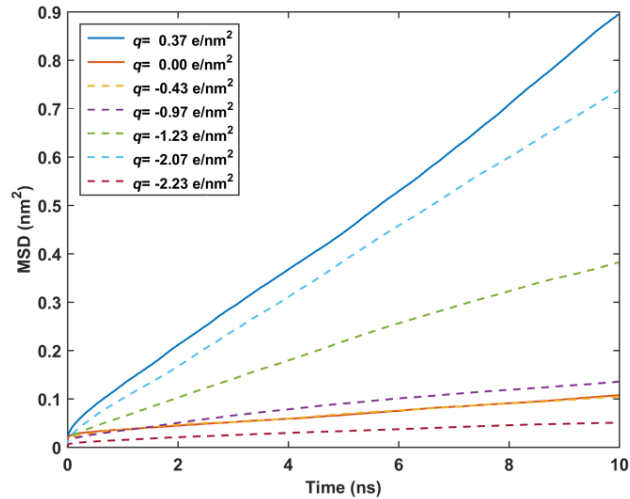


**Figure 2-3.** MSDs of the TFSI ions confined inside 0.75 nm pores (slow). In these charging states the TFSI ions diffuse very slowly. The time window for this MSD computation is increased from 0-500 ps in Figure 2-2 to 0-10 ns.

As a comparison, the MSD was also computed in a time window of  $T = 10$  ns for cases in which ions diffuse slowly to assess the diffusion at large time scale in Figure 2-3. These MSDs exhibit the same trend as revealed by the MSDs in the time window of  $T = 500$  ps, and the diffusion coefficients extracted from these MSDs agree with those extracted from the MSDs in the time window of 500 ps within statistical error (see Figure 2-4).

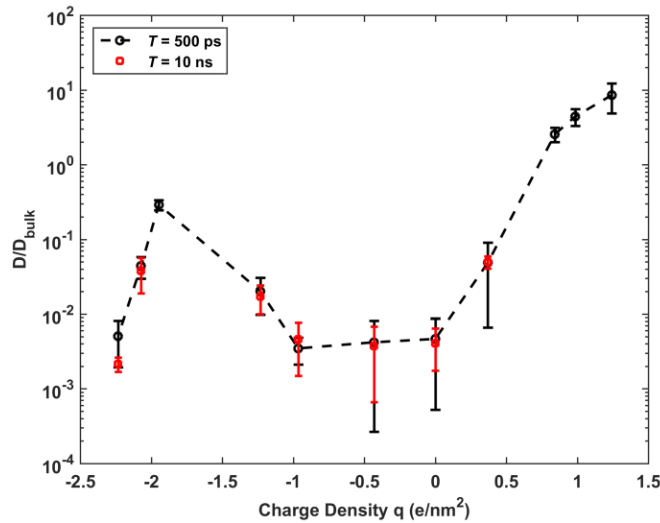


**Figure 2-4.** Diffusion coefficients of TFSI<sup>-</sup> ions using two sets of MSDs. Ions were confined inside 0.75 nm pores. The first set of MSD (see Figure 2-2) was computed in a time window of  $T_1 = 150$  ps (for fast ion diffusion) or 500 ps (for slow ion diffusion), and the diffusion coefficient was computed by linear regression of the MSD between  $0.6-1.0T_1$ . The second set of MSD (see Figure 2-3) was computed in a time window of  $T_2 = 10$  ns, and the diffusion coefficient was computed by linear regression of the MSD between  $0.6-1.0T_2$ . Note that the second set of MSD ( $T = 10$  ns) was computed only for the charging states in which the TFSI<sup>-</sup> ions diffuse very slowly.

## 2.2. Results and Discussion

In this work, the diffusion of 1-ethyl-3-methylimidazolium and bis(trifluoromethylsulfonyl)-imide ions (EMIM<sup>+</sup> and TFSI<sup>-</sup> ions) inside slit-shaped micropores is studied using molecular dynamics (MD) simulations with detailed molecular models for the ions (see Figure 2-5). The diffusion coefficient of ions inside a pore depends on the internal state of the pore, which can be characterized using the density of cations and anions inside the pore ( $\rho_+$  and  $\rho_-$ ), or equivalently, the net charge and the total ion density inside the pore ( $q = \rho_+ - \rho_-$  and  $\rho_\Sigma = \rho_+ + \rho_-$ ). All densities are presented as area density hereafter since ions form a single layer in most of the pores studied here. When charging a pore,  $q$  and  $\rho_\Sigma$  are not uniform along the pore length and

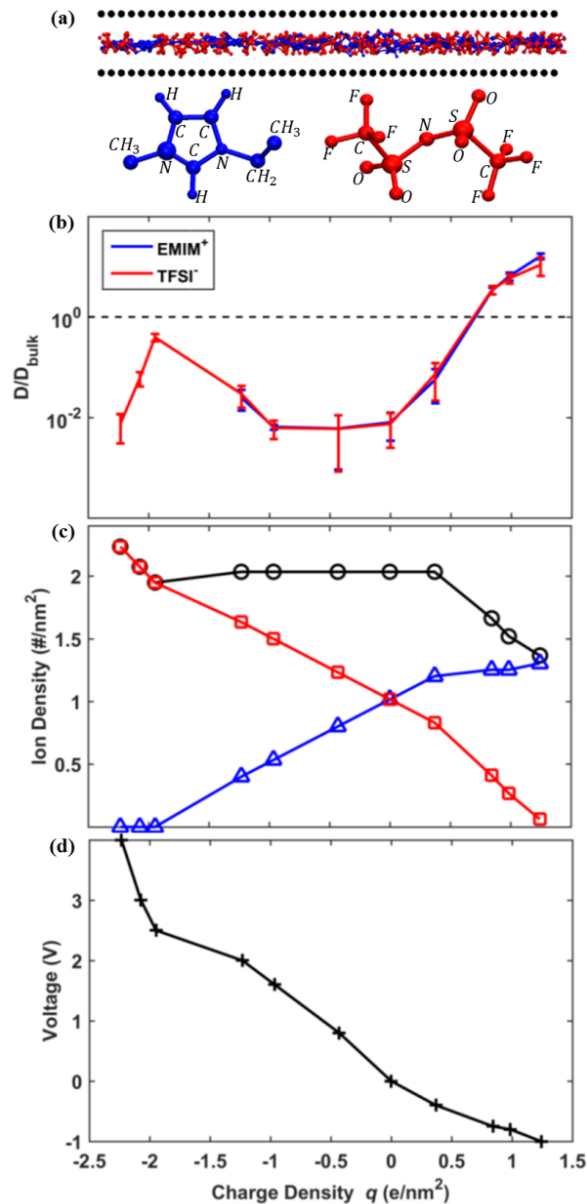


**Figure 2-5.** Ion diffusion inside a 0.75 nm slit pore. The systems were under quasi-static charging conditions. (a) A snapshot of the simulation system and the molecular models of the EMIM<sup>+</sup> and TFSI<sup>-</sup> ions. (b-c) The scaled ion diffusion coefficient (panel b) and density (panel c) as a function of ionic density  $q$  inside the pore during quasi-static charging ( $q = \rho_+ - \rho_-$ ). (d) Voltage on the pore walls as a function of ionic density  $q$ . The black line in panel c denotes the total ion density. Panel c and d are adapted from Ref. 70. Ion densities in panel c are presented as area density as the ions confined in the pore form a single layer.

vary with time, which make the quantitative study of ion diffusion under conditions relevant to pore charging complicated. However, prior studies on the impulsive charging of subnanometer pores have shown that the overall charging behavior is closely correlated with the diffusion coefficients of ions inside the pore under quasi-static (infinitely slow) charging conditions<sup>57</sup>. Therefore once the net charge  $q$  inside the pore is known during quasi-static charging, the total ion density inside the pore ( $\rho_{\Sigma}$ ) can be uniquely determined from the thermodynamics of charge storage inside pores, thus making it possible to set up MD simulations to study the ion diffusion. In what follows, the evolution of the self-diffusion coefficients of EMIM<sup>+</sup> and TFSI<sup>-</sup> ions are mapped out during the quasi-static charging of several pores. Slit pores with center-to-center widths of 0.72, 0.75, and 1.1 nm are considered, in part because the quasi-static charge storage behavior (i.e.,  $\rho_{\Sigma} - q$  relation) in these pores has been determined by some of us earlier.<sup>70</sup> The number densities of the cation and anion in these pores under different charging conditions correspond to different voltages on the pore walls and are taken from Ref. 70 (also see Table 2-1 to Table 2-3) to set up the diffusion simulations.

First the diffusion of RTIL in a 0.75 nm pore were examined. Figure 2-5b shows the evolution of the diffusion coefficients of the EMIM<sup>+</sup> and TFSI<sup>-</sup> ions inside the pore when it is charged under quasi-static conditions (the electrode voltage corresponding to different charge inside pore are shown in Figure 2-5d). The diffusion coefficients of the EMIM<sup>+</sup> and TFSI<sup>-</sup> ions are close to each other. In addition, they generally increase as charging of the pore proceeds, except when the ionic charge density,  $q$ , inside the pore reduces below  $-2 e/\text{nm}^2$ . For the TFSI<sup>-</sup> ions, the diffusion coefficient approaches their bulk value when  $q$  is  $-2 e/\text{nm}^2$ . On the other hand, the diffusion of EMIM<sup>+</sup> ions is faster than in bulk RTIL at  $q > 0.7 e/\text{nm}^2$  and even becomes faster than Na<sup>+</sup> ions in bulk water<sup>108</sup> for  $q \gtrsim 0.9 e/\text{nm}^2$ . Comparison of the ion diffusion coefficients and

ion densities inside the pore as a function of pore charge (see Figure 2-5b, c) indicates that the ion diffusion coefficient inside the pore tends to increase (decrease) as the total ion density  $\rho_{\Sigma}$  and hence ion packing decrease (increases). These observations are qualitatively similar to that observed from simulations using coarse-grained ions confined in sub-nanometer pores<sup>57</sup>. However, when the pore becomes more charged while the total ion density inside the pore remains constant, the dependence of the EMIM<sup>+</sup> and TFSI<sup>-</sup> ion's diffusion coefficients on pore charges is more complicated than that observed with coarse-grained ions. Specifically, for RTILs featuring nearly spherical, coarse-grained ions, the ion diffusion speeds up greatly as the pore becomes charged, even if the total ion density is fixed. This speed-up originates from the fact that, as charging proceeds, the interlocked cation-anion lattice inside the pore is gradually broken, which facilitates ion diffusion<sup>57</sup>. When the molecular details are included, such a speed up is indeed observed for the EMIM<sup>+</sup> ions when  $q$  increases from 0 to  $\sim 0.5$  e/nm<sup>2</sup>, but not for TFSI<sup>-</sup> ions when  $q$  decreases from 0 to  $\sim -1.0$  e/nm<sup>2</sup>. This asymmetric behavior is likely caused by the fact that TFSI<sup>-</sup> ions are slightly more bulky than the EMIM<sup>+</sup> ions and they have more tortuous structure with a larger aspect ratio than the disk-like EMIM<sup>+</sup> ions, leading to the difference in the efficiency of ion packing inside the pores. Specifically, when charging of the pore proceeds by swapping EMIM<sup>+</sup> ions inside the pore with TFSI<sup>-</sup> ions in the RTIL reservoir (thus  $q$  inside the pore becomes more negative but the total ion density inside pore remains constant), ions inside the pore become more tightly packed, and the movement of ions becomes more hindered by the irregularly shaped TFSI<sup>-</sup> ions.

The critical role of the total ion density (hence ion packing) and the more subtle role of ion shape in determining ion diffusion inside the pore can be rationalized as follows. In the absence of solvents, the movement of a RTIL ions confined in narrow pores is hindered greatly by its

neighbors. These neighbors can be thought to form a cage surrounding each ion, and the random diffusion of the ion “locked” in the cage requires the cage to be broken. In a densely populated pore, the breakage of such cage often must involve coordinated movement of many ions, and hence the ion diffusion is slow. The interlocking of ions with complex shape also compounds the situation, making the diffusion even slower. If the pore is only sparsely populated, the breakage of such a cage involves only movement of a few ions and the shape of ions plays a marginal role in hindering ion diffusion. To corroborate these ideas, the breakage of ion cages<sup>109</sup> were analyzed by computing the time correlation function of ion cages<sup>110</sup>

$$ACF_c(t) = \langle C(0)C(t) \rangle \quad (2-3)$$

where the bracket  $\langle \dots \rangle$  denotes ensemble average and  $C(t)$  is an indicator of the cage around an ion:  $C(t)$  is defined as 1.0 if the cage surrounding an ion at  $t=0$  still exists at time  $t$  later, and zero if the composition of the cage of an ion  $i$  at time  $t$  is different from that at time  $t=0$  (i.e., the cage is broken). At any given time, to identify which ions form the cage of an ion  $i$ , the distance of the

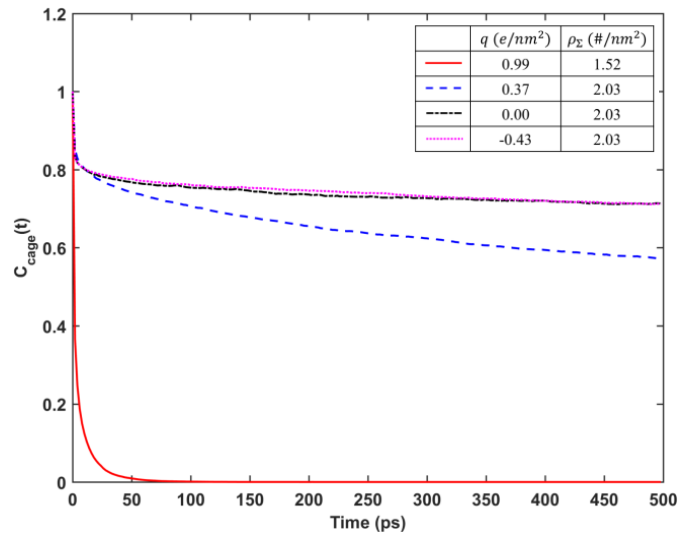


**Figure 2-6.** Cage dynamics for EMIM<sup>+</sup> ions. The ions were confined inside a 0.75 nm pore. The dynamics of the “cage” surrounding the EMIM<sup>+</sup> ions is characterized using the cage time correlation function (Equation 2-3) in pores with different charge  $q$  and total ion density  $\rho_{\Sigma}$ .

ion  $i$  to each ion  $j$  in the system,  $r_{i-j}$ , is computed. If  $r_{i-j}$  is smaller than  $r_{\min}$ , the position of the first valley of the radial distribution function of ion pair  $i-j$  in bulk RTILs, then ion  $j$  is counted as a member of the cage for ion  $i$ . A fast decay of  $ACF_c(t)$  toward zero means that the cage surrounding an ion breaks rapidly after forming. Figure 2-6 shows the  $ACF_c(t)$  of EMIM<sup>+</sup> ions confined in the 0.75 nm pore at different level of charging (the  $ACF_c(t)$  of the TFSI<sup>-</sup> ions shows very similar trend and thus is not shown). It can be seen that, as the total ion density inside the pore  $\rho_\Sigma$  decreases from 2.03 to 1.52 #/nm<sup>2</sup> while the ionic charge inside pore,  $q$ , increases from 0.37 to 0.99 e/nm<sup>2</sup>, the cage surrounding EMIM<sup>+</sup> ions breaks much faster, consistent with the speed-up of EMIM<sup>+</sup> ion diffusion shown in Figure 2-5b. When the pore charge varies from 0 to 0.37 e/nm<sup>2</sup> and from 0 to -0.43 e/nm<sup>2</sup>,  $\rho_\Sigma$  is constant. In the former case ( $q: 0 \rightarrow 0.37$  e/nm<sup>2</sup>), the ion cage breaks slightly faster, which is consistent with the moderately faster EMIM<sup>+</sup> ion diffusion. The faster cage breakage is due to the presence of more disk-like shaped EMIM<sup>+</sup> ions in the pore, which have less impedance to the breakage of ion cage. On the other hand, in the second case ( $q: 0 \rightarrow -0.43$  e/nm<sup>2</sup>), the dynamics of the cage surrounding EMIM<sup>+</sup> ions shows little change, again consistent with the fact that the diffusion of EMIM<sup>+</sup> ion changes little. This is because more bulky and tortuous TFSI<sup>-</sup> ions populate in the pore as the charge decreases from 0, which tend to hinder the breakage of ion cages.

The fact that  $ACF_c(t)$  decreases notably at short time ( $t < 30$  ps) but decreases very slowly at long time when the pore charge is 0 or -0.43 e/nm<sup>2</sup> indicates that the EMIM<sup>+</sup> ions mostly vibrate inside the cage but the overall motion of all ions is largely arrested. To some extent, EMIM<sup>+</sup> ions also diffuse with their “ionic solvation” shell nearly intact, although visualization of ion trajectories suggests that this mode of diffusion does not dominate the ion transport. Figure 2-7 shows the correlation between the mean square displacement and the cage dynamics. Overall, the

fast (slow) cage dynamics of the EMIM<sup>+</sup> ions at short (long) time appears to be consistent with the fact that their mean-square-displacement increases relatively rapidly at short time but very slowly at long time.

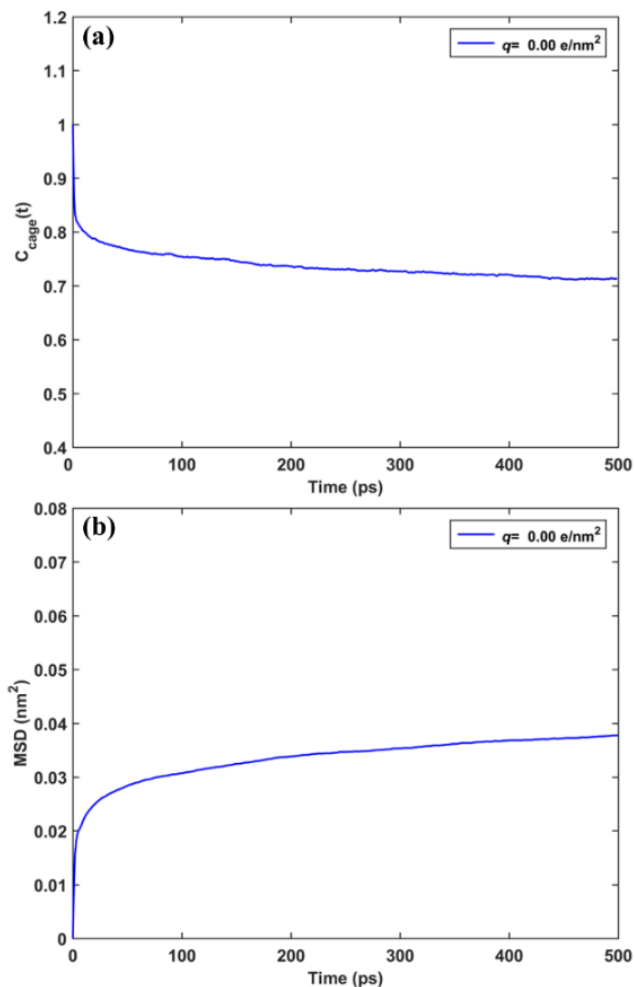


**Figure 2-7.** Dynamics of cations at zero charge condition. The ions were confined inside a 0.75 nm pore and  $q=0 \text{ e/nm}^2$ . (a) The Cage dynamics of EMIM<sup>+</sup> ions characterized using the cage time correlation function (Equation 2-3). (b) The mean-square displacement of the EMIM<sup>+</sup> ions in the  $xy$ -plane parallel to the pore walls.

Next the diffusion of RTIL in a 0.72 nm pore was investigated. The diffusion of the EMIM<sup>+</sup> ions in the pore (see Figure 2-8) shows some features similar to those in the 0.75 nm pores: their diffusion speeds up as the pore charge increases from 0 to  $0.67 \text{ e/nm}^2$  which is accompanied by a

decrease of the total ion density inside the pore; their diffusion slows down as the pore charge reduces below zero, when the total ion density inside pore increases. However, the diffusion of TFSI<sup>-</sup> ions is quite different from that in the 0.75 nm pore. As can be seen from Figure 2-8, the

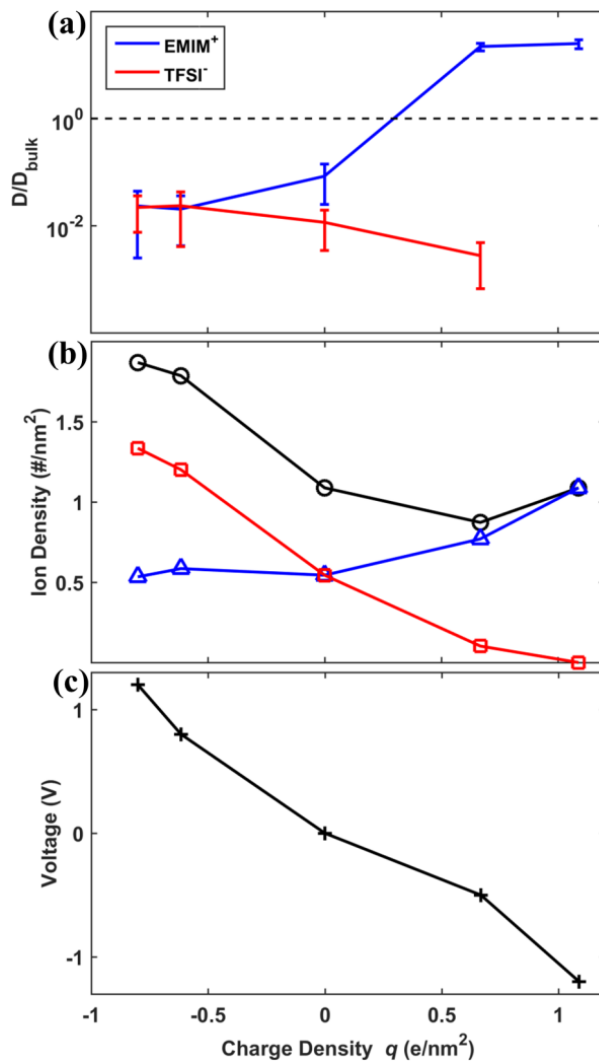


**Figure 2-8.** Ion diffusion inside a 0.72 nm slit pore. The scaled ion diffusion coefficient (panel a) and density (panel b) as a function of the ionic density  $q$  under quasi-static charging conditions. (c) Voltage on the pore walls as a function of ionic density  $q$ . Panel b and c are adapted from Ref. 70.

diffusion of TFSI<sup>-</sup> ions changes little when the pore becomes either positively or negatively charged. The different response of the EMIM<sup>+</sup> and TFSI<sup>-</sup> ions' diffusion to the charging of the pores originates mostly from the more ellipsoidal shape of the TFSI<sup>-</sup> ions compared to the rather

planar, disk-like EMIM<sup>+</sup> ions. The effect of the difference in shape is especially pronounced when the ions are confined in the narrower 0.72 nm pore. Specifically, because of its ellipsoidal shape, regardless of how a TFSI<sup>-</sup> ion is situated within the 0.72 nm pore, its multiple constituent atoms will be in close contact with the pore wall (see Figure 2-9a). Accordingly, the conformation of the TFSI<sup>-</sup> ions is strongly constrained by the pore wall, and the transition between the two different conformers (i.e. C1 and C2 conformers (Figure 2-9b)) is severely impeded (Figure 2-9c).

Consequently, the steric interactions between the TFSI<sup>-</sup> ions and the pore wall dominate the movement of the TFSI<sup>-</sup> ions, leading to their inertness in the 0.72 nm pores regardless of the pore charge density. These steric interactions are extremely sensitive to the pore width. In fact, in the 0.75 nm pore, these interactions already become much weaker, as hinted by the more facile transition between their C1 and C2 conformation (see Figure 2-9c). As a result, the diffusion of TFSI<sup>-</sup> ions in the 0.75 nm pore is much faster. For the disk-like EMIM<sup>+</sup> ions, which tend to position themselves along the middle plane of the 0.72 nm pore, few of their atoms are in close contact with the wall atoms. Consequently, the diffusion of EMIM<sup>+</sup> ions is not restricted by the wall but instead governed more strongly by caging from other ions. To ascertain that it is the ion-wall interactions rather than other factors such as ion-ion interactions that dominate the slow diffusion of TFSI<sup>-</sup> ions in the 0.72 nm pore, the simulation was repeated with  $q = 0.67 \text{ e/nm}^2$  and  $\rho_{\Sigma} = 0.87 \text{ \#/nm}^2$  by increasing the pore width from 0.72 nm to 0.75 nm without changing the number of ions inside the pore. The diffusion coefficient of TFSI<sup>-</sup> ions was found to increase by ~100 times, thus confirming the decisive role of steric ion-wall interactions in controlling the diffusion of TFSI<sup>-</sup> ions in the 0.72 nm pore.

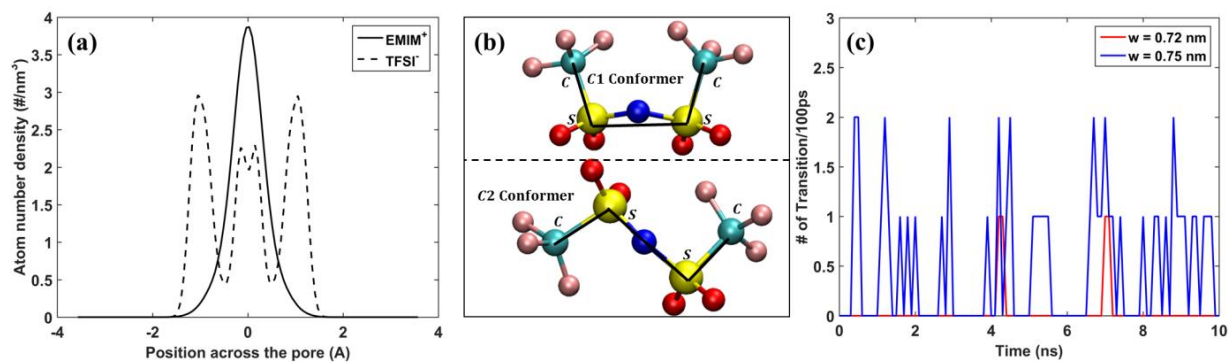


**Figure 2-9.** Structures of EMIM<sup>+</sup> and TFSI<sup>-</sup> ions confined inside micropores. (a) The atom number density profiles of EMIM<sup>+</sup> and TFSI<sup>-</sup> ions across a 0.72 nm pore ( $q = 0.67 \text{ e/nm}^2$  and  $\rho_{\Sigma} = 0.87 \text{ \#/nm}^2$ ). Each atom of an ion contributes equally to its atom number density profile. (b) Geometry of the C1 and C2 conformers of a TFSI<sup>-</sup> ion. These conformers are distinguished based on the angle of the pseudo-dihedral form by the C-S-S-C atoms.<sup>111</sup> The yellow, cyan, pink, and red balls denote the S, C, F and O atoms, respectively. (c) Comparison of the rate of transition between the C1 and C2 conformers of TFSI<sup>-</sup> ions confined inside the 0.72 nm pore ( $q = 0.67 \text{ e/nm}^2$ ,  $\rho_{\Sigma} = 0.87 \text{ \#/nm}^2$ ) and inside the 0.75 nm pore ( $q = 0.54 \text{ e/nm}^2$ ,  $\rho_{\Sigma} = 0.88 \text{ \#/nm}^2$ ) during a 10 ns simulation. The transition between the C1 and C2 conformers occurs if the angle of the pseudo-dihedral formed by the C-S-S-C atoms changes by more than 120 degrees.

Finally, the ion packing and dynamics within a 1.1 nm pore is compared with the results for 0.72 and 0.75 nm pores. The 1.1 nm pore was chosen because it is wide enough to accommodate two layers of ions. Figure 2-10 shows the evolution of ion diffusion coefficients and densities inside the pore during charging under the quasi-static condition. Unlike the observations for the narrower pores shown in Figure 2-5 and Figure 2-8, the diffusion coefficients of both EMIM<sup>+</sup> and TFSI<sup>-</sup> vary rather modestly with the pore charge. This is similar to the situation in the mesopores studied by other research groups<sup>76-79</sup> and also in line with the fact that the total ion density inside the pore varies only marginally as the pore becomes charged. Moreover, in the investigated charge range, both EMIM<sup>+</sup> and TFSI<sup>-</sup> ions only show much slower dynamics than in bulk.

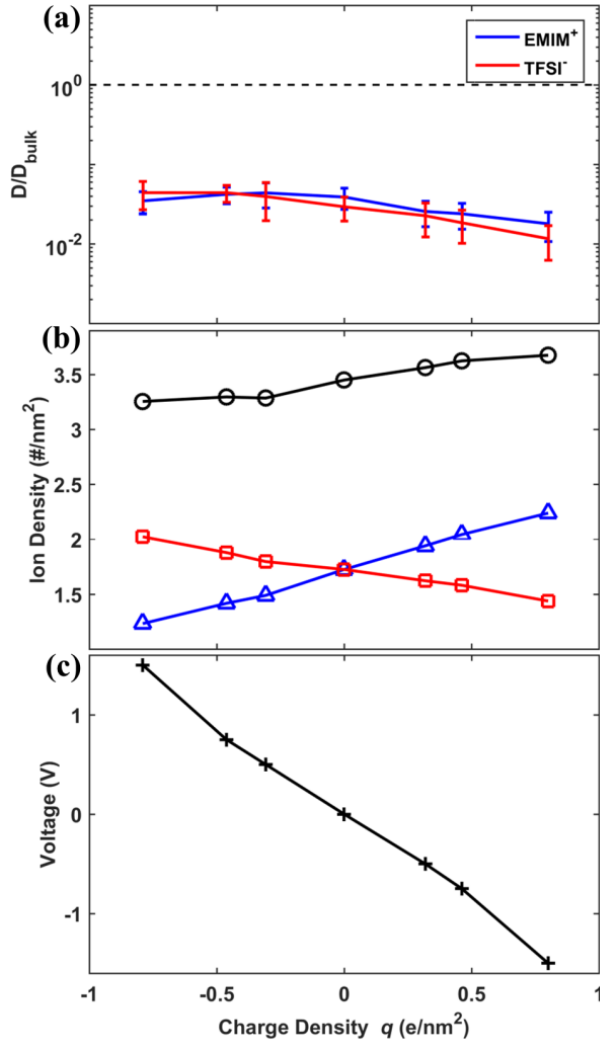


**Figure 2-10.** Ion diffusion inside a 1.1 nm slit pore. The scaled ion diffusion coefficient (panel **a**) and density (panel **b**) as a function of the ionic density  $q$  under quasi-static charging conditions. (c) Voltage on the pore walls as a function of ionic density  $q$ . Panel **b** and **c** are adapted from Ref. 70.

### 2.3. Conclusions

In summary, an unexpected picture of ion transport in charged micropores has emerged from MD simulations, where complex-shaped ions were represented using an all-atom models. In the pores that accommodated only one layer of ions, the diffusion coefficient of an ion increased greatly during charging and exceeded the bulk diffusion values or even diffusion coefficients of

small monovalent cations in bulk water. In the wider pores that accommodated more than one layer of ions, ions diffusion was slower than in bulk RTILs and largely independent of the state of charge. Overall, although many factors affect the ion diffusion, the ion packing typically plays the most important role. These results highlight the importance of understanding the charge dependence of ion diffusion in addition to the pore size dependence. These results also highlight the importance of precisely controlling pore size to realize fast ion diffusion in charged pores. In many practical materials, the large variation of pore size often leads to formation of diffusion bottlenecks as pore expands and narrows along its length, thus limiting the power density of the supercapacitors. Such limitation can potentially be resolved using precisely templated carbons.<sup>112</sup> In absence of precise pore size control, hierarchical carbons with combined micro- and mesopores may offer the best compromise between energy and power density as large pores will provide supply of ions to narrow pores with size comparable to ion sizes.

## CHAPTER 3

### Dynamic Charge Storage in RTIL-filled Nanopores<sup>†</sup>

Understanding the dynamic charge storage in nanoporous electrodes with room-temperature ionic liquids is essential for optimizing them to achieve supercapacitors with high energy and power densities. This chapter reports coarse-grained molecular dynamics simulations of the cyclic voltammetry of supercapacitors featuring subnanometer pores and model ionic liquids. The results show that the cyclic charging and discharging of nanopores are governed by the interplay between the external field-driven ion transport and the sloshing dynamics of ions inside the pore. The ion occupancy along the pore length depends strongly on the scan rate and varies cyclically during charging/discharging. Unlike that at equilibrium conditions or low scan rates, charge storage at high scan rates is dominated by counterions while the contribution by co-ions is marginal or negative. These observations help explain the perm-selective charge storage observed experimentally. The results clarify the mechanisms underlying these dynamic phenomena and quantify their effects on the efficiency of the dynamic charge storage in nanopores.

---

<sup>†</sup> This chapter is adapted with permission from the following paper (Ref. 113):

He, Y.; Huang, J.; Sumpter, B. G.; Kornyshev, A. A.; Qiao, R., Dynamic Charge Storage in Ionic Liquids-Filled Nanopores: Insight from a Computational Cyclic Voltammetry Study. *The Journal of Physical Chemistry Letters* **2015**, *6*, 22-30.

Copyright 2015 American Chemical Society.

### 3.1. Models, Simulation System and Methods

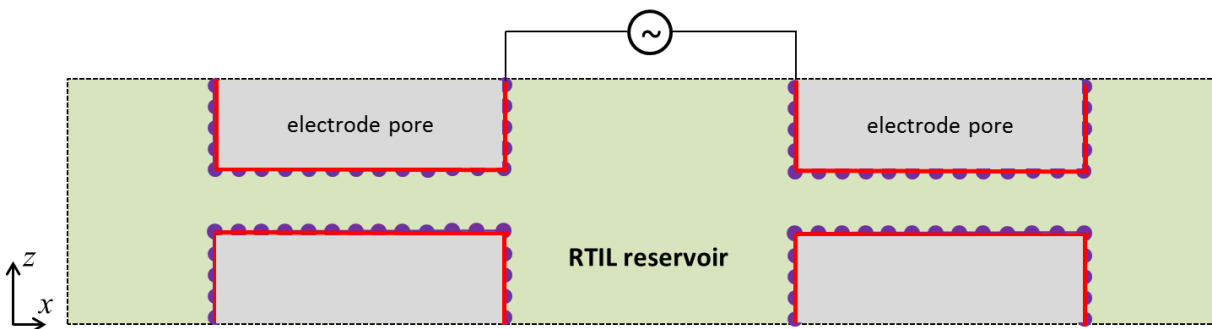


**Figure 3-1.** A schematic of the system used for MD simulations. The red solid lines denote the image planes of the electrode pore walls and the black dashed lines denote the simulation box. The system is periodic in all three directions. The length of each pore and RTIL reservoir is 12.09 and 10.92 nm, respectively. The two pores inside each MD system have the same center-to-center width of either 0.78 or 0.91 nm. This figure is adapted with permission from Fig. S2 of Ref. 57. Copyright 2014 Springer Nature.

MD simulations of the cyclic voltammetry of subnanometer pores connected with RTIL reservoirs are performed. The MD simulation system consists of a pair of identical slit pores and RTIL reservoirs (see Figure 3-1 and Figure 3-2). The system contains 6048 wall atoms, and also includes 1180 and 1200 pairs of cations and anions for two separate studies with 0.78 and 0.91 nm pores, respectively. The length of each pore and each reservoir is 12.09 nm and 10.92 nm, respectively. Each pore wall is made of a square lattice of LJ particles with an atom spacing of 0.17 nm. Each anion has the same geometry as the  $\text{BF}_4^-$  ion, with a nearly spherical shape. The constituent atoms are modeled as Lennard-Jones (LJ) particles and a unit negative charge was assigned to its central atom. The cation is identical to the anion except that its central atom is positively charged. To account for the electronic polarizability of RTILs, a background dielectric constant of 2.5 was used when computing the electrostatic interactions. The LJ potential describing the non-electrostatic interactions between neighboring atoms is given by  $\phi_{LJ} =$

$4\epsilon \left[ \left( \frac{\sigma}{r} \right)^{12} - \left( \frac{\sigma}{r} \right)^6 \right]$ , where the LJ parameters of  $\sigma = 0.336$  nm and  $\epsilon = 0.36$  kJ/mol are the same for all atoms in the system.

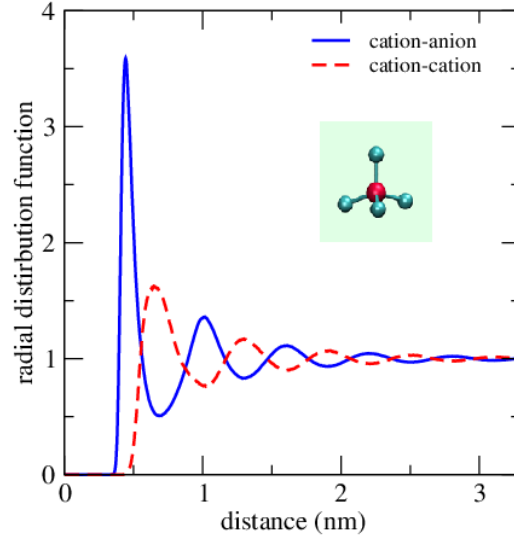


**Figure 3-2.** Radial distribution function (RDF) for the bulk model of RTILs. Temperature is 400 K and pressure is 1 atm. Both the cation-cation and cation-anion RDFs are calculated. The positions of the cation and anion are based on their central atoms. The inset shows a schematic of the cation. The geometry of the anion is the same as that of the cation.

The bulk density of the model RTILs considered here is  $4.11 \text{ \#/nm}^3$  for cations and anions ( $T = 400 \text{ K}$ ,  $P = 1 \text{ atm}$ ). Figure 3-2 shows the cation-anion radial distribution function (RDF) in the bulk RTILs, which suggests that the diameter of each ion is  $\sim 0.45$  nm. The self-diffusion coefficient of ions in bulk RTILs under the same conditions was found to be  $D^+ = D^- = 2.32 \times 10^{-9} \text{ m}^2/\text{s}$ , which is  $\sim 1$ - $2$  order of magnitude larger than that of typical RTILs used in supercapacitors. Such a large diffusion coefficient is predominantly caused by the elevated temperature (400 K) at which the simulations were performed. The elevation of temperature is the standard procedure in the simulations of simplified model ionic liquids, which helps to speed up the computation to reasonable times as well as prevents solidification<sup>70-71, 114-116</sup>. The high diffusion coefficient is useful since simulating large systems featuring polarizable electrodes is computationally

demanding and the fast diffusion of ions allows cyclic voltammetry with various scanning rates to be simulated using modest computational resources.

With the choice of model RTILs and nanopores described above, ions effectively form a single layer inside the two pore widths considered (see Figure 3-3). Therefore, the area density was used to characterize the distribution of ions inside the nanopore.

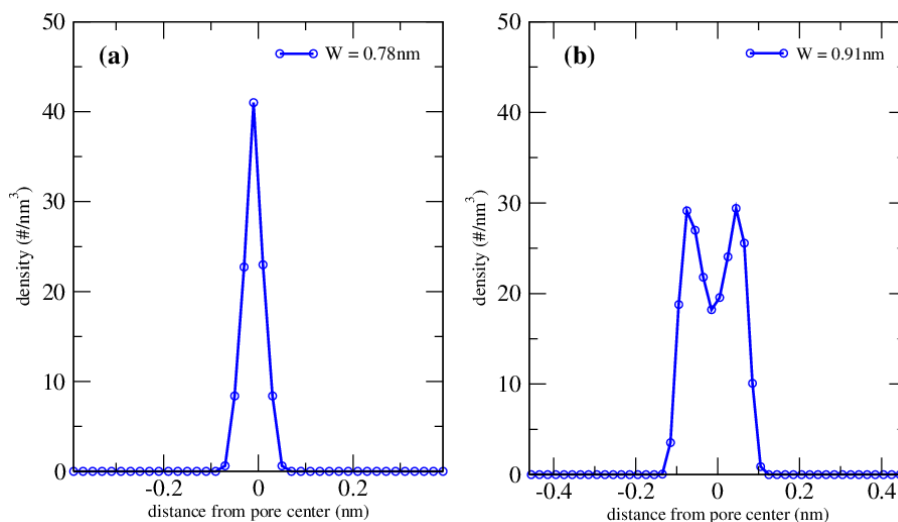


**Figure 3-3.** Density profile of cations across the pore: (a) 0.78 nm-wide (b) 0.91 nm-wide pore at the PZC state. The positions of ions are based on their central atoms. In (b), there are two weak peaks corresponding to two ion layers inside the pore. However, since the separation between these peaks is less than the ion radius, these barely distinguishable ion layers can effectively be treated as one single layer. The density profile of the anion is essentially the same as that of the cation and therefore is not shown.

The walls of each pore are maintained as ideally polarizable surfaces using a modified Gromacs code<sup>117</sup>. Prior studies have concluded that it is important that the charging of nanopores is simulated by enforcing a constant potential on each pore wall rather than assigning static charges to wall atoms<sup>118</sup>. Here the electrical potential on the pore wall was enforced within the framework of continuum electrostatics<sup>119</sup>: each pore wall was modeled as an equipotential surface with its image plane coinciding with the geometric plane of the wall atoms. This method has produced

similar results compared to other methods for enforcing electrical potential on pore walls<sup>70-71, 120</sup>. The slit shape of the pore is similar to that found in an emerging class of electrode materials based on graphene and MXene, which feature well-aligned pores with large length-to-width aspect ratios<sup>121-122</sup>. Cations and anions of the model RTILs are nearly spherical and of identical size, and their specific interactions with the pore walls are not taken into account. With these coarse-grained models, the purpose is to reveal the essential physics of the collective interactions of ions in subnanometer pores and their manifestations in the dynamics of charge storage. The main idea is to discuss these separately from the effects that may be caused by the chemical complexities of RTIL ions and details of interactions of ions with real electrode materials. The effectiveness of these coarse-grained models in delineating the charging dynamics in practical materials is supported by the fact that the key features of charging dynamics predicted using these models<sup>57</sup> are indeed observed in simulations employing more realistic electrode and RTIL models<sup>55</sup>.

Simulations were performed in the NVT ensemble with  $T = 400$  K. Such an elevated temperature helps increase the diffusion coefficient of the ions so that charging dynamics can be studied with the available computational resources. Simulation at lower temperature is difficult because the diffusion of ionic liquids slows down greatly as temperature reduces. Therefore, charging/discharging of the pores considered here (i.e., charge efficiency  $>20\%$ ) will require long simulation time (e.g., thousands of nanoseconds) and prohibitive amount of computer time. During each simulation, the evolutions of cation and anion densities along each pore were computed on the fly. These data were used to compute the net charge inside each pore, which was then used to compute the charging/discharging current, the energy stored (released) during the charging (discharging), and the energy efficiency of each charging/discharging cycle. Each cyclic voltammetry study was repeated three times with independent initial configurations. Further

details such as the calculations of electrostatic forces are provided in the Supporting Information. A time step of 3 fs was used in production runs. The tests indicated that, in NVE simulations of bulk RTILs based on the coarse-grained model, the energy drift is less than 0.2% over 10 ns when a time step of 3 fs was used. Such a relatively large time step is often used in coarse-grained MD simulations because some of the faster modes are no longer active due to coarse-graining.

In the MD simulations, a Berendsen thermostat with the time constant 2 ps was used to control the temperature of the RTILs. The non-electrostatic interactions were computed with a cutoff length of 1.5 nm and the neighbor list was updated every step. To take into account the electronic polarizability of pore walls, the electrostatic interactions were computed using the method developed by the Aluru group<sup>119</sup>. Specifically, the electrostatic potential and force are computed using the PME method and by solving an auxiliary Laplace equation. In the PME part, a real space cutoff of 1.5 nm was used, and FFT grid spacing was 0.13 nm. The auxiliary Laplace equation was discretized using the compact fourth-order stencil on the same grid as the FFT grid and solved during each time step.

Each cyclic voltammetry simulation begins with a pore+reservoir system pre-equilibrated with the voltage between the two pores set to zero, i.e., ions in each pore are at the potential of zero charge (PZC) state. Starting at  $t = 0$ , the voltage difference between the two pores is increased from 0 to the target potential (forward scan) and then decreased to 0 (backward scan), both at the same scan rate of  $s$ . These scans are repeated until the system reaches a periodic steady state. Simulations are performed in systems with two pore sizes separately (center-to-center width: 0.78 and 0.91 nm) and five scan rates for each pore size ( $s = 1.88, 3.75, 5, 7.5, \text{ and } 10$  V/ns). The large scan rates are commensurate with the nanoscale pore length and the fast diffusion of the RTILs due to the high temperature used in the simulations.

### 3.2. Results and Discussion

To help understand the cyclic voltammetry results, the essential features of the thermodynamics and ion transport underlying charge storage in narrow pores are recapitulated next. Under quasi-static or equilibrium conditions, these pores store charge very effectively for two reasons. First, ion-ion electrostatic interactions are strongly screened by the pore walls<sup>69</sup>. Second, in pores polarized by a given voltage, the number of co-ions inside the pore decreases when the pore width reduces, which helps suppress over-screening and “solvation” of ions by ions with opposite charges and thus leads to more effective storage of counterions in narrower pores<sup>67-68, 71-72, 115, 120</sup>. It is interesting to note that, while both counterion insertion and co-ion removal contribute to charge storage, as manifested by the peak in capacitance-voltage curves, charge storage inside narrow pores is especially effective when it is achieved mainly by removal of co-ions (also termed de-mixing of counterions and co-ions).

In addition to the above thermodynamic factors, charge storage is also affected by the transport of ions. In typical supercapacitors, the resistance for the ion transport between pore entrance and electrolyte reservoir (i.e., separators soaked with electrolytes) is small. Therefore, in response to a voltage change on the pore wall, the densities of the counter/co-ions at pore entrance quickly adjust towards their quasi-static values corresponding to the new voltage. The net transport of ions into/out of the pore is thus throttled by the internal transport of ions toward the pore entrance or interior. For example, during charging, the net flux of counterions into the pore is limited by how fast counterions are transport from the pore entrance toward pore interior. For ions inside slit-shaped pores with width comparable to the ion size, their fluxes, according to a recent mean-field theory, can be given by<sup>57, 89</sup>

$$J_{\pm} = -D_{\pm}\nabla\rho_{\pm} \mp D_{\pm}\rho_{\pm}G\nabla q - D_{\pm}\rho_{\pm}/(\rho_{\max} - \rho_{\Sigma})\nabla\rho_{\Sigma} \quad (3-1)$$

where  $D_{\pm}$  is ion diffusion coefficient,  $\rho_{\pm}$  is the ion density,  $q = \rho_{+} - \rho_{-}$  is the ionic charge in unit of elementary charge,  $\rho_{\Sigma} = \rho_{+} + \rho_{-}$  is the total ion density, and  $\rho_{\max}$  is the total ion density at close packing. In Equation 3-1,  $G = e^2/\pi\epsilon_p k_B T \sum_{n=1}^{\infty} \sin^2(\pi n/2)/n K_1(n\pi R_c/L)$ , where  $e$  is the elementary charge,  $\epsilon_p$  is the permittivity inside the pore,  $k_B T$  is the thermal energy,  $K_1$  is the modified Bessel function of the second kind of the first order,  $R_c$  is the cut-off radius, and  $L$  is the pore width.  $G$  characterizes the screening of ion-ion electrostatic interactions by the conducting pore walls. The first term of Equation 3-1 is the diffusion of ions. The second term is the electrical ion migration originating from electrostatic ion-ion interactions, and it often dominates the overall ion transport. The last term denotes the ion transport due to the gradient of the total ion density along the pore. While mechanisms such as ion transport due to hydrodynamic flows and friction between different ion species are not accounted for in this model, Equation 3-1 can provide an effective description of the ion transport in narrow pores, especially when the counterion and co-ion densities do not differ greatly. When the density of counterions inside a pore far exceeds that of the co-ions, the transport of co-ions approaches simple diffusion, likely because the driving force for their electrical migration is overestimated in Equation 3-1.

Equation 3-1 has two straightforward implications. First, as proved in the recent MD simulations<sup>57</sup>, it suggests that ion transport is more effective in wider pores because  $G$  increases as pores become wider. Second, since the migration flux of an ion species is proportional to its density and both counterions and co-ions are driven by the same gradient of ionic charge, Equation 3-1 suggests that the flux of counterions, whose density is always higher than that of the co-ions, is typically higher than that of the co-ions. Trivially, the flux of any ion species inside the pore tends to be higher when its density is larger. These latter two effects have not yet received significant

attention in the study of dynamic charge storage. However, as detailed below, they can play a key role in the intriguing phenomena revealed in recent experimental in-situ studies of ion dynamics in supercapacitors<sup>87-88</sup>.

### 3.2.1. Initial Transients of Cyclic Voltammetry

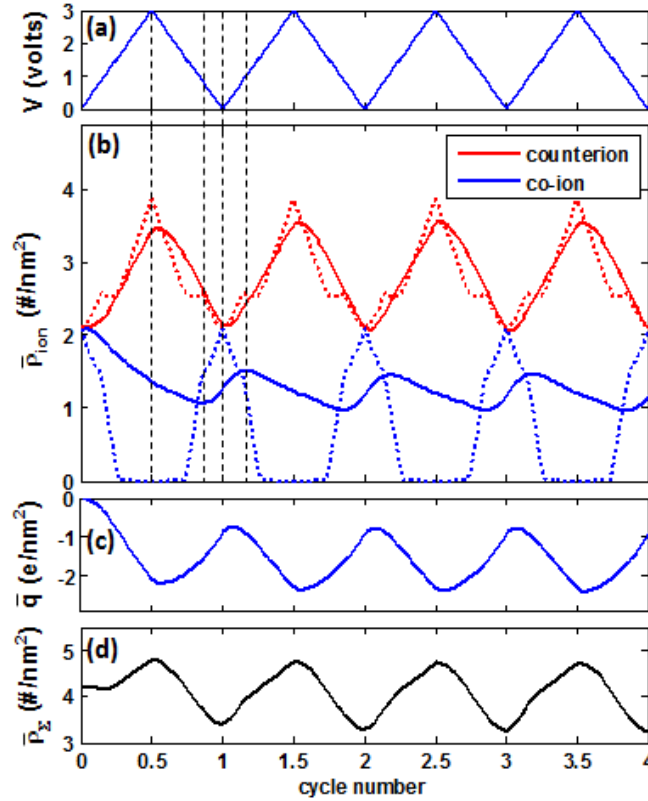


**Figure 3-4.** Charging and discharging of a 0.78 nm-wide electrode pore. Only the first few cycles are shown. Scan rate is 5 V/ns. **(a)** Evolution of the voltage on pore walls. **(b-d)** Evolution of the average counterion and co-ion densities ( $\bar{\rho}_{count,co}$ ), charge density  $\bar{q}$ , and total ion density  $\bar{\rho}_{\Sigma}$  inside the pore ( $\bar{q} = \bar{\rho}_{co} - \bar{\rho}_{count}$ ;  $\bar{\rho}_{\Sigma} = \bar{\rho}_{co} + \bar{\rho}_{count}$ ). In **(b)**, the evolution of ion densities during quasi-static charging/discharging is shown as dotted lines. Densities are presented as area density as the ions confined in the pore form a single layer.

Because the system is symmetric in both the geometries of the positively/negatively charged pores and the structure of the cations/anions, only the charge storage in the positively charged pore will be discussed. Figure 3-4 shows the first few cycles of the charging and

discharging of a 0.78 nm-wide pore at a scan rate of 5 V/ns, which is representative of all other cases examined. As voltage increases (decreases) (Figure 3-4a), counterions are inserted into (removed from) the pore, while the co-ions are removed from (inserted into) the pore (Figure 3-4b). Their responses to the applied voltage deviate from those in the quasi-static limit. While the insertion/removal of counterions is synchronized quite well with the evolution of the applied voltage, the response of co-ions lags significantly behind. Indeed, co-ions are removed from the pore well beyond the conclusion of the first forward scan; they start to be inserted into the pore only when the first backward scan is nearly finished (cf. the second vertical dashed line in Figure 3-4b) and their insertion terminates shortly after the second forward scan starts (cf. the fourth vertical dashed line in Figure 3-4b). These features, i.e., prolonged removal of co-ions until the voltage is decreased to  $\sim 1$  V and quick termination of co-ion insertion once the voltage increases back to  $\sim 1$  V, are repeated in subsequent cycles. The response of counterions and co-ions to the cyclic voltage reaches a periodic steady state within about three cycles, in line with that observed in experimental studies<sup>86-87</sup>.

The different responses of counterions and co-ions to the applied voltage have both dynamic and thermodynamic origins. As described above, the flux of counterions inside pore is usually stronger than that of the co-ions because of their higher density. This phenomenon, along with the fact that the net flux of an ionic species into/out of the pore is dominated by the transport of this species inside the pore toward the pore interior/entrance, causes counterions to respond more effectively to the evolving voltage applied on the electrode than co-ions. This trend is especially pronounced at times when the density of counterions inside the pore is already much larger than that of the co-ions. For example, Figure 3-4b shows that, while the counterion's insertion rate is comparable to the co-ion's removal rate at the initial stage of the first forward scan,

it soon exceeds the co-ion's removal rate as charging proceeds, i.e., as the pore becomes populated by more counterions but fewer co-ions.

A consequence of the slow removal of co-ions from the pore during the first forward scan (the “charging” scan) is that co-ions continue to be removed from the pore during a significant portion of the first backward scan (the “discharging” scan). Specifically, at the end of the first forward scan, co-ions remain of high density inside the pore, although from a thermodynamic perspective the voltage on the pore wall demands co-ions to be fully depleted (c.f. the density of co-ions at the quasi-static condition in Figure 3-4b). Therefore, co-ions continue to be removed during the backward scan until the voltage on the electrode drops to  $\sim 1$  V, when the density of co-ions inside the pore becomes comparable to that thermodynamically demanded by the voltage.

The different response of counterions and co-ions to the voltage cycling identified above leads to interesting phenomena. Because counterion insertion (removal) and co-ion removal (insertion) are generally not synchronized and their rates are also different, the cycling of the applied voltage leads to not only a cycling of the net charge inside the pore (see Figure 3-4c), but also a cycling of the total ion density inside the pore (see Figure 3-4d). The latter result indicates that the total mass of a porous electrode changes periodically during charging/discharging, which has been reported experimentally and leveraged to study the mechanism of dynamic charge storage in nanoporous electrodes. Another manifestation of the different counterion and co-ion dynamics is the non-neutral state of the pore each time the voltage returns to zero (hereafter termed the **State of Zero Voltage**, or **SZV**). As expected from the classical TLM<sup>123</sup>, for pores polarized by the voltage signal in Figure 3-4a, the net ionic charge inside them is negative at each SZV. While TLM provides no information on the composition of the electrolyte inside a pore (within the classical TLM, the dynamic state of a pore is characterized by a single variable, i.e., the distribution of the

net charge along the pore), Figure 3-4b and Figure 3-4c show that, compared to the PZC state, the SZV features a weak excess of counterions and a significant shortage of co-ions, i.e., a reduced total ion density. It is worth noting that the lower total ion density at SZV compared to that at the PZC has been discovered by Richey *et al.* in the infrared spectroelectrochemical characterization of dynamic charge storage in microporous CDC electrodes (pore size: 0.85 nm) immersed in ionic liquids<sup>86</sup>. This interesting experimental observation may be related to the mechanisms delineated above.

### 3.2.2. Cyclic Charging/discharging and the Underlying Ion Dynamics

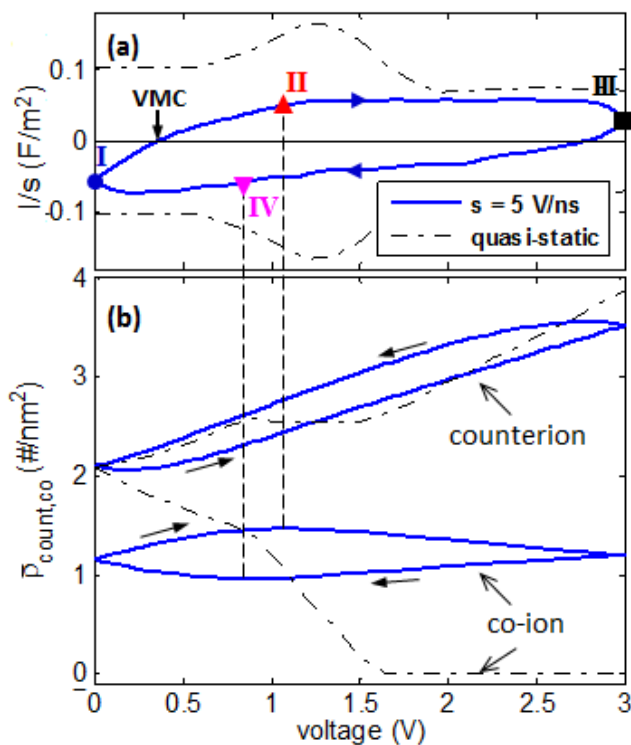


**Figure 3-5.** Current and ion density during steady-state charging/discharging cycles. Pore width was 0.78 nm. (a) The evolution of the normalized current  $I/s$ . (b) The average counterion and co-ion densities inside the pore. The evolutions of normalized current and ion densities during the quasi-static charging/discharging are shown as dot-dashed lines. Points II and IV correspond to the voltages at which the net transport of co-ions reverses its direction.

The dynamic charge storage at periodic steady states are then examined, which is the focus of most cyclic voltammetry studies. Figure 3-5a shows that the computed cyclic voltammogram closely resembles those measured experimentally<sup>88</sup>. During quasi-static charging, the normalized current shows a peak in the 1-1.5 V voltage window during forward scan, which is caused by the counter/co-ion de-mixing. Quasi-static discharging shows a symmetrical peak located in the 1-1.5 V range. In sharp contrast, these peaks disappear in cyclic voltammetry at a scan rate of 5 V/ns. Its difference from the quasi-static results gives a clear illustration of the effect of ion transport on the dynamic charge storage in nanopores.

To gain insights into what contributes to the charging and discharging currents quantified in Figure 3-5a, their underlying ion dynamics is studied (see Figure 3-5b). As detailed above, at SZV, the number of counterions inside the pore is nearly comparable to that at the PZC state, i.e., that demanded thermodynamically by the zero voltage on the pore walls. However, the number of co-ions inside the pore is much less than that at the PZC. As such, at SZV, there is a large driving force for co-ions to enter into the pore, giving a negative current (point I in Figure 3-5a). As voltage increases, the number of co-ions inside the pore increases (Figure 3-5b), which favors counterion insertion and meanwhile hinders co-ion insertion. Consequently, co-ion insertion slows down and counterion insertion speeds up; eventually the current reaches zero at  $\sim 0.38$  V where the magnitude of net charge inside the pore reaches a minimum (this voltage is termed **voltage of minimal charge**, or VMC). Interestingly, until the voltage increases further to  $\sim 1$  V (point II in Figure 3-5a), counterions and co-ions are inserted concurrently into the pore (Figure 3-5b). The ion dynamics in the remainder of the forward scan is similar to that expected from the TLM<sup>123</sup>. At the end of the forward scan (point III in Figure 3-5a), both the counterion and the co-ion densities are higher than those at the beginning of the forward scan (Figure 3-5b). The significant accumulation of

counterions is responsible for the energy storage during the charging stage. However, the net accumulation of co-ions during the forward scan indicates that they contribute *negatively* to charge storage (this effect becomes more pronounced as the scan rate increases, see Figure 3-6). This phenomenon, unique to the fast and cyclic charging of narrow pores, is caused by the persistent insertion of co-ions into the pore until  $\sim 1$  V is reached and by the sluggish removal of co-ions thereafter. The former mostly originates from the large deficiency of co-ions at the SZV compared to that at the PZC.

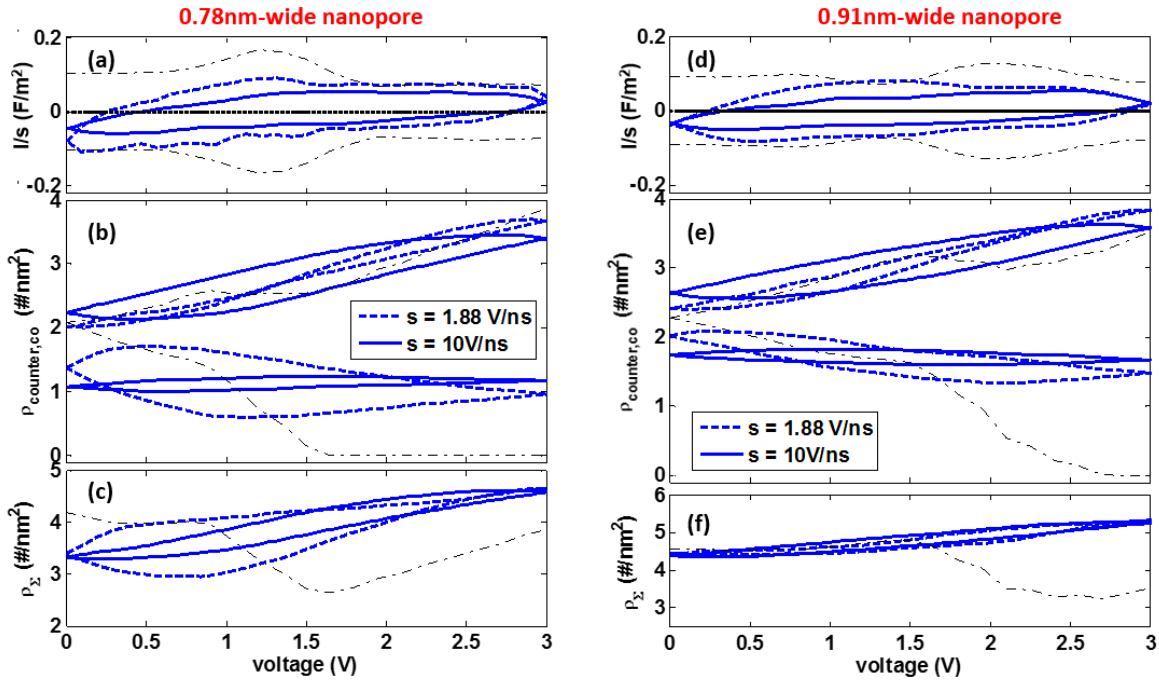


**Figure 3-6.** Current and ion density during steady-state charging/discharging of two pores. (a,d) Evolution of the normalized current  $I/s$ . (b,e) The average counterion and co-ion densities inside the pore. (c,f) The average total ion density. Those corresponding to the quasi-static charging/discharging are shown as dot-dashed black lines.

The ion dynamics during the backward scan largely follow the expected behavior: as the voltage decreases, counterions are removed from the pore while more co-ions are supposed to enter the pore. However, the number of co-ions inside the pore does not immediately increase as

the backward scan starts. In fact, their number keeps decreasing until the voltage drops to  $\sim 0.8$  V (point IV in Figure 3-5b). The persistent but sluggish removal of co-ions over such a wide voltage window has similar origins as that observed during the backward scan in the first charging/discharging cycle (see Figure 3-4b). Afterwards, the number of co-ions increased slightly until the SZV. In comparison, during the entire backward scan, the number of counterions decreases monotonically all the way to the SZV.

Overall, at the high scan rate considered here, both the charging during the forward scan and the discharging during the backward scan are dominated by the transport of counterions. The co-ions play a relatively limited role despite that they *do* participate in these processes. Their net contribution to charging is small, as their transport during the two phases of the forward scan (I $\rightarrow$ II and II $\rightarrow$ III in Figure 3-5b) essentially cancels out each other (see Figure 3-5b). The same effect applies to discharging during the backward scan.

In the discussion thus far, all ions inside the pore except those at the immediate entrance of the pore are treated in a lumped fashion. Such a treatment allows the net ion transport in/out of the pore to be analyzed qualitatively without spatially resolving the ion transport inside the pore. To scrutinize the ion dynamics during charging/discharging in greater detail, the internal ion transport is examined in a spatially resolved manner. The analysis will focus only on the electrical migration of ions because it often dominates the overall charging/discharging behavior<sup>57</sup>. Figure 3-7 shows the spatial-temporal evolution of the ionic space charge inside the pore during the four phases of a voltage cycling (I $\rightarrow$ II, II $\rightarrow$ III, III $\rightarrow$ IV, and IV $\rightarrow$ I in Figure 3-5a). The evolution of the ionic charge profile in the pore interior exhibits a sloshing pattern. In the forward scan, the ionic charge profile is concave at point I; it becomes nearly flat at point II, and convex at point III. The opposite pattern occurs during the backward scan. It is evident from Equation 3-1 that such a

sloshing of ionic charge drives ion transport within the pore: counterions (anions) migrate toward the pore entrance and co-ions (cations) move toward the pore interior in phases I→II and IV→I, delivering negative charge toward the pore entrance; the opposite process occurs in phases II→III and III→IV (see insets of Figure 3-7b to Figure 3-7e).

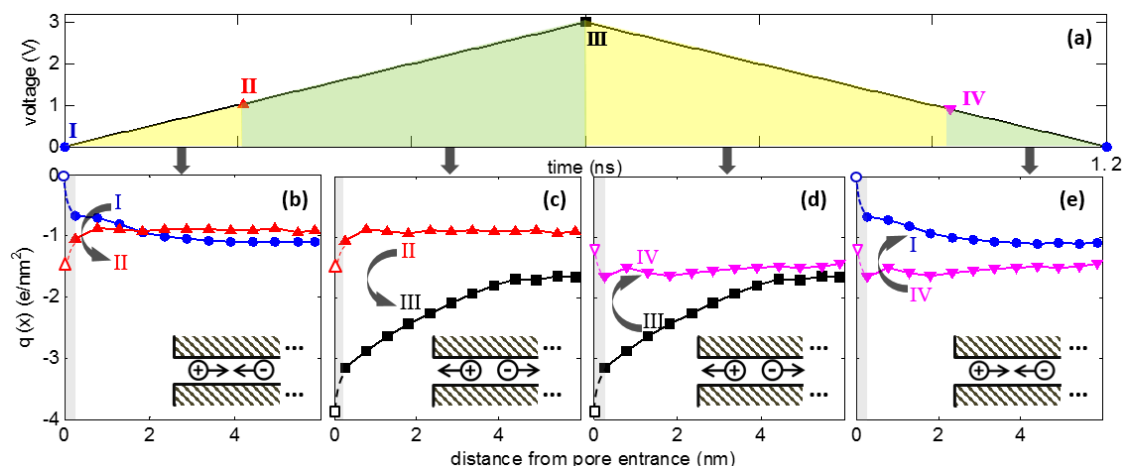


**Figure 3-7.** Ionic space charge density during cyclic charging/discharging. Pore width is 0.78 nm and scan rate is 5 V/ns. **(a)** Evolution of the voltage on the pore wall. **(b-e)** The corresponding ionic space charge density inside the pore. Points I-IV correspond to those in Figure 3-5a. As the pore is open at both ends, only the space charges between the pore entrance ( $x = 0$ ) and the pore center are shown. The variation of the ionic space charge near  $x=0$  (shaded regions in **b-e**), too sharp to be resolved in MD simulations, is shown as dashed lines with the charge at the pore entrance taken as its quasi-static value (denoted by open symbols). During phases I→II and III→IV, the electrical ion migration induced by the gradient of the ionic space charge along pore length (insets in **b-e**) counteracts the ion transport driven by the external voltage; the opposite occurs during phases II→III and IV→I.

The net ion transport in/out of the pore is a result of the interplay between the ion transport induced by an applied voltage and by the internal sloshing of ionic charges. In the forward scan, the increase of the voltage on the pore wall tends to drive anions (counterions) into the pore and cations (co-ions) out of the pore. During phase I→II, the sloshing of ionic space charge inside the pore delivers anions toward pore entrance and cations toward pore interior, thus counteracting the effect of the applied voltage. One can show that the sloshing of ionic space charge during phase

III→IV has a similar effect, but that during phases II→III and IV→I enhances the action of the applied voltage. The competition between the charge transport caused by the sloshing of ionic space charges and the applied voltage during phases I→II and III→IV helps explain why the net ionic current during these phases is smaller than that during phases II→III and IV→I, in which the sloshing of ionic space charges and applied voltage cooperate with each other.

### 3.2.3. Effects of Scan Rate and Pore Size on Dynamic Charge Storage

Figure 3-8a compares the cyclic voltammograms of a 0.78 nm-wide pore operating at different scan rates. As the scan rate increases, the current deviates more and more from that at the quasi-static charging/discharging condition. In particular, the charging current at moderate voltages (0.5-1.2 V) decreases sharply with increasing scan rate, while that at large voltages (>~1.5 V) decreases moderately. To quantify how the performance of the dynamic charge storage inside the pore is affected by the scan rate, the following are computed: the electrical energy needed to charge the pore during the forward scan  $E_{charging}$ , the energy delivered by the pore during the backward scan  $E_{discharging}$ , and the voltammetric charge  $Q_v$ :

$$E_{charging} = \int_0^{t_f} V(t) I(t) dt = \int_{\bar{q}(0)}^{\bar{q}(t_f)} V(\bar{q}) d\bar{q} \quad (3-2)$$

$$E_{discharging} = \int_{t_f}^{t_b} V(t) I(t) dt = \int_{\bar{q}(t_f)}^{\bar{q}(t_b)} V(\bar{q}) d\bar{q} \quad (3-3)$$

$$Q_v = \int_0^{t_f} I(t) dt = \int_{t_f}^{t_b} I(t) dt \quad (3-4)$$

where  $t = 0$  is the starting time of a full scan.  $t_f$  and  $t_b$  are the time when the forward and backward scan ends, respectively.  $V$ ,  $I$ , and  $\bar{q}$  are the voltage on the pore wall, the net ionic current in/out of the pore, and the average charge inside the pore. The energy efficiency of the charge

storage, also called the Watt-hour efficiency<sup>123</sup>, is computed using  $\eta_e = E_{discharging}/E_{charging}$ . The charge efficiency is computed using  $\eta_{dyn} = Q_v/Q_{equ}$ , where  $Q_{equ}$  is the amount of charge stored inside the pore under quasi-static charging conditions. Note that  $\eta_{dyn}$  is different from the Amp-hour (or Coulomb) efficiency<sup>123</sup>, which is 100% due to the absence of stray currents in the simulations.

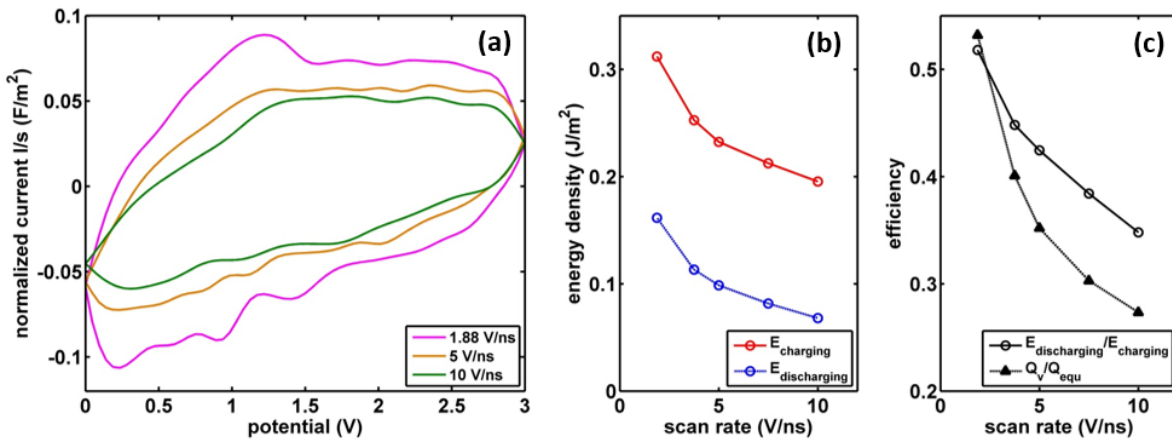


**Figure 3-8.** Effects of scan rate on the charging/discharging of a 0.78 nm pore. **(a)** Cyclic voltammograms of the pore operating at different scan rates. **(b)** Effects of scan rate on the energy needed for charging a 0.78 nm-wide pore and the energy released by the same pore during discharging. **(c)** Effects of scan rate on the charge and energy storage efficiency of a 0.78 nm-wide pore during cyclic charging and discharging.

Figure 3-8b shows that, as the scan rate increases, both the energy needed to charge the pore and the energy delivered by the pore during discharging decrease due to less charge being stored/released during the charging/discharging half cycle (Figure 3-8c). Figure 3-8c also shows that the overall energy efficiency of the charge storage/release cycle also decreases as the scan rate increases, which is consistent with the results shown in Figure 3-8a, i.e., at high scan rates, most charges are stored at high voltage (thus requiring more energy, cf. Equation 3-2) but released at low voltage (thus delivering less energy). Figure 3-8c further shows that the charge efficiency decreases with increasing scan rate. However, the pore retains  $\sim 30\%$  of its charge storage

capability when the scan rate increases from zero (quasi-static) to 10 V/ns. This indicates that, while the scan rates used in this study are far greater than those used in typical experimental studies, they are not too high for the nanoscopic systems considered here, which is akin to the fact that scan rates up to several V/s are experimentally used to characterize the charging dynamics in cavity micro-electrodes<sup>124</sup>.

The response of  $E_{charging}$ ,  $E_{discharging}$  and  $\eta_e$  to the scan rate shown above originates from the fact that, as the scan rate increases, the charging (discharging) current decreases, especially at low (high) voltages. This fact is consistent with the expectation that, as the scan rate increases, counterions (co-ions) have less time to be inserted into (removed from) the pore, which is already predicted by the classical TLM. Close inspection of the ion dynamics underlying the cyclic charging and discharging, however, shows that the response of the charge storage to the scan rate exhibits unique features that are not described by the classical TLM.

The classical TLM does not distinguish the role of counter/co-ions in charging/discharging as ion density does not explicitly appear in the model. Hence it cannot provide information on the relative contribution of counter/co-ions to dynamic charge storage. On the other hand, these simulations indicate that counterions dominate the dynamic charge storage, especially at high scan rates. Figure 3-9 shows how the average densities of counterions and co-ions inside a pore vary as the pore becomes charged. The ion densities and net ionic charge are offset by their values at the VMC because the net charge inside the pore is not zero at the beginning of the forward scan (*cf.* Figures. 3-5a, b). Under quasi-static conditions, counterion insertion and co-ion removal contribute similarly to charge storage until the pore becomes moderately charged ( $\sim 1.2 \text{ e/nm}^2$ ); further charging is contributed almost solely by the removal of co-ions until they are completely removed, after which counterion insertion dominates charging (not shown). These different roles of

counter/co-ions in charge storage are thermodynamic in origin and their mechanisms have been previously clarified<sup>70, 125</sup>. However, at finite scan rates, the contributions of counter/co-ions to charge storage changes greatly. At a scan rate of 1.88 V/ns, before  $q - q_{VMC}$  reaches  $\sim 1.2$  e/nm<sup>2</sup>, the contribution of counterion insertion and co-ion removal to net charge storage deviate moderately from those under quasi-static conditions. Specifically, counterions contribute more

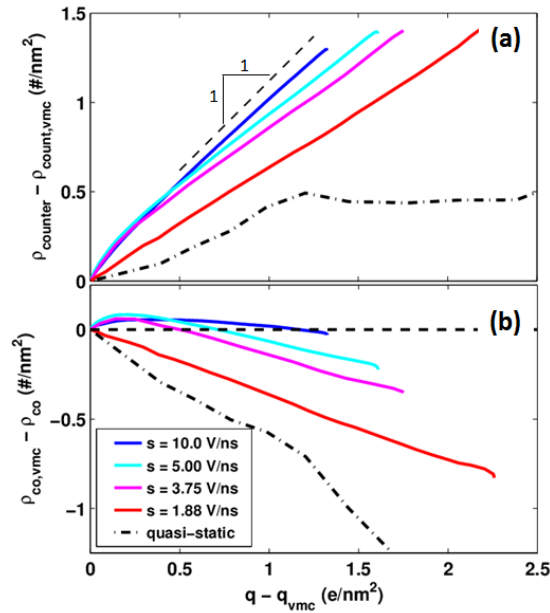


**Figure 3-9.** Variation of ion density during charging of a 0.78 nm-pore. (a) The average counterion densities. (b) The average co-ion densities. The ion densities ( $\rho_{count/co}$ ) and net ionic charge ( $q$ ) are offset by their values at the voltage of minimal charge (VMC). In panel a, the thin dashed line corresponds to the situation in which charging is contributed solely by insertion of counterions.

while co-ions contribute less to the dynamic charge storage. As charging proceeds further, the relative contribution of counter/co-ions does not change greatly. This latter behavior, however, differs from that in the quasi-static charging, in which charging from  $q - q_{PMC} = 1.2$  to  $2.2$  e/nm<sup>2</sup> is almost solely due to co-ion removal. As the scan rate further increases, the contribution of co-ions to the charge storage is further reduced, e.g., at scan rates faster than 3.75 V/ns, co-ions are even inserted into the pore during the early stage of charging (Figure 3-9b), thus contributing

negatively to net charge storage. As a result, charge storage is increasingly achieved through counterion insertion. Indeed, at scan rate of 10 V/ns, charge storage is achieved almost exclusively through the insertion of counterions (cf. Figure 3-9a).

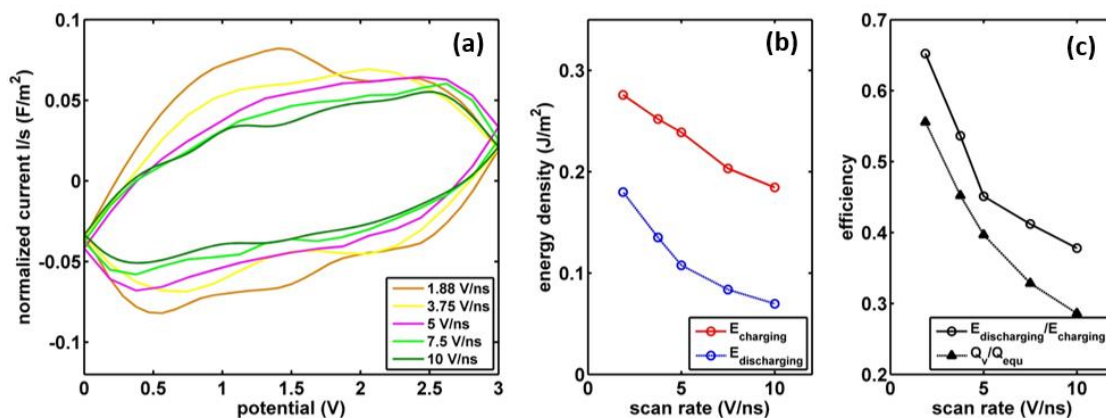


**Figure 3-10.** Effects of scan rate on the charging/discharging of a 0.91 nm pore. (a) Cyclic voltammograms of the pore operating at different scan rates. (b) Effects of scan rate on the energy needed for charging a 0.91 nm-wide pore and the energy released by the same pore during discharging. (c) Effects of scan rate on the charge and energy storage efficiency of a 0.91 nm-wide pore during cyclic charging and discharging.

The ion dynamics exposed above resemble those observed in recent experiments. In particular, the dominance of charging by counterions is similar to that reported in the pioneering EQCM studies by Levi *et al.* and Tsai *et al.*<sup>85, 88</sup> Both research groups found that under certain conditions, the charging of the pore is contributed almost solely by the insertion of counterions (termed perm-selectiveness). The perm-selectiveness observed by Levi *et al.*<sup>85</sup> seems to be thermodynamic in nature as charging was found to be independent of the scan rate when the perm-selectiveness was observed. The perm-selectiveness observed by Tsai *et al.*<sup>88</sup>, however, could have different origins. Specifically, for CDC electrodes (pore size: 1.0 nm) in contact with EMI-TFSI electrolytes, charge storage in the negative polarization (when EMI<sup>+</sup> ion is the counterion) and in part of the positive polarization (when TFSI<sup>-</sup> ion is the counterion) was found to be contributed solely by the insertion of counterions at a scan rate of 10 mV/s. Prior simulations of the charge

storage in porous carbons with similar pore size and electrolytes show that, at equilibrium, the contributions of counterion insertion and co-ion removal to the net charge storage are quite similar<sup>70-71</sup>. Therefore, the perm-selectiveness observed in Tsai *et al.*'s study likely has dynamic origins similar to what was observed and discussed in detail above. Note that while a scan rate of 10 mV/s is relatively small, charging at this rate can still show dynamic effects. In fact, even a scan rate of 0.5 mV/s there can be incurrence of significant dynamic effects for some systems<sup>86</sup>.

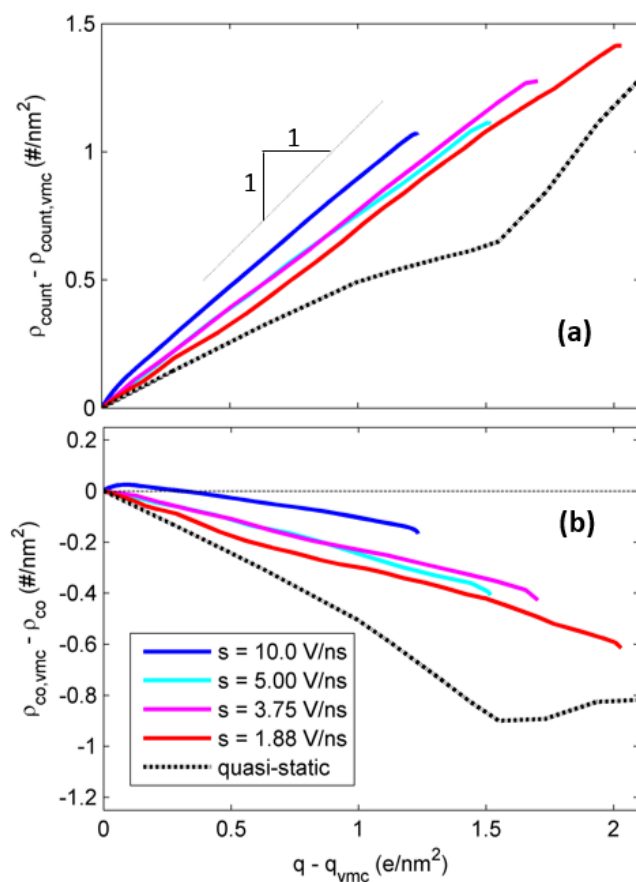


**Figure 3-11.** Variation of ion density during charging of a 0.91 nm-pore. (a) The average counterion densities. (b) The average co-ion densities. The ion densities ( $\rho_{\text{count/co}}$ ) and net ionic charge ( $q$ ) are offset by their values at the voltage of minimal charge (VMC). In panel a, the thin dashed line corresponds to the situation in which charging is contributed solely by insertion of counterions.

The effect of pore size on charging and discharging was also examined. The result for a 0.91 nm-wide pore exhibits similar features as for the 0.78 nm-wide pore discussed above. As shown in Figure 3-6, Figure 3-10 and Figure 3-11, the SZV of the pore is characterized by a deficiency of co-ions compared to the PZC state. In these cases, the dynamics of counterions follow more closely the evolution of the applied voltage while co-ions lag behind; co-ions are inserted into the pore concurrently with counterions during the initial phase of the forward scan with high rates while counterions dominate the charging of the pore at large scan rates. However, because the transport of ions is less sluggish than in the 0.78 nm-wide pore (cf. Equation 3-1), the charging/discharging of this pore is more efficient (Figure 3-10c). The response of counterions and co-ions to the applied voltage is less disparate compared to that in the 0.78 nm-wide pores: the concurrent insertion of counter-/co-ions terminates at smaller voltages compared to that in narrower pores. While counterions still dominate the charging, co-ions contribute notably to charging even at the highest scan rate examined here (cf. Figure 3-11).

### **3.3. Conclusions**

In summary, the cyclic charging and discharging of supercapacitors based on sub-nanometer pores and RTILs by using MD simulations have been studied. These simulations allowed us to probe the dynamic charge storage at the single-pore level both spatially and temporally, which is extremely difficult, if possible at all, to access experimentally. It was found that the cyclic charging and discharging of a nanopore are governed by the external field-driven ion transport and the sloshing dynamics of ions inside the pore. These two processes compete with (or facilitate) each other during the beginning (late) phase of the forward and the backward scan, which leads to the asymmetric shape of the cyclic voltammogram.

The dynamic charge storage in subnanometer pores is dominated by counterions, especially at high scan rates and in narrower pores. Such a phenomenon differs greatly from the charge storage under equilibrium conditions. The predominant contribution of counterions to the charge storage observed here, termed perm-selective charging by prior researchers, is caused by the stronger electrical migration flux of counterions during charging, which in turn is caused by the relative abundance of counterions over co-ions inside the pore. As the pore becomes wider, the relative abundance of counterions over co-ions weakens, and therefore the co-ions contribute more to charge storage, albeit still at a lesser degree than counterions.

These simulations revealed that, during cyclic charging/discharging, nanopore systems are driven to far-from-equilibrium states. Indeed, the internal state of the nanopore (in particular the total ion density) not only deviates from that under quasi-static charging/discharging conditions but also varies greatly as the scan rate changes. Since these phenomena affect the energy and charge storage efficiency of the cyclic charging/discharging of nanopores, they should be considered when developing improved theories for charging/discharging of supercapacitors.

In the present coarse-grained simulations, simplistic models are used for ions and pore walls, and the specific interactions between them are neglected. In practice, the specificities of ions and ion-wall interactions can affect the dynamics of charge storage in nanopores, e.g., the specific adsorption of ions in pores can greatly affect their transport properties and thus the dynamic charge dynamics. Clarifying the effects of these specificities requires the charge storage to be simultaneously resolved at quantum-, molecular-, and pore-scales in simulations. Such multiscale simulations represent a grand challenge in materials modeling and cannot be achieved by brute-force coupling of the simulations at these scales. However, by developing fundamental understanding of the generic features determined by collective interactions between the RTIL ions

in a nanopore, screened by the electronic polarizability of the pore, this work will lay the basis for such multiscale simulations.

## CHAPTER 4

### Molecular Mechanics of PBDT Ion Gels

The recently fabricated PBDT ion gels (also termed molecular ionic composites or MICs) feature polyanions immersed in RTILs. They show promising properties such as high ionic conductivity, widely tunable modulus, and great thermal stability. In particular, when the PBDT mass fraction is high, the elastic modulus of the ion gel could reach several GPa, much higher than most existing ion gels. The rational design of the ion gels requires a fundamental understanding of molecular mechanisms behind their superior properties. Here the mechanical property of the ion gel consisting of PBDT polyanions and [C<sub>2</sub>mim][TfO] RTILs is studied using molecular simulations. In general, the mechanical strength of the ion gels originates from the strong ion-ion correlation inside them. The highly aligned PBDT polyanions in the ion gels can carry most of the loads in polyanions' axial direction, thus leading to high elastic modulus in this direction. Under transverse loading, the interference of the ionic space charges between polyanions (consequently the polyanion-polyanion interactions) becomes less favorable and resists transverse strain strongly. Such a strong resistance to mechanical strain, along with the massive amount of polyanions per unit volume in the ion gels endows the material with high elastic modulus in the transverse direction. Furthermore, the shear deformation has a smaller effect on the interference of ionic space charge between polyanions (thus the rod-rod interactions), which is also consistent with the relatively low shear modulus found in simulations and experiments.

## 4.1. Models, Simulation System and Methods

The PBDT ion gels exhibit rich structure at the macro-, meso- and molecular scales. As shown in Figure 4-1a, at the macroscale, it is expected that individual liquid crystalline (LC) domains can form in the gel sample. Each subdomain has its own LC alignment, which may be responsible for anisotropic properties of the ion gels<sup>49</sup>. As shown in Figure 4-1b, inside each subdomain, the PBDT chains are highly aligned. While most PBDT chains are packed with rather uniform spacing, there can still be pockets of RTILs. Based on how the PBDT chains are organized with respect to each other, the meso-scale structure inside each subdomain can be further classified into three different regions, marked as A, B and C in Figure 4-1b. Region A is where all the aligned PBDT chains are from the same bundle, and an enlarged view of this region is shown in Figure 4-1c. Region B is where the PBDT chains' end meets. In region C, chains from different bundles are aligned with each other.

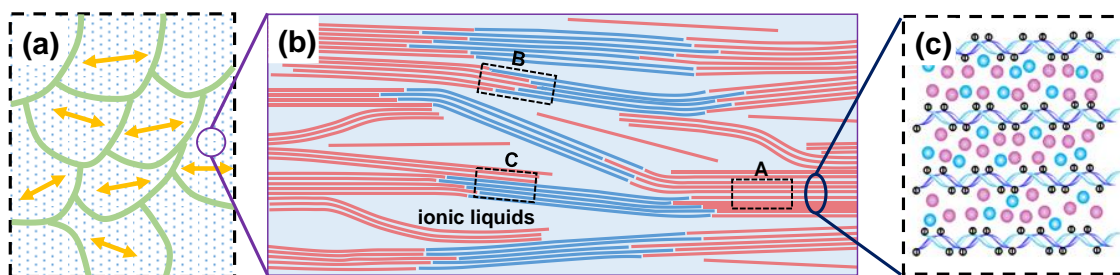


**Figure 4-1.** The structure of the PBDT ion gel. (a) A schematic of the macroscale structure of the gel with grain boundaries (denoted by the green curves). Each subdomain shows liquid crystalline (LC) alignment originating from the aligned PBDT chains. The arrows show the LC alignment of the subdomain. (b) A schematic of the structure of the gel inside one subdomain. The red/blue lines denote the PBDT chains. The blue background denotes the ions dispersed in the gel. Three different regions are marked. (c) A schematic of the locally highly aligned PBDT chains immersed in RTILs. The pink balls denote the C<sub>2</sub>mim cations, the blue balls denote the BF<sub>4</sub> anions and the small black balls denote the SO<sub>3</sub><sup>-</sup> groups of the PBDT chains. Figure in panel (c) is reproduced from Ref. 49.

Quantitative prediction of the mechanical and transport properties of the ion gels with the above structure requires multiscale simulations spanning molecular (angstrom-level) to continuum scales (a few to tens of micrometers). Given that research on this new class of ion gel is still at the earliest stage, these multiscale simulations are not yet possible. A reasonable roadmap toward understanding the mechanics of the ion gels is as follows. First, the mechanical properties of ion gels in representative mesoscale constituents of ion gels (e.g., regions A, B and C in Figure 4-1b) must be understood. Next, how the constituents interact with each other must be clarified. Finally, the interactions between subdomains shown in Figure 4-1a must be elucidated. To break ground for the fundamental research toward understanding the mechanical properties of PBDT ion gels, the mechanical properties of the region A in Figure 4-1b are studied because the mechanical moduli of this region largely set the upper bound of the mechanical moduli of ion gel samples.

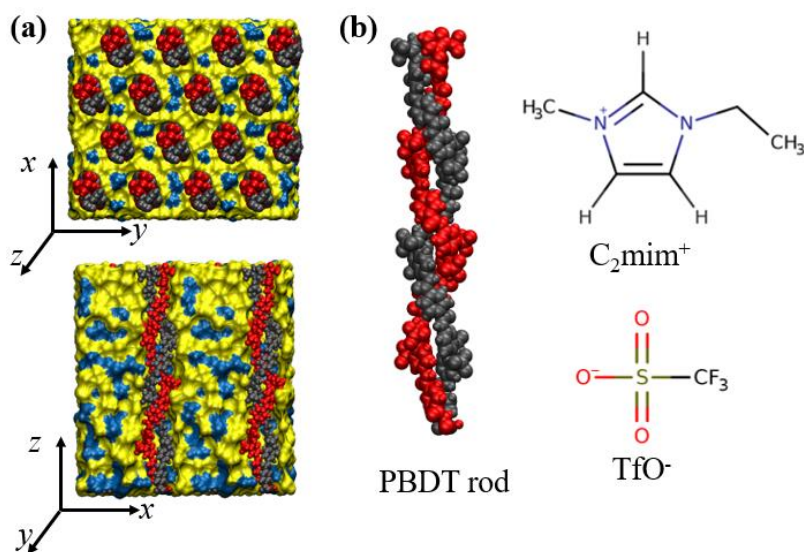


**Figure 4-2.** The molecular system used to study the mechanical properties of PBDT ion gels. (a) Top view and side view of the simulation system. The red and black chains represent the PBDT polyanions, the blue surface represent the anions and the yellow surface represent the cations. (b) The chemical structure of the PBDT rod, C<sub>2</sub>mim<sup>+</sup>, and TfO<sup>-</sup>. Each rod consists of two PBDT polyanions pre-assembled in a double-helix conformation with four chemical repeat units.

In this work, the mechanical property of the PBDT-[C<sub>2</sub>mim][TfO] ion gel is studied using MD simulations with full molecular models (see Figure 4-2). MD simulations were performed using the LAMMPS codes<sup>102</sup>. A relatively high PBDT mass fraction (30 wt%) was chosen to improve the statistics of the simulations. The ion gel system was pre-assembled, equilibrated then strained, and the corresponding stresses were recorded to calculate its mechanical properties.

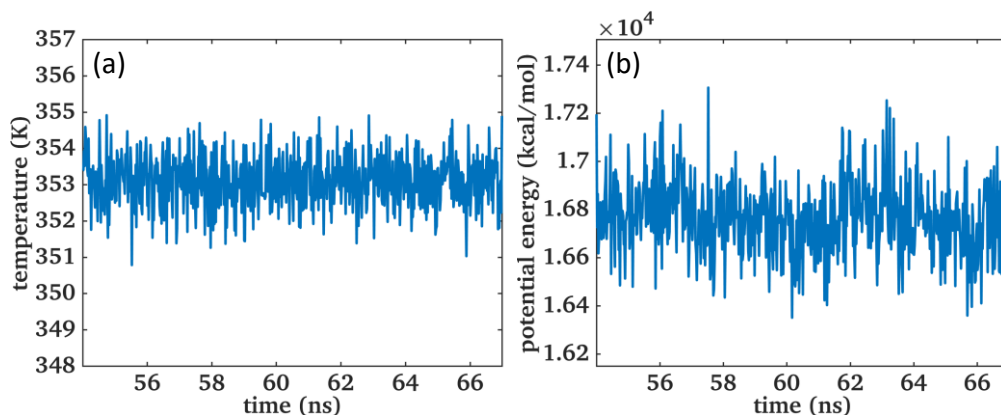


**Figure 4-3.** Temperature (a) and potential energy (b) of the system during the last stage of the NVT equilibration. The average temperature of the system is  $353 \pm 0.72$  K; the average potential energy of the system is  $16765 \pm 150$  kcal/mol.

The MD system was built with 16 PBDT rods immersed in the RTIL [C<sub>2</sub>mim][TfO]. As shown in Figure 4-2b, each rod is composed of two PBDT polyanions pre-assembled in a double-helix conformation as suggested by prior studies<sup>49</sup>. Initially the PBDT rods were perfectly arranged in a hexagonal lattice<sup>98</sup> in the *xy*-plane and aligned in the *z* direction. The simulation unit cell for the ion gel is assumed to be transversely isotropic with *z*-axis being the axis of symmetry. The cation/anion numbers are chosen such that the PBDT mass fraction is ~30% and the whole system is charge neutral. The simulation system is periodic in all three directions. The system was first equilibrated in the NPT ensemble for 50 ns, followed by a run in the NVT ensemble for 10 ns to generate the initial configuration for the simulations with mechanical deformation. The temperature and potential energy of the system during the NVT equilibration are shown in Figure

4-3. The temperature and potential energy profiles did not show observable drift, indicating the system has been equilibrated well. Using the center-of-mass position of each PBDT rods, the distance between adjacent rods was measured as  $\sim 1.69$  nm in the equilibrium state.

For transversely isotropic materials, only five independent elastic coefficients are required to define the elastic stiffness matrix:

$$\begin{bmatrix} \sigma_{11} = \sigma_{xx} \\ \sigma_{22} = \sigma_{yy} \\ \sigma_{33} = \sigma_{zz} \\ \sigma_{23} = \sigma_{yz} \\ \sigma_{13} = \sigma_{xz} \\ \sigma_{12} = \sigma_{xy} \end{bmatrix} = \begin{bmatrix} C_{11} & C_{12} & C_{13} & 0 & 0 & 0 \\ C_{12} & C_{11} & C_{13} & 0 & 0 & 0 \\ C_{13} & C_{13} & C_{33} & 0 & 0 & 0 \\ 0 & 0 & 0 & C_{44} & 0 & 0 \\ 0 & 0 & 0 & 0 & C_{44} & 0 \\ 0 & 0 & 0 & 0 & 0 & C_{11} - C_{12} \end{bmatrix} \begin{bmatrix} \epsilon_{11} = \epsilon_{xx} \\ \epsilon_{22} = \epsilon_{yy} \\ \epsilon_{33} = \epsilon_{zz} \\ \epsilon_{23} = \epsilon_{yz} \\ \epsilon_{13} = \epsilon_{xz} \\ \epsilon_{12} = \epsilon_{xy} \end{bmatrix} \quad (4-1)$$

where  $C_{ij}$  is the elastic constant of the material, and  $\sigma_{ij}$  and  $\epsilon_{ij}$  are the stress and strain components in the direction. In order to evaluate the five independent elastic constants  $C_{ij}$  of an ion gel, three sets of simulations were carried out with different sets of boundary conditions.

**Table 4-1.** The displacement applied at the boundary of the simulation system. The subscripts 1, 2, 3 represent  $x$ ,  $y$ ,  $z$  directions respectively, where  $z$  is the longitudinal direction.

Applied strains	Applied displacements
$\epsilon_{11} = e$	$u_1 = ex_1$
$\epsilon_{33} = e$	$u_3 = ex_3$
$\epsilon_{23} = e$	$u_2 = \frac{e}{2}x_3, u_3 = \frac{e}{2}x_2$

Table 4-1 summarized the displacement applied at the boundary of the simulation system. The strain was applied to system by uniformly deforming or shearing the simulation cell in certain directions and re-scaling the coordination of the atoms in the new simulation cell. The simulation system was equilibrated for 20 ns, then the stress tensor was averaged over another 20 ns. The stress of the system is defined in the form of virial stress<sup>126</sup> and computed by the average of the local stress over all the atoms in the MD system,

$$S_{ab} = \frac{1}{N} \sum_{i=1}^N \frac{1}{V_i} [m_i v_a^i v_b^i + \frac{1}{2} \sum_{j \neq i} F_{ij} \frac{r_{ij,a} r_{ij,b}}{r_{ij}}] \quad (4-2)$$

where  $m_i$  is the mass of atom  $i$ ,  $v_a^i$  and  $v_b^i$  are the velocities of atom  $i$  in the axial a and b directions,  $N$  is the total number of atoms in the system,  $r_{ij}$  is the distance between two atoms,  $r_{ij,a}$  is the component of the vector from atom  $i$  to  $j$ ,  $V_i$  is the volume of atom  $i$  ( $\sum V_i = V$  is the system volume), and  $F_{ij}$  is the force between atom  $i$  and atom  $j$ , including the intermolecular forces and intramolecular forces.

The modulus of the material can then be calculated from the elastic constants using the following equations,

$$E_3 = C_{33} - \frac{2C_{13}C_{13}}{C_{11} + C_{12}} \quad (4-3)$$

$$E_1 = E_2 = \frac{(C_{11} - C_{12})(C_{11}C_{33} + C_{12}C_{33} - 2C_{13}C_{13})}{C_{11}C_{33} - C_{13}C_{13}} \quad (4-4)$$

$$G_{12} = \frac{1}{2} (C_{11} - C_{12}) \quad (4-5)$$

$$G_{23} = G_{13} = \frac{1}{2} C_{44} \quad (4-6)$$

where  $E_3$  is the elastic modulus of the material in the  $z$ -direction (along the rod),  $E_1 = E_2$  are the elastic modulus of the material in the transverse direction,  $G_{12}$ ,  $G_{23}$  and  $G_{13}$  are the shear modulus of the material in the respective planes.

It should be noted that in order to apply the shear strain  $\epsilon_{23}$ , a coordinate transformation is required due to the way the simulation box edge vectors are defined in LAMMPS. As shown in the Figure 4-4, after the shear strain  $\epsilon_{23}$  is applied to the simulation box, the new edge vectors

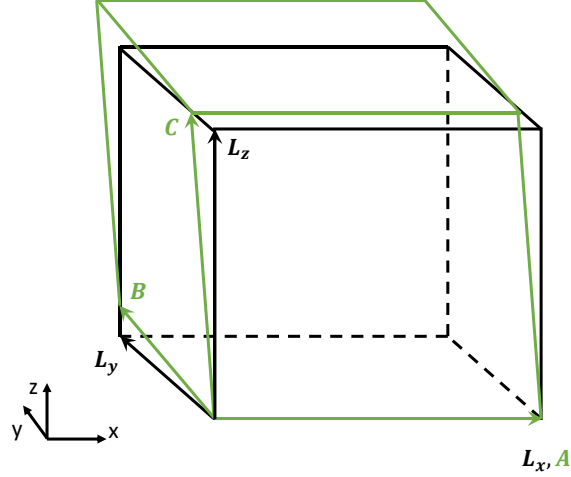


**Figure 4-4.** The simulation box before and after the shear deformation. The black lines represent the original simulation box with edge vectors  $L_x$ ,  $L_y$  and  $L_z$ . The green line represent the simulation box after the shear strain  $\epsilon_{23}$  is applied, and the edge vectors are  $A$ ,  $B$  and  $C$  respectively.

should be  $A = [L_x, 0, 0]$ ,  $B = [0, L_y, \frac{e}{2}L_y]$  and  $C = [0, \frac{e}{2}L_z, L_z]$ , where  $L_x$ ,  $L_y$  and  $L_z$  are the edge length of the original simulation box. However, in LAMMPS the triclinic simulation box edge vectors are defined as  $\mathbf{a} = [a_x = xhi - xlo, 0, 0]$ ,  $\mathbf{b} = [b_x = xy, b_y = yhi - ylo, 0]$ , and  $\mathbf{c} = [c_x = xz, c_y = yz, c_z = zhi - zlo]$ , which means  $\mathbf{a}$  must lie on the positive  $x$  axis,  $\mathbf{b}$  must lie in the  $xy$  plane with positive  $y$  component, and  $\mathbf{c}$  may have any orientation with positive  $z$  component. Using the following equations, the edge vectors  $A$ ,  $B$  and  $C$  can be transferred to  $\mathbf{a}$ ,  $\mathbf{b}$  and  $\mathbf{c}$ ,

$$a_x = A \quad (4-7)$$

$$b_x = \mathbf{B} \cdot \mathbf{A} \quad (4-8)$$

$$b_y = |\mathbf{A} \times \mathbf{B}| = \sqrt{B^2 - b_x^2} \quad (4-9)$$

$$c_x = \mathbf{C} \cdot \mathbf{A} \quad (4-10)$$

$$c_y = \mathbf{C} \cdot (\widehat{\mathbf{A} \times \mathbf{B}}) \times \mathbf{A} = \frac{\mathbf{B} \cdot \mathbf{C} - b_x c_x}{b_y} \quad (4-11)$$

$$c_z = |\mathbf{C} \cdot (\widehat{\mathbf{A} \times \mathbf{B}})| = \sqrt{C^2 - c_x^2 - c_y^2} \quad (4-12)$$

where  $A$ ,  $B$  and  $C$  are the length of the respective vectors, the symbol  $(\widehat{\phantom{x}})$  indicates the corresponding unit vector.

Following previous work<sup>94</sup>, the  $C_{2mim}^+$  and  $TfO^-$  ions were modeled using united-atom force fields<sup>127</sup>. The force field parameters for the PBDT polyanions were generated using the Swissparam server<sup>128</sup>. The PBDT polyanions were modeled as periodic molecules with four repeat units, which have effectively infinite length in the axial direction considering its periodic images. According to the previous work<sup>49</sup>, each PBDT rod is composed of two PBDT polyanions in a double helix structure. However, it is difficult for two infinitely long PBDT polyanions chains to intertwine and form a double helix structure in MD simulation. Therefore, the periodic PBDT polyanions are pre-assembled into a double helix form. As shown in Figure 4-5a, the non-periodic PBDT molecules was first built with four repeat units, then two PBDT molecules were placed side-by-side in water (with sodium ions so that the system is charge neutral). After ~30 nanoseconds, it was observed that the two non-periodic PBDT molecules would intertwine with each other and form a double helix structure as shown in Figure 4-5b. The system was further equilibrated for 90 ns to make sure the structure is stable. At this point, a stable double helix structure of the non-periodic PBDT molecules was picked. The atoms of periodic PBDT molecules were then mapped to this double helix structure to obtain a double helix structure composed of two periodic PBDT molecules intertwined with each other. To ensure that the structure is stable, the double helix structure is further relaxed in water for 10 nanoseconds. The stable double helix structure of periodic PBDT polyanions is then used to build the simulation system shown in Figure 4-2a with RTILs.

The system temperature was maintained at 353 K using a Nosé-Hoover thermostat. The non-electrostatic interactions were computed via direct summation with a cut-off length of 1.2 nm. The electrostatic interactions were computed using the particle-particle particle-mesh (PPPM) method with a real-space cutoff length of 1.2 nm. The stresses were recorded every 20 ps. Each simulation was repeated three times with different initial configurations to obtain reliable statistics.

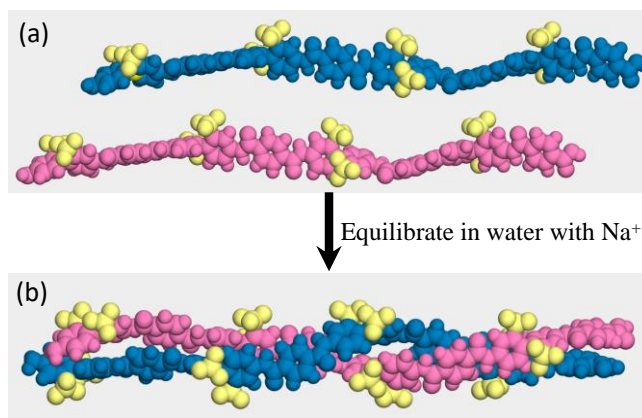


**Figure 4-5.** Formation of the double helix structure using non-periodic PBDT polyanions. (a) Two PBDT polyanions are packed side-to-side in water with Na<sup>+</sup> ions. (b) After ~30 nanoseconds, two polyanions chains intertwine with each other and form a double helix structure. The pink and blue balls denote the backbone of the PBDT polyanion chains of two molecules respectively, the yellow balls denote the SO<sub>3</sub> groups of the PBDT molecules, the grey background denotes the water. Na<sup>+</sup> ions and water molecules are not shown for clarity.

## 4.2. Results and discussion

Some tests were first performed to make sure the model ion gel built in Figure 4-2 behaves as viscoelastic material with finite elastic component at low frequency rather than some nanorods immersed in liquids, i.e. pencils immersed in water. In the first scenario, when strain is imposed to the system in the  $x$  or  $y$  direction while the pressure is maintained constant in the other directions, the stress in the deformed directions should not decay to zero in the long time limit. On the other

hand, if the modelled system behaves like pencils-in-water box, the stress in the deformed direction will decay to zero gradually.

To perform the above test, a 2% strain was imposed to the equilibrated system in the  $x$  direction while the pressure in  $y$  and  $z$  directions were maintained constant. As shown in Figure 4-6, after 10 ns, the stress in the  $x$  direction does not vanish, which means the system built in Figure 4-2 has passed the pencil-in-water box test. It should be noted that a system with 20% PBDT mass fraction was also built and tested, but that system failed this test.

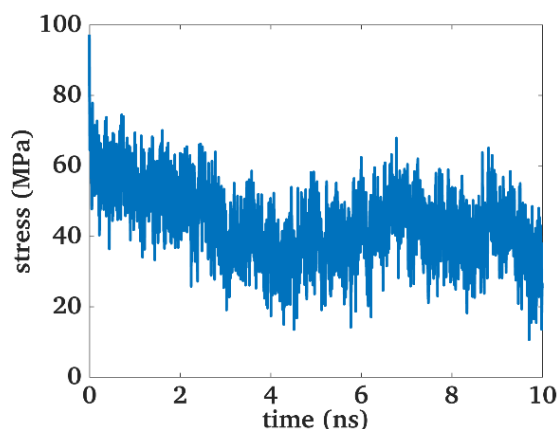


**Figure 4-6.** The pencil-in-water box test. A 2% strain is imposed to the model ion gel in the  $x$  direction while the pressure in  $y$  and  $z$  directions are maintained at 1 atm. After 10 ns, the stress in the  $x$  direction does not vanish, suggesting that the system is behaving as a solid.

The equilibrated system was then strained as in Table 4-1 to calculate the elastic constants of the model ion gel. Table 4-2 summarizes the stiffness constants and the modulus of the ion gel calculated from the simulations. The elastic modulus of the ion gel in the direction along the PBDT rod ( $E_{\parallel}$ ) is very high. This is expected since the highly aligned PBDT polyanion bundle, which is periodic in the longitudinal direction, can carry most of the loads in this direction without much deformation.

The modulus in the transverse direction ( $E_{\perp}$ ) is smaller than  $E_{\parallel}$ , but still much larger than what was found in gel-like materials<sup>96-97</sup>. The relatively high modulus in the transverse direction mainly comes from the strong electrostatic interactions between the PBDT nanorods mediated by the RTILs. As indicated by prior work<sup>94</sup>, the ions around charged nanorods exhibit long-range ordering and extensive electrostatic networks are formed within ion gels. The ionic charge distribution in the equilibrium state should correspond to the lowest free energy of the system, or the most favorable interactions between the polyanion nanorods. After a transverse strain is imposed on the ion gel, the spacing between the charged nanorods is modified and the ionic space charge distribution between the PBDT nanorods changes. The electrostatic interactions between the PBDT nanorods in such a new configuration are less favorable than in the initial configuration. If the change of the electrostatic interactions between the nanorods is large for a small change of the PBDT nanorod configuration (and the distribution of the ions between the nanorods), a large amount of energy can be stored when the ion gel is only deformed weakly, which is manifested as a high modulus of the ion gel in the transverse direction. Following this idea, the ion distribution in the interstitial space between PBDT nanorods and its impact on the rod-rod interactions will be examined next.

**Table 4-2.** Stiffness constants and modulus of the model ion gel studied in this work. The unit of the listed numbers is MPa. The subscripts 1, 2, 3 represent  $x$ ,  $y$ ,  $z$  directions respectively, where  $z$  is the longitudinal direction.

$C_{11}$	$C_{12}$	$C_{13}$	$C_{33}$	$C_{44}$
3241	2801	3113	8775	262
$C_{66}$	$E_{\perp}$ ( $E_{\perp}$ )	$E_{\parallel}$ ( $E_{\parallel}$ )	$G_{13}$	$G_{12}$
440	789	5566	131	220

Figure 4-7 shows the ionic charge density distribution in the interstitial space between the PBDT polyanions in the un-deformed the model ion gel. Even though the net charge of the PBDT rod is negative, some negative ionic charge is observed close to the rod surface. This is caused by two reasons. First, the sulfonate groups carrying the negative surface charge have finite size and some of their atoms are located at positions relatively far away from the rod's axis. Second, the PBDT rods are not strictly straight in these simulations. A ring of positive ionic charge is observed around the negative charges in the center. Higher positive charge is observed at certain positions (bright yellow) on the ring due to the presence of the sulfonate groups near these positions. In the middle of three PBDT rods, there is a triangular pocket mostly filled with negative charge.

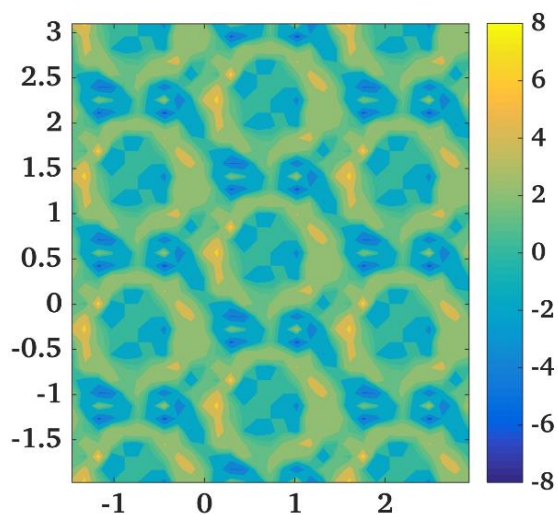


**Figure 4-7.** Ion charge density distribution in the interstitial space between the PBDT polyanions in an un-deformed model ion gel. PBDT rods are fixed into a hexagonal lattice in this simulation, and the rod-rod spacing is 1.69 nm. The ion density is color-coded, and the unit of the color bar is  $\text{nm}^{-3}$ . The ionic charge distributions around each rod in the simulation were averaged to improve the statistics.

In the un-deformed state, the ionic charge distribution shown above should lead to the lowest free energy for the rod-rod interactions. However, it is difficult to correlate such interactions with the ionic charge distribution directly. Nevertheless, it is possible to qualitative correlate the ionic charge distribution with the rod-rod interactions by leveraging the insight from prior studies.

Zhou *et al.*<sup>95</sup> studied the interaction between two charged nanorods immersed in RTILs. They correlated the rod-rod interaction energy change with the space charge interference around different rods, i.e. a constructive (destructive) interference leads to higher (lower) interaction energy, and such an interference of the ionic space charge can be predicted by a simple superposition of the ion charge density near a single charged nanorod. It should be noted that, in their work, there are only two nanorods in the system and each nanorod is essentially smooth cylinders. Therefore, whether the correlations between the interference of ionic space charge and rod-rod interactions established in their study is applicable to the current system (fully resolved PBDT polyanions arranged in a hexagonal lattice) is not obvious and must be established first.

To this end, the interactions between *two* PBDT nanorods immersed in bulk RTILs are first studied. The free energy for the rod-rod interaction in a 2-rod system was computed using the following equation,

$$E(D) = - \int_{D_0}^D f(x) dx \quad (4-13)$$

where  $f(x)$  is the force at a rod-rod separation of  $x$ ,  $D_0 = 3$  nm is the largest rod-rod separation explored in the simulations, and the free energy at rod-rod separation of  $D_0$  is taken as zero. Figure 4-8a shows the free energy between two PBDT rods as a function of the distance between them. A minimum (maximum) free energy is observed at  $\sim 1.35$  nm ( $\sim 1.65$  nm), and the energy barrier is  $\sim 4.3 k_B T/\text{nm}$ . Such a large energy barrier can help to stabilize the PBDT rods in the RTILs. In real ion gels, there are enormous number of PBDT nanorods in a unit volume, and the energy cost for changing the rod-rod spacing to either smaller or larger values compared to the equilibrium separation can be large.

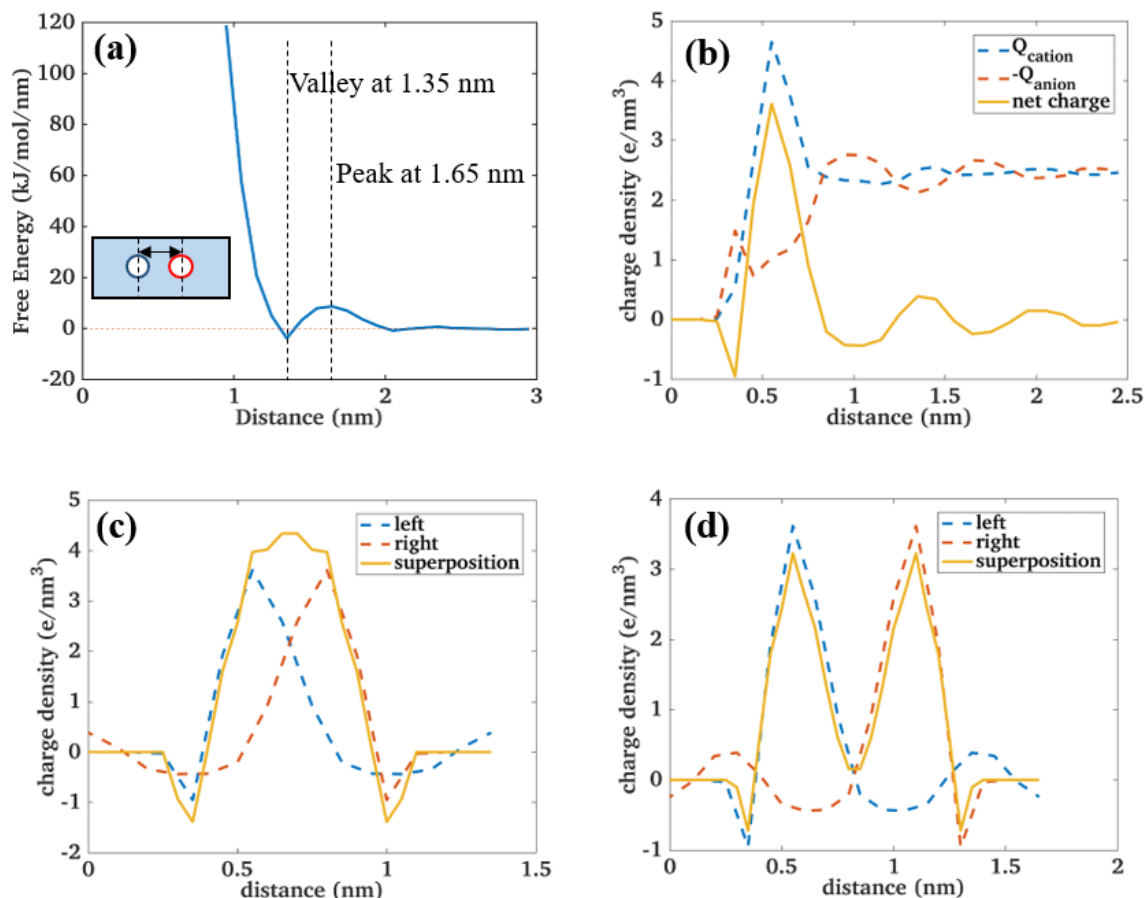


**Figure 4-8.** The interference of the ionic space charge between two PBDT rods and its correlation with the rod-rod interactions. (a) Interaction energy between two PBDT polyanions immersed in a bulk RTIL as a function of the rod-rod distance. The inset shows a sketch of the system used to calculate the free energy. (b) Charge density profile around an isolated rod as a function of the distance from the axis of the rod. (c-d) The interference of the ionic charge between two PBDT rods positioned at the minimum (c) and maxima (d) of the free energy vs. rod separation curve. The charge density profiles along the rod-rod centerline in (c) and (d) are calculated by the superposition of the charge density profile around an isolated rod.

It is difficult to calculate the interference of the ionic space charge between two PBDT rods directly as the rod is inhomogeneous. Such a calculation will require averaging ionic space charge under all different arrangements of the two PBDT rods. Nevertheless, as indicated by the previous work<sup>95</sup>, the simple superposition of the charge density profile around an isolated rod can predict the charge distribution between two rods. Figure 4-8b shows the ionic charge density profile

around an isolated PBDT rod. Similar to the 2-dimensional ionic charge density distribution shown in Figure 4-7, a small negative charge valley can also be observed very close to the center of the rod. Figure 4-8c shows that at a rod-rod distance of 1.35 nm, where the free energy is minimal, the interference of the space charge from the opposing rod is constructive, i.e. charge peak (valley) associated with one rod is reinforced by the charge peak (valley) of the other rod. On the other hand, Figure 4-8d shows that at a rod-rod distance of 1.65 nm where the free energy is maximal, and the interference of the space charge from the opposing rod is destructive, i.e. charge peak (valley) associated with one rod is cancelled by the charge peak (valley) of the other rod. These results confirm that, the interaction between two PBDT rods can also be reasonably deduced from the superposition of the space charge distribution around an isolated rod. The constructive (destructive) interference of the space charge would lead to the decrease (increase) of the free energy for the rod-rod interaction.

With insights from the 2-rod system, the relationship between the space charge density profile and the free energy of rod-rod interaction in the model ion gel can now be explored. The ionic space charge density in the interstitial space between the PBDT nanorods is computed using the superposition the ionic charge density near an isolated rod. Assuming that the PBDT rods are arranged in a perfect hexagonal lattice with a rod-rod spacing corresponding to the equilibrium rod-rod spacing, the computed space charge density distribution is shown in Figure 4-9a. Each PBDT rod is surrounded by a ring of positive ionic charge, and a triangular pocket filled with negative charge is observed in the gap formed by three neighboring rods. Overall, the charge density distribution calculated from the superposition in Figure 4-9a exhibits very similar pattern with the actual charge density distribution shown in Figure 4-7. As marked in the panel (a) and (b) in Figure 4-9, observation of the 2-D charge distribution suggests two typical regions with different

charge interference patterns in the interstitial space between the PBDT rods: the triangular region in the middle of three rods and the elliptical region along the centerline of two rods. These two regions are examined in details below.

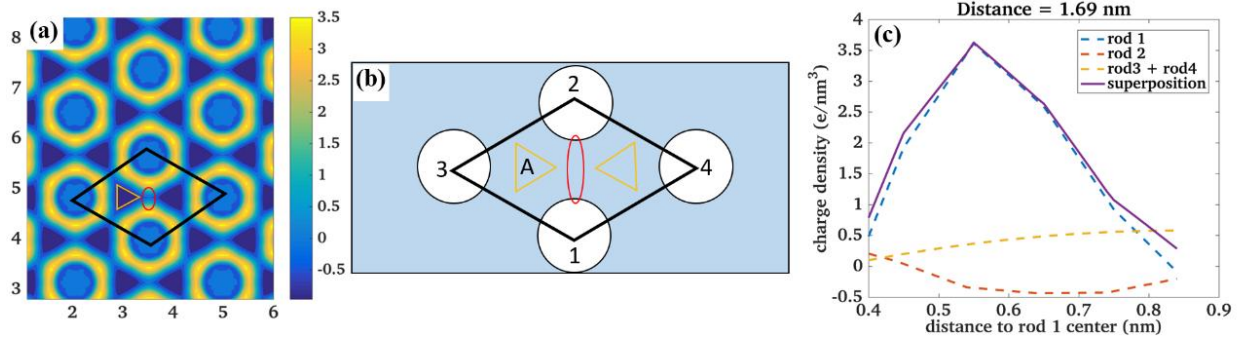


**Figure 4-9.** Charge interference in the PBDT ion gel. (a) 2-D ion charge density distribution with 1.69 nm rod-rod distance calculated from superposition. (b) Sketch showing two typical regions among the PBDT polyanion lattices with different charge interference pattern. (c) Charge interference along the centerline of rod 1 and rod 2 (marked in the sketch (b)) as a function of the distance to rod 1.

The distance from the center of the triangular region to the center of the nearby rods is  $\sim 0.98$  nm as the average rod-rod distance is  $\sim 1.69$  nm. Such a distance correlates to the position of a negative valley in the ionic charge distribution around an isolated rod in Figure 4-8b. This indicates that, in the triangular region where the distance to the nearby rods is around 0.98 nm, the space charge associated with each rod would be negative. As a result, the interference of the space charge in this region (e.g. the triangular region A in Figure 4-8b) from all three nearby rods (e.g. rods 1, 2 and 3 in Figure 4-8b) is constructive.

The situation in the elliptical regions is much more complicated. The interference of the space charge associated with all the four rods around it (e.g. rods 1, 2, 3 and 4 in Figure 4-8b) need to be considered. Figure 4-9c shows the charge interference in the lower half of the elliptical region along the centerline of rod 1 and rod 2 as a function of the distance to rod 1. Since the rod-rod distance in the current system is  $\sim 1.69$  nm, the interference of the space charge from rod 1 and rod

2 will be destructive, i.e. the charge peak (valley) associated with rod 1 is being canceled by the charge valley (peak) of rod 2. However, this destructive interference is cancelled by space charge associated with the other two nearby rods (i.e. rod 3 and rod 4). The situation is similar in the higher half of the elliptical region along the centerline of the rod 1 and rod 2: the negative space charge associated with rod 1 will be cancelled by the positive space charge associated with rod 3 and rod 4. Overall, in the elliptical region, the charge interference is weak due to cancellation between the constructive and destructive interference of charge around the four different rods near this region.

Based on the relationship between the interference of ionic space charges and the interaction between two charged nanorods, the constructive charge interference *in the triangular region* in Figure 4-9 tends to lead to a lower free energy for the rod-rod interactions. When the material is strained in the transverse direction, this triangle region would deform, and the distance from the region to the nearby rods will no longer be similar or around the negative charge valley in Figure 4-8b. As a result, the space charge associated with the nearby rods could change from negative to positive, the charge interference can change from constructive to destructive, and the accompanying rod-rod interaction energy increases. The situation *in the elliptical region* in Figure 4-9 is quite different as the charge interference in this region is rather weak. Regardless of whether the ion gel is in the equilibrium state or strained state, the weak charge interference in this elliptical region would only be slightly affected due to the cancellation effects outlined above. Therefore, the variation of the interference of ionic space charge in this region induced by the deformation of ion gel has smaller effect on the rod-rod interactions.

Overall, deforming the ion gel worsens the interference of ionic space charge in the gel (especially in the triangular region) and increases the rod-rod interaction energy. Although the

increase of the interaction energy between neighboring rods can be small, the overall increase of the system's free energy can be significant given the large number of PBDT nanorods in unit volume. This helps explain the very large modulus of the ion gels in the transverse direction, although no chemical bonds are present in these gels.

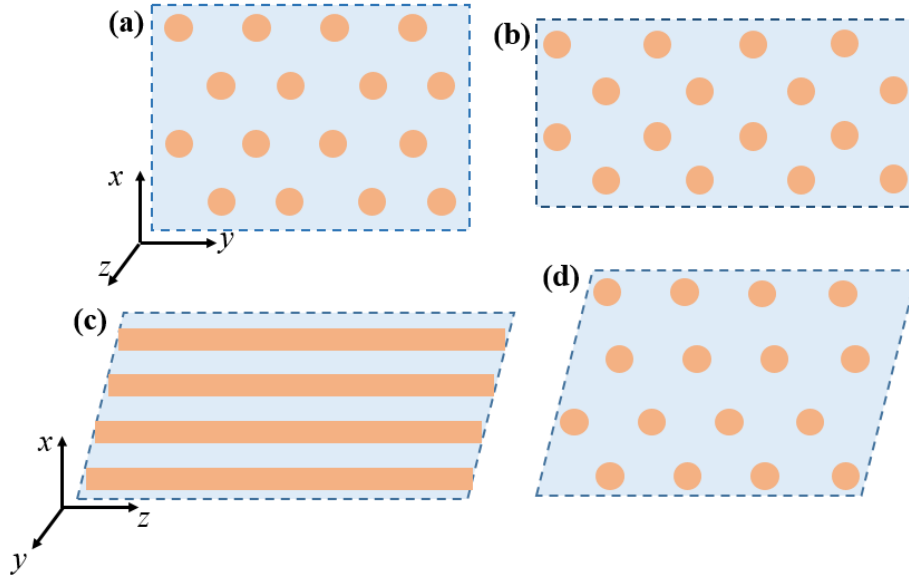


**Figure 4-10.** A sketch of a subdomain within an ion gel sample in the equilibrium state (a), undergoing transverse strain (b), undergoing shear strain in the  $xz$ -plane (c), and under shear strain in the  $xy$ -plane (d). The blue background represents the RTILs. The orange bars represent the PBDT polyanions. The dashed lines represent the simulation box.

Compared to  $E_{\parallel}$  and  $E_{\perp}$ , the shear modulus measured in the simulations is much smaller, which is also consistent with experimental results. The smaller shear modulus of the ion gel can also be qualitatively understood from the perspective of ionic space charge interference.

As shown in Figure 4-10c, under shear deformation in the  $xz$  or  $yz$ -plane, each rod is only slightly moved in the  $z$  direction relative to the rods surrounding it, therefore the ionic space charge associated with each rod only change marginally, and the charge interference in most of the space between the rods would be modified marginally. The corresponding change of the rod-rod

interaction energy and thus the shear modulus  $G_{13}$  and  $G_{23}$  would be small. When the material is sheared in the  $xy$ -plane as shown in Figure 4-10d, the impact on the ionic space charge interference in the triangular region is still small compared with that under transverse strain (shown in Figure 4-10b). As a result, the rod-rod interaction energy and thus the modulus will also be small under shear deformation in the  $xy$ -plane.

### 4.3. Conclusions

In summary, the mechanical properties of the model PBDT ion gels have been studied using MD simulations. The PBDT polyanions were fully aligned initially and the model ion gel was considered as transversely isotropic. By straining the model ion gel and recording the resulting stress in different directions, the modulus of the ion gel in different directions was calculated. The longitudinal modulus of the ion gel is very large since the PBDT polyanions carry most of the loads. The transverse modulus is smaller than the longitudinal modulus, but it is still much larger than that of most reported gel-like materials. The shear modulus of the model ion gel is much smaller than the transverse and longitudinal modulus, in agreement with recent experimental data.

Generally, the mechanical strength of ion gel comes from the ionic correlation inside the material, which governs the interactions between the polyanion nanorods. In order to understand the high modulus of the ion gels, the relationship between the interference of the ionic space charge and the interaction energy of two PBDT rods was first investigated. The results confirmed that the constructive (destructive) interference of the ionic space charge leads to a more negative (positive) free energy for the rod-rod interactions. Next, the ionic space charge interference in a model ion gel where the PBDT polyanions are in a hexagonal lattice was examined. It was found that the ionic space charge interference in the gap formed between three neighboring nanorods is

significant and can be notably modified by the transverse deformation of ion gel. Straining an ion gel worsens the interference of ionic space charge in this region and increases the rod-rod interaction energy. Because of the large number of PBDT nanorods in a unit volume of ion gels, straining the ion gel incurs large energy cost due to the increased rod-rod interaction energy in the gel and thus the mechanical modulus is high. Shear deformation has a smaller effect on the charge interference in the interstitial space among the PBDT polyanions, and this helps explain the relatively low shear modulus of ion gels revealed in recent experiments.

These results provide semi-quantitative data and preliminary explanation for understanding the mechanical properties observed for PBDT ion gels. Integration of the data and insights obtained here into future multiscale modeling will lead to more accurate prediction of the mechanical modulus of PBDT ion gels and facilitate development of effective guidelines for the rational engineering of this new class of polymer electrolytes.

## CHAPTER 5

### CONCLUSIONS

Room-temperature ionic liquids (RTILs) are molten salts composed completely of ions but remain in the liquid state at or below room temperature. Due to their great properties, RTILs and their derivatives are considered as promising candidates for use in a wide array of electrochemical devices. For supercapacitors, the emerging consensus is using RTILs as working electrolyte and porous carbon electrodes, which can greatly enhance the energy density of supercapacitors and thus help them break into mainstream market. For polymer electrolytes in devices such as batteries, the recent invented ion gels, in which RTILs are dispersed between PBDT polyanions, opens up new opportunities for engineering new electrolyte materials with long-sought properties, i.e., concurrently high ionic conductivity and mechanical modulus.

To optimize of the performance of the supercapacitors based on RTILs and nanoporous electrodes, it is important to have a fundamental understanding of the charge storage mechanism in them. Specifically, understanding the ion dynamics and charging dynamics of the ions in nanopores can help to resolve the issue of the lower power density of supercapacitors using these materials compared with conventional systems. To meet this need, the diffusion of EMIM<sup>+</sup> and TFSI<sup>-</sup> ions in slit-shaped micropores (width < 2 nm) under conditions similar to those during pore charging was studied first. The key findings are as follows:

1. In pores that accommodate only one layer of ions, the diffusion coefficient of an ion increased greatly during charging and exceeded the bulk diffusion values or even diffusion coefficients of small monovalent cations in bulk water. This speed up is attributed to the more facile breakage of the ionic cage around individual ions as the

charging proceeds, which is confirmed by a quantitative analysis of the cage dynamics of ions.

2. In very narrow pore where the conformation of ions is severely limited by confinement, the diffusion of TFSI<sup>-</sup> ions is very slow and does not increase as greatly as the more planar EMIM<sup>+</sup> ions when charging proceeds. On the other hand, in the wider pores that accommodat more than one layer of ions, ions diffusion was slower than in bulk RTILs and largely independent of the state of charge.
3. Overall, although many factors affect the ion diffusion, ion packing, which can change greatly during charging, plays the most important role. These results highlight the importance of understanding the charge dependence of ion diffusion in addition to the pore size dependence. These results also highlight the importance of precisely controlling pore size to realize fast ion diffusion in charged pores.

Next, the charge storage in RTIL-filled nanopores during cyclic charging and discharging was studied using coarse-grained molecular dynamics simulations. The key findings are as follows:

1. The cyclic charging and discharging of a nanopore are governed by the external field-driven ion transport and the sloshing dynamics of ions inside the pore. These two processes compete with (or facilitate) each other during the beginning (late) phase of the forward and the backward scan, which leads to the asymmetric shape of the cyclic voltammogram.
2. The dynamic charge storage in subnanometer pores is dominated by counterions, especially at high scan rates and in narrower pores, while the contribution of co-ions is marginal or negative. Such a phenomenon differs greatly from the charge storage under equilibrium conditions. The predominant contribution of counterions to the charge

storage observed here, termed perm-selective charging by prior researchers, is caused by the stronger electrical migration flux of counterions during charging, which in turn is caused by the relative abundance of counterions over co-ions inside the pore. During cyclic charging/discharging, nanopore systems are driven to far-from-equilibrium states.

To further develop the new class of ion gel represented by the recently invented PBDT ion gel, a fundamental understanding of the molecular mechanisms behind its properties such as high mechanical modulus is needed. Here, the mechanical modulus of a model PBDT ion gel is computed and analyzed using molecular dynamics. The key findings of this work are as follows:

1. MD simulations showed that the longitudinal modulus of the model ion gel is very large (on the order of several GPa), which is caused by the fact that PBDT polyanions carry most of the load. The modulus of the model ion gel in the transvers direction is on the order of several hundreds of MPa, while the shear modulus is quite low. Both observations are in qualitative agreement with the experiments.
2. The mechanical strength of ion gel comes from the ionic correlations within, which govern the interactions between the polyanion nanorods. The interference of the ionic space charge in the gap formed between three neighboring nanorods is significant and can be notably modified by the transverse deformation of ion gel. Straining an ion gel worsens the interference of ionic space charge in this region and increases the rod-rod interaction energy. Because of large number of PBDT nanorods in the ion gels, straining the ion gel incurs large energy cost and thus the transverse modulus is high. Shear deformation has a smaller effect on the charge interference in the interstitial space among the PBDT polyanions, and this helps explain the relatively low shear modulus of ion gels revealed in recent experiments.

In summary, this dissertation focused on the structure and dynamics of the nano-confined RTILs in two target application areas of RTILs. While the applications differ considerably, at a fundamental level, all the researches in this dissertation center on the most basic set of questions in molecular thermodynamics: how the molecular details of chemical species control the molecular and mesoscale structures of materials and systems; how these structures determine the dynamics of molecules and the macroscopic behavior of related systems. The diversity of the molecular structure of RTILs and the complexity of the electrostatic interactions in dense systems afford rich physics of RTILs in confined systems. Delineating these rich physics, beyond satisfying the curious minds, lays the theoretical foundation for the rational engineering of RTILs and RTIL-related materials to meet the demand by ever more exciting applications.

## REFERENCES

1. Total Energy Review. Administration, U. S. E. I., Ed. 2017.
2. Zachos, J.; Pagani, M.; Sloan, L.; Thomas, E.; Billups, K., Trends, Rhythms, and Aberrations in Global Climate 65 Ma to Present. *Science* **2001**, *292*, 686-693.
3. Shafiee, S.; Topal, E., When Will Fossil Fuel Reserves Be Diminished? *Energy Policy* **2009**, *37*, 181-189.
4. Borowy, B. S.; Salameh, Z. M., Dynamic Response of a Stand-Alone Wind Energy Conversion System with Battery Energy Storage to a Wind Gust. *IEEE T. Energy Conver.* **1997**, *12*, 73-78.
5. Gratzel, M., Solar Energy Conversion by Dye-Sensitized Photovoltaic Cells. *Inorg. Chem.* **2005**, *44*, 6841-6851.
6. Muetze, A.; Vining, J. G., Ocean Wave Energy Conversion - a Survey. In *2006 IEEE Industry Applications Conference, Forty-First Ias Annual Meeting*, 2006; Vol. 1-5, pp 1410-1417.
7. Pena, R.; Clare, J. C.; Asher, G. M. In *Doubly Fed Induction Generator Using Back-to-Back Pwm Converters and Its Application to Variable-Speed Wind-Energy Generation*, IEE Proceedings-Electric Power Applications, May; 1996; pp 231-241.
8. Goodenough, J. B.; Abruna, H. D.; Buchanan, M. V. *Basic Research Needs for Electrical Energy Storage. Report of the Basic Energy Sciences Workshop on Electrical Energy Storage, April 2-4, 2007*; United States, 2007-04-04, 2007.
9. Earle Waghorne, W., Viscosities of Electrolyte Solutions. *Phil. Trans. R. Soc. Lond. A* **2001**, *359*, 1529-1543.
10. Song, J. Y.; Wang, Y. Y.; Wan, C. C., Review of Gel-Type Polymer Electrolytes for Lithium-Ion Batteries. *J. Power Sources* **1999**, *77*, 183-197.
11. Luo, X.; Wang, J.; Dooner, M.; Clarke, J., Overview of Current Development in Electrical Energy Storage Technologies and the Application Potential in Power System Operation. *Appl. Energ.* **2015**, *137*, 511-536.
12. Díaz-González, F.; Sumper, A.; Gomis-Bellmunt, O.; Villafáfila-Robles, R., A Review of Energy Storage Technologies for Wind Power Applications. *Renew. Sust. Energ. Rev.* **2012**, *16*, 2154-2171.
13. Miller, J. R.; Simon, P., Materials Science - Electrochemical Capacitors for Energy Management. *Science* **2008**, *321*, 651-652.
14. Mekhilef, S.; Saidur, R.; Safari, A., Comparative Study of Different Fuel Cell Technologies. *Renew. Sust. Energ. Rev.* **2012**, *16*, 981-989.
15. Simon, P.; Gogotsi, Y., Materials for Electrochemical Capacitors. *Nat. Mater.* **2008**, *7*, 845-854.
16. Zhang, L. L.; Zhao, X. S., Carbon-Based Materials as Supercapacitor Electrodes. *Chem. Soc. Rev.* **2009**, *38*, 2520-2531.
17. Wang, D. W.; Li, F.; Liu, M.; Lu, G. Q.; Cheng, H. M., 3d Aperiodic Hierarchical Porous Graphitic Carbon Material for High-Rate Electrochemical Capacitive Energy Storage (Vol 47, Pg 373, 2008). *Angew. Chem. Int. Ed.* **2008**, *47*, 373-376.
18. Wang, G. P.; Zhang, L.; Zhang, J. J., A Review of Electrode Materials for Electrochemical Supercapacitors. *Chem. Soc. Rev.* **2012**, *41*, 797-828.

19. Liu, C.; Li, F.; Ma, L. P.; Cheng, H. M., Advanced Materials for Energy Storage. *Adv. Mater.* **2010**, *22*, E28-E62.
20. Xu, L.; Jia, M.; Li, Y.; Jin, X.; Zhang, F., High-Performance MnO<sub>2</sub>-Deposited Graphene/Activated Carbon Film Electrodes for Flexible Solid-State Supercapacitor. *Sci. Rep.* **2017**, *7*, 12857.
21. Meyer, J. C.; Geim, A. K.; Katsnelson, M. I.; Novoselov, K. S.; Booth, T. J.; Roth, S., The Structure of Suspended Graphene Sheets. *Nature* **2007**, *446*, 60.
22. Ma, Z.; Kyotani, T.; Liu, Z.; Terasaki, O.; Tomita, A., Very High Surface Area Microporous Carbon with a Three-Dimensional Nano-Array Structure: Synthesis and Its Molecular Structure. *Chem. Mater.* **2001**, *13*, 4413-4415.
23. Korenblit, Y.; Rose, M.; Kockrick, E.; Borchardt, L.; Kvit, A.; Kaskel, S.; Yushin, G., High-Rate Electrochemical Capacitors Based on Ordered Mesoporous Silicon Carbide-Derived Carbon. *Acs Nano* **2010**, *4*, 1337-1344.
24. Nien, Y.-H., The Application of Carbon Nanotube to Bone Cement. In *Carbon Nanotubes - Polymer Nanocomposites*, Yellampalli, S., Ed. InTech: Rijeka, 2011; p Ch. 18.
25. Endo, M.; Maeda, T.; Takeda, T.; Kim, Y. J.; Koshiba, K.; Hara, H.; Dresselhaus, M. S., Capacitance and Pore-Size Distribution in Aqueous and Nonaqueous Electrolytes Using Various Activated Carbon Electrodes. *J. Electrochem. Soc.* **2001**, *148*, A910-A914.
26. Baughman, R. H.; Zakhidov, A. A.; de Heer, W. A., Carbon Nanotubes - the Route toward Applications. *Science* **2002**, *297*, 787-792.
27. Zhu, Y. W., et al., Carbon-Based Supercapacitors Produced by Activation of Graphene. *Science* **2011**, *332*, 1537-1541.
28. Tarascon, J. M.; Armand, M., Issues and Challenges Facing Rechargeable Lithium Batteries. *Nature* **2001**, *414*, 359-367.
29. Patil, A.; Patil, V.; Shin, D. W.; Choi, J. W.; Paik, D. S.; Yoon, S. J., Issue and Challenges Facing Rechargeable Thin Film Lithium Batteries. *Mater. Res. Bull.* **2008**, *43*, 1913-1942.
30. Keppeler, M.; Shen, N.; Nageswaran, S.; Srinivasan, M., Synthesis of [Small Alpha]-Fe<sub>2</sub>O<sub>3</sub>/Carbon Nanocomposites as High Capacity Electrodes for Next Generation Lithium Ion Batteries: A Review. *J. Mater. Chem. A* **2016**, *4*, 18223-18239.
31. Poizot, P.; Laruelle, S.; Grugeon, S.; Dupont, L.; Tarascon, J. M., Nano-Sized Transition-Metal Oxides as Negative-Electrode Materials for Lithium-Ion Batteries. *Nature* **2000**, *407*, 496-499.
32. Demirocak, E. D.; Srinivasan, S. S.; Stefanakos, K. E., A Review on Nanocomposite Materials for Rechargeable Li-Ion Batteries. *Appl. Sci.* **2017**, *7*.
33. Zhou, Y.; Wang, J.; Hu, Y.; O'Hayre, R.; Shao, Z., A Porous LiFePO<sub>4</sub> and Carbon Nanotube Composite. *Chem. Commun.* **2010**, *46*, 7151-7153.
34. Yang, J.; Wang, J.; Wang, D.; Li, X.; Geng, D.; Liang, G.; Gauthier, M.; Li, R.; Sun, X., 3d Porous LiFePO<sub>4</sub>/Graphene Hybrid Cathodes with Enhanced Performance for Li-Ion Batteries. *J. Power Sources* **2012**, *208*, 340-344.
35. Shi, Y.; Chou, S.-L.; Wang, J.-Z.; Wexler, D.; Li, H.-J.; Liu, H.-K.; Wu, Y., Graphene Wrapped LiFePO<sub>4</sub>/C Composites as Cathode Materials for Li-Ion Batteries with Enhanced Rate Capability. *J. Mater. Chem.* **2012**, *22*, 16465-16470.
36. Liu, Q.; Dong, X.; Xiao, G.; Zhao, F.; Chen, F., A Novel Electrode Material for Symmetrical Sofcs. *Adv. Mater.* **2010**, *22*, 5478-5482.
37. Litster, S.; McLean, G., Pem Fuel Cell Electrodes. *J. Power Sources* **2004**, *130*, 61-76.

38. Zhong, C.; Deng, Y. D.; Hu, W. B.; Qiao, J. L.; Zhang, L.; Zhang, J. J., A Review of Electrolyte Materials and Compositions for Electrochemical Supercapacitors. *Chem. Soc. Rev.* **2015**, *44*, 7484-7539.
39. Li, Q.; Chen, J.; Fan, L.; Kong, X.; Lu, Y., Progress in Electrolytes for Rechargeable Li-Based Batteries and Beyond. *Green Energy Environ.* **2016**, *1*, 18-42.
40. O'Hayre, R.; Cha, S.-W.; Colella, W.; Prinz, F., *Fuel Cell Fundamentals, 3rd Edition*; John Wiley & Sons, 2016.
41. Lei, Z.; Chen, B.; Koo, Y.-M.; MacFarlane, D. R., Introduction: Ionic Liquids. *Chem. Rev.* **2017**, *117*, 6633-6635.
42. Welton, T., Room-Temperature Ionic Liquids. Solvents for Synthesis and Catalysis. *Chem. Rev.* **1999**, *99*, 2071-2084.
43. Hallett, J. P.; Welton, T., Room-Temperature Ionic Liquids: Solvents for Synthesis and Catalysis. 2. *Chem. Rev.* **2011**, *111*, 3508-3576.
44. Randström, S.; Montanino, M.; Appetecchi, G. B.; Lagergren, C.; Moreno, A.; Passerini, S., Effect of Water and Oxygen Traces on the Cathodic Stability of N-Alkyl-N-Methylpyrrolidinium Bis(Trifluoromethanesulfonyl)Imide. *Electrochim. Acta* **2008**, *53*, 6397-6401.
45. Armand, M.; Endres, F.; MacFarlane, D. R.; Ohno, H.; Scrosati, B., Ionic-Liquid Materials for the Electrochemical Challenges of the Future. *Nat. Mater.* **2009**, *8*, 621.
46. Osada, I.; de Vries, H.; Scrosati, B.; Passerini, S., Ionic-Liquid-Based Polymer Electrolytes for Battery Applications. *Angew. Chem. Int. Ed.* **2016**, *55*, 500-513.
47. Wasserscheid, P.; Welton, T., *Ionic Liquids in Synthesis*, 2nd ed.; Wiley-VCH: Weinheim :, 2008.
48. Bockris, J. O. M.; Reddy, A. K. N.; Gamboa-Aldeco, M., *Modern Electrochemistry 2a: Fundamentals of Electrode Processes*, 2nd ed.; Springer Science & Business Media: New York, 2001.
49. Wang, Y.; Chen, Y.; Gao, J.; Yoon, H. G.; Jin, L.; Forsyth, M.; Dingemans, T. J.; Madsen, L. A., Highly Conductive and Thermally Stable Ion Gels with Tunable Anisotropy and Modulus. *Adv. Mater.* **2016**, *28*, 2571-2578.
50. Schulze, M. W.; McIntosh, L. D.; Hillmyer, M. A.; Lodge, T. P., High-Modulus, High-Conductivity Nanostructured Polymer Electrolyte Membranes Via Polymerization-Induced Phase Separation. *Nano Lett.* **2014**, *14*, 122-126.
51. Xu, W.; Wang, J.; Ding, F.; Chen, X.; Nasybulin, E.; Zhang, Y.; Zhang, J.-G., Lithium Metal Anodes for Rechargeable Batteries. *Energy Environ. Sci.* **2014**, *7*, 513-537.
52. Brandt, A.; Pohlmann, S.; Varzi, A.; Balducci, A.; Passerini, S., Ionic Liquids in Supercapacitors. *MRS Bull.* **2013**, *38*, 554-559.
53. Ruiz, V.; Huynh, T.; Sivakkumar, S. R.; Pandolfo, A. G., Ionic Liquid-Solvent Mixtures as Supercapacitor Electrolytes for Extreme Temperature Operation. *RSC Advances* **2012**, *2*, 5591-5598.
54. Palm, R.; Kurig, H.; Tönurist, K.; Jänes, A.; Lust, E., Is the Mixture of 1-Ethyl-3-Methylimidazolium Tetrafluoroborate and 1-Butyl-3-Methylimidazolium Tetrafluoroborate Applicable as Electrolyte in Electrical Double Layer Capacitors? *Electrochem. Commun.* **2012**, *22*, 203-206.
55. Péan, C.; Merlet, C.; Rotenberg, B.; Madden, P. A.; Taberna, P.-L.; Daffos, B.; Salanne, M.; Simon, P., On the Dynamics of Charging in Nanoporous Carbon-Based Supercapacitors. *ACS Nano* **2014**, *8*, 1576-1583.

56. He, Y.; Huang, J.; Sumpter, B. G.; Kornyshev, A. A.; Qiao, R., Dynamic Charge Storage in Ionic Liquids-Filled Nanopores: Insight from a Computational Cyclic Voltammetry Study. *J. Phys. Chem. Lett.* **2015**, *6*, 22-30.
57. Kondrat, S.; Wu, P.; Qiao, R.; Kornyshev, A., Accelerating Charging Dynamics in Sub-Nanometer Pores. *Nat. Mater.* **2014**, *13*, 387-393.
58. Shaplov, A. S.; Marcilla, R.; Mecerreyes, D., Recent Advances in Innovative Polymer Electrolytes Based on Poly(Ionic Liquid)S. *Electrochim. Acta* **2015**, *175*, 18-34.
59. Lodge, T. P., A Unique Platform for Materials Design. *Science* **2008**, *321*, 50.
60. Meyer, W. H., Polymer Electrolytes for Lithium-Ion Batteries. *Adv. Mater.* **1998**, *10*, 439-448.
61. Cho, J. H.; Lee, J.; He, Y.; Kim, B. S.; Lodge, T. P.; Frisbie, C. D., High-Capacitance Ion Gel Gate Dielectrics with Faster Polarization Response Times for Organic Thin Film Transistors. *Adv. Mater.* **2008**, *20*, 686-690.
62. Le Bideau, J.; Ducros, J.-B.; Soudan, P.; Guyomard, D., Solid-State Electrode Materials with Ionic-Liquid Properties for Energy Storage: The Lithium Solid-State Ionic-Liquid Concept. *Adv. Funct. Mater.* **2011**, *21*, 4073-4078.
63. Arbizzani, C.; Biso, M.; Cericola, D.; Lazzari, M.; Soavi, F.; Mastragostino, M., Safe, High-Energy Supercapacitors Based on Solvent-Free Ionic Liquid Electrolytes. *J. Power Sources* **2008**, *185*, 1575-1579.
64. Largeot, C.; Portet, C.; Chmiola, J.; Taberna, P.-L.; Gogotsi, Y.; Simon, P., Relation between the Ion Size and Pore Size for an Electric Double-Layer Capacitor. *J. Am. Chem. Soc.* **2008**, *130*, 2730-2731.
65. Simon, P.; Gogotsi, Y., Capacitive Energy Storage in Nanostructured Carbon–Electrolyte Systems. *Acc. Chem. Res.* **2013**, *46*, 1094-1103.
66. Fedorov, M. V.; Kornyshev, A. A., Ionic Liquids at Electrified Interfaces. *Chem. Rev.* **2014**, *114*, 2978-3036.
67. Shim, Y.; Kim, H. J., Nanoporous Carbon Supercapacitors in an Ionic Liquid: A Computer Simulation Study. *Acs Nano* **2010**, *4*, 2345-2355.
68. Skinner, B.; Chen, T. R.; Loth, M. S.; Shklovskii, B. I., Theory of Volumetric Capacitance of an Electric Double-Layer Supercapacitor. *Phys. Rev. E* **2011**, *83*.
69. Kondrat, S.; Kornyshev, A., Superionic State in Double-Layer Capacitors with Nanoporous Electrodes. *J. Phys. Condens. Matter* **2011**, *23*, 022201.
70. Xing, L.; Vatamanu, J.; Borodin, O.; Bedrov, D., On the Atomistic Nature of Capacitance Enhancement Generated by Ionic Liquid Electrolyte Confined in Subnanometer Pores. *J. Phys. Chem. Lett.* **2013**, *4*, 132-140.
71. Merlet, C.; Rotenberg, B.; Madden, P. A.; Taberna, P. L.; Simon, P.; Gogotsi, Y.; Salanne, M., On the Molecular Origin of Supercapacitance in Nanoporous Carbon Electrodes. *Nat. Mater.* **2012**, *11*, 306-310.
72. Jiang, D. E.; Jin, Z. H.; Wu, J. Z., Oscillation of Capacitance inside Nanopores. *Nano Lett.* **2011**, *11*, 5373-5377.
73. Feng, G.; Cummings, P. T., Supercapacitor Capacitance Exhibits Oscillatory Behavior as a Function of Nanopore Size. *The Journal of Physical Chemistry Letters* **2011**, *2*, 2859-2864.
74. Kajdos, A.; Kvit, A.; Jones, F.; Jagiello, J.; Yushin, G., Tailoring the Pore Alignment for Rapid Ion Transport in Microporous Carbons. *J. Am. Chem. Soc.* **2010**, *132*, 3252-3253.

75. Rose, M.; Korenblit, Y.; Kockrick, E.; Borchardt, L.; Oschatz, M.; Kaskel, S.; Yushin, G., Hierarchical Micro- and Mesoporous Carbide-Derived Carbon as a High-Performance Electrode Material in Supercapacitors. *Small* **2011**, *7*, 1108-1117.
76. Monk, J.; Singh, R.; Hung, F. R., Effects of Pore Size and Pore Loading on the Properties of Ionic Liquids Confined inside Nanoporous Cmk-3 Carbon Materials. *J. Phys. Chem. C* **2011**, *115*, 3034-3042.
77. Rajput, N. N.; Monk, J.; Hung, F. R., Structure and Dynamics of an Ionic Liquid Confined inside a Charged Slit Graphitic Nanopore. *J. Phys. Chem. C* **2012**, *116*, 14504-14513.
78. Singh, R.; Rajput, N. N.; He, X.; Monk, J.; Hung, F. R., Molecular Dynamics Simulations of the Ionic Liquid [Emim+][Tfmsi-] Confined inside Rutile (110) Slit Nanopores. *Phys. Chem. Chem. Phys.* **2013**, *15*, 16090-16103.
79. Singh, R.; Monk, J.; Hung, F. R., Heterogeneity in the Dynamics of the Ionic Liquid Bmim+ Pf6- Confined in a Slit Nanopore. *J. Phys. Chem. C* **2011**, *115*, 16544-16554.
80. Rajput, N. N.; Monk, J.; Singh, R.; Hung, F. R., On the Influence of Pore Size and Pore Loading on Structural and Dynamical Heterogeneities of an Ionic Liquid Confined in a Slit Nanopore. *The Journal of Physical Chemistry C* **2012**, *116*, 5169-5181.
81. Shi, W.; Sorescu, D. C., Molecular Simulations of Co<sub>2</sub> and H<sub>2</sub> Sorption into Ionic Liquid 1-N-Hexyl-3-Methylimidazolium Bis(Trifluoromethylsulfonyl)Amide ( Hmim Tf<sub>2</sub>n ) Confined in Carbon Nanotubes. *J. Phys. Chem. B* **2010**, *114*, 15029-15041.
82. Iacob, C.; Sangoro, J. R.; Kipnusu, W. K.; Valiullin, R.; Kaerger, J.; Kremer, F., Enhanced Charge Transport in Nano-Confined Ionic Liquids. *Soft Matter* **2012**, *8*, 289-293.
83. Chaban, V. V.; Prezhdo, O. V., Nanoscale Carbon Greatly Enhances Mobility of a Highly Viscous Ionic Liquid. *Acs Nano* **2014**, *8*, 8190-8197.
84. Levi, M. D.; Salitra, G.; Levy, N.; Aurbach, D.; Maier, J., Application of a Quartz-Crystal Microbalance to Measure Ionic Fluxes in Microporous Carbons for Energy Storage. *Nat. Mater.* **2009**, *8*, 872-875.
85. Levi, M. D.; Levy, N.; Sigalov, S.; Salitra, G.; Aurbach, D.; Maier, J., Electrochemical Quartz Crystal Microbalance (Eqcm) Studies of Ions and Solvents Insertion into Highly Porous Activated Carbons. *J. Am. Chem. Soc.* **2010**, *132*, 13220-13222.
86. Wang, H.; Forse, A. C.; Griffin, J. M.; Trease, N. M.; Trognko, L.; Taberna, P.-L.; Simon, P.; Grey, C. P., In Situ Nmr Spectroscopy of Supercapacitors: Insight into the Charge Storage Mechanism. *J. Am. Chem. Soc.* **2013**, *135*, 18968-18980.
87. Richey, F. W.; Dyatkin, B.; Gogotsi, Y.; Elabd, Y. A., Ion Dynamics in Porous Carbon Electrodes in Supercapacitors Using in Situ Infrared Spectroelectrochemistry. *J. Am. Chem. Soc.* **2013**, *135*, 12818-12826.
88. Tsai, W.-Y.; Taberna, P.-L.; Simon, P., Electrochemical Quartz Crystal Microbalance (Eqcm) Study of Ion Dynamics in Nanoporous Carbons. *J. Am. Chem. Soc.* **2014**, *136*, 8722-8728.
89. Kondrat, S.; Kornyshev, A., Charging Dynamics and Optimization of Nanoporous Supercapacitors. *J. Phys. Chem. C* **2013**, *117*, 12399-12406.
90. Lee, A. A.; Kondrat, S.; Oshanin, G.; Kornyshev, A. A., Charging Dynamics of Supercapacitors with Narrow Cylindrical Nanopores. *Nanotechnology* **2014**, *25*.
91. Okoshi, K.; Kamee, H.; Suzuki, G.; Tokita, M.; Fujiki, M.; Watanabe, J., Well-Defined Phase Sequence Including Cholesteric, Smectic a, and Columnar Phases Observed in a Thermotropic Lc System of Simple Rigid-Rod Helical Polysilane. *Macromolecules* **2002**, *35*, 4556-4559.

92. Watson, J. D.; Crick, F. H. C., Molecular Structure of Nucleic Acids: A Structure for Deoxyribose Nucleic Acid. *Nature* **1953**, *171*, 737-738.
93. Albrecht, M., "Let's Twist Again" Double-Stranded, Triple-Stranded, and Circular Helicates. *Chem. Rev.* **2001**, *101*, 3457-3498.
94. Yu, Z.; He, Y.; Wang, Y.; Madsen, L. A.; Qiao, R., Molecular Structure and Dynamics of Ionic Liquids in a Rigid-Rod Polyanion-Based Ion Gel. *Langmuir* **2017**, *33*, 322-331.
95. Yu, Z.; Zhang, F.; Huang, J.; Sumpter, B. G.; Qiao, R., Ionic Liquids-Mediated Interactions between Nanorods. *J. Chem. Phys.* **2017**, *147*, 134704.
96. Hou, X.; Siow, K. S., Mechanical Properties and Ionic Conductivities of Plasticized Polymer Electrolytes Based on Abs/Pmma Blends. *Polymer* **2000**, *41*, 8689-8696.
97. Kim, S. H.; Choi, J. K.; Bae, Y. C., Mechanical Properties and Ionic Conductivity of Gel Polymer Electrolyte Based on Poly(Vinylidene-Fluoride-Co-Hexafluoropropylene). *J. Appl. Polym. Sci.* **2001**, *81*, 948-956.
98. Wang, Y.; Gao, J.; Dingemans, T. J.; Madsen, L. A., Molecular Alignment and Ion Transport in Rigid Rod Polyelectrolyte Solutions. *Macromolecules* **2014**, *47*, 2984-2992.
99. He, Y.; Qiao, R.; Vatamanu, J.; Borodin, O.; Bedrov, D.; Huang, J.; Sumpter, B. G., Importance of Ion Packing on the Dynamics of Ionic Liquids During Micropore Charging. *The Journal of Physical Chemistry Letters* **2016**, *7*, 36-42.
100. Vatamanu, J.; Borodin, O.; Bedrov, D.; Smith, G. D., Molecular Dynamics Simulation Study of the Interfacial Structure and Differential Capacitance of Alkylimidazolium Bis(Trifluoromethanesulfonyl)Imide C(N)Mim Tfsi Ionic Liquids at Graphite Electrodes. *J. Phys. Chem. C* **2012**, *116*, 7940-7951.
101. Borodin, O.; Smith, G. D., Development of Many-Body Polarizable Force Fields for Li-Battery Components: 1. Ether, Alkane, and Carbonate-Based Solvents. *J. Phys. Chem. B* **2006**, *110*, 6279-6292.
102. Plimpton, S., Fast Parallel Algorithms for Short-Range Molecular Dynamics. *J. Comput. Phys.* **1995**, *117*, 1-19.
103. Wang, Z.; Yang, Y.; Olmsted, D. L.; Asta, M.; Laird, B. B., Evaluation of the Constant Potential Method in Simulating Electric Double-Layer Capacitors. *J. Chem. Phys.* **2014**, *141*, 184102.
104. Hockney, R. W.; Eastwood, J. W., *Computer Simulation Using Particles*; Adam Hilger: New York, 1989.
105. Wei, D.; Song, Y.; Wang, F., A Simple Molecular Mechanics Potential for Mu M Scale Graphene Simulations from the Adaptive Force Matching Method. *J. Chem. Phys.* **2011**, *134*, 184704.
106. Martinez, L.; Andrade, R.; Birgin, E. G.; Martinez, J. M., Packmol: A Package for Building Initial Configurations for Molecular Dynamics Simulations. *J. Comput. Chem.* **2009**, *30*, 2157-2164.
107. Frenkel, D.; Smit, B., *Understanding Molecular Simulation. From Algorithms to Applications*; Academic Press: San Diego, 1996.
108. Fell, C. J. D.; Hutchison, H., Diffusion Coefficients for Sodium and Potassium Chlorides in Water at Elevated Temperatures. *J. Chem. Eng. Data* **1971**, *16*, 427-429.
109. Schroder, C., Collective Translational Motions and Cage Relaxations in Molecular Ionic Liquids. *J. Chem. Phys.* **2011**, *135*, 024502.
110. Shi, R.; Wang, Y., Ion-Cage Interpretation for the Structural and Dynamic Changes of Ionic Liquids under an External Electric Field. *J. Phys. Chem. B* **2013**, *117*, 5102-5112.

111. Fujii, K.; Fujimori, T.; Takamuku, T.; Kanzaki, R.; Umebayashi, Y.; Ishiguro, S. I., Conformational Equilibrium of Bis(Trifluoromethanesulfonyl) Imide Anion of a Room-Temperature Ionic Liquid: Raman Spectroscopic Study and Dft Calculations. *J. Phys. Chem. B* **2006**, *110*, 8179-8183.
112. Oschatz, M.; Boukhalfa, S.; Nickel, W.; Lee, J. T.; Klosz, S.; Borchardt, L.; Eychmueller, A.; Yushin, G.; Kaskel, S., Kroll-Carbons Based on Silica and Alumina Templates as High-Rate Electrode Materials in Electrochemical Double-Layer Capacitors. *J. Mater. Chem. A* **2014**, *2*, 5131-5139.
113. He, Y.; Huang, J.; Sumpter, B. G.; Kornyshev, A. A.; Qiao, R., Dynamic Charge Storage in Ionic Liquids-Filled Nanopores: Insight from a Computational Cyclic Voltammetry Study. *The Journal of Physical Chemistry Letters* **2015**, *6*, 22-30.
114. Fedorov, M. V.; Kornyshev, A. A., Towards Understanding the Structure and Capacitance of Electrical Double Layer in Ionic Liquids. *Electrochim. Acta* **2008**, *53*, 6835-6840.
115. Feng, G.; Cummings, P. T., Supercapacitor Capacitance Exhibits Oscillatory Behavior as a Function of Nanopore Size. *J. Phys. Chem. Lett.* **2011**, *2*, 2859-2864.
116. Merlet, C.; Pean, C.; Rotenberg, B.; Madden, P. A.; Daffos, B.; Taberna, P. L.; Simon, P.; Salanne, M., Highly Confined Ions Store Charge More Efficiently in Supercapacitors. *Nat. Commun.* **2013**, *4*.
117. Lindahl, E.; Hess, B.; van der Spoel, D., Gromacs 3.0: A Package for Molecular Simulation and Trajectory Analysis. *J. Mol. Model.* **2001**, *7*, 306-317.
118. Merlet, C.; Péan, C.; Rotenberg, B.; Madden, P. A.; Simon, P.; Salanne, M., Simulating Supercapacitors: Can We Model Electrodes as Constant Charge Surfaces? *J. Phys. Chem. Lett.* **2013**, *4*, 264-268.
119. Raghunathan, A. V.; Aluru, N. R., Self-Consistent Molecular Dynamics Formulation for Electric-Field-Mediated Electrolyte Transport through Nanochannels. *Phys. Rev. E* **2007**, *76*.
120. Wu, P.; Huang, J. S.; Meunier, V.; Sumpter, B. G.; Qiao, R., Complex Capacitance Scaling in Ionic Liquids-Filled Nanopores. *Acs Nano* **2011**, *5*, 9044-9051.
121. Yang, X. W.; Cheng, C.; Wang, Y. F.; Qiu, L.; Li, D., Liquid-Mediated Dense Integration of Graphene Materials for Compact Capacitive Energy Storage. *Science* **2013**, *341*, 534-537.
122. Lukatskaya, M. R.; Mashtalir, O.; Ren, C. E.; Dall'Agnese, Y.; Rozier, P.; Taberna, P. L.; Naguib, M.; Simon, P.; Barsoum, M. W.; Gogotsi, Y., Cation Intercalation and High Volumetric Capacitance of Two-Dimensional Titanium Carbide. *Science* **2013**, *341*, 1502-1505.
123. Pell, W. G.; Conway, B. E., Voltammetry at a De Levie Brush Electrode as a Model for Electrochemical Supercapacitor Behaviour. *J. Electroanal. Chem.* **2001**, *500*, 121-133.
124. Lin, R.; Huang, P.; Segalini, J.; Largeot, C.; Taberna, P. L.; Chmiola, J.; Gogotsi, Y.; Simon, P., Solvent Effect on the Ion Adsorption from Ionic Liquid Electrolyte into Sub-Nanometer Carbon Pores. *Electrochim. Acta* **2009**, *54*, 7025-7032.
125. Wu, P.; Huang, J.; Meunier, V.; Sumpter, B. G.; Qiao, R., Voltage Dependent Charge Storage Modes and Capacity in Subnanometer Pores. *J. Phys. Chem. Lett.* **2012**, *3*, 1732-1737.
126. Allen, M. P.; Tildesley, D. J., *Computer Simulation of Liquids*; Clarendon Press Oxford [England], 1989.

127. Zhong, X.; Liu, Z.; Cao, D., Improved Classical United-Atom Force Field for Imidazolium-Based Ionic Liquids: Tetrafluoroborate, Hexafluorophosphate, Methylsulfate, Trifluoromethylsulfonate, Acetate, Trifluoroacetate, and Bis(Trifluoromethylsulfonyl)Amide. *J. Phys. Chem. B* **2011**, *115*, 10027-10040.
128. Zoete, V.; Cuendet, M. A.; Grosdidier, A.; Michielin, O., Swissparam: A Fast Force Field Generation Tool for Small Organic Molecules. *J. Comput. Chem.* **2011**, *32*, 2359-2368.